Ph. D. Thesis

Enhanced flux pinning to high fields in YBCO and YBCO/Ag Superconductors through Preform Optimization in Infiltration and Growth Process

N. Devendra Kumar

School of Physics, University of Hyderabad
2011

ENHANCED FLUX PINNING TO HIGH FIELDS IN YBCO and YBCO/Ag SUPERCONDUCTORS THROUGH PREFORM OPTIMIZATION IN INFILTRATION AND GROWTH PROCESS

A THESIS SUBMITTED FOR THE DEGREE OF
DOCTOR OF PHILOSOPHY

BY

N. DEVENDRA KUMAR

**School of Physics
University of Hyderabad
Hyderabad – 500046, India**

August 2011

DEDICATED

TO

MY PARENTS

DECLARATION

I hereby declare that the work reported in this thesis has been carried out by me under the supervision of ***Professor V. Seshubai***, School of Physics, University of Hyderabad, Hyderabad, India. I also declare that this has not been submitted to any University or Institution for the award of any degree/diploma.

N. Devendra Kumar

Date: August 11 2011

Place: Hyderabad

CERTIFICATE

This is to certify that the research work compiled in this thesis entitled "**Enhanced flux pinning to high fields in YBCO and YBCO/Ag superconductors through preform optimization in Infiltration and Growth process**" has been carried out by *Mr. N. Devendra Kumar* under my supervision and the same has not been submitted for the award of any degree of any University.

Dr. V. SESHUBAI

RESEARCH SUPERVISOR
PROFESSOR, School of Physics
University of Hyderabad

Date: August 11 2011

Place: Hyderabad

DEAN
SCHOOL OF PHYSICS

ACKNOWLEDGEMENTS

I would like to express my sincere gratitude to my supervisor *Prof. V. Seshubai* for her constant inspiration, continuous support during the entire course of my research work, exceptional patience with critical reading, re-reading and correcting successive version of the manuscript. I also admire her for the dedication that she has shown, in cultivating right concepts and igniting interest and zeal for research work at my post-graduation stage.

I thank the Dean **Prof. C. Bansal**, School of Physics for enabling me to use all the central facilities of the school required for the work reported in the thesis. I also thank my teachers and former Deans of the school **Prof. A.K. Bhatnagar, Prof. A.P. Pathak, Prof. S.N. Kaul, Prof. V.S.S. Sastry, Prof. Vipin Srivastava** and all other faculty of the school for their constant support and encouragement.

I would like to acknowledge **Dr. T. Rajasekharan**, Scientist-G, Defense Metallurgical Research laboratory (DMRL), Kanchenbagh, Hyderabad for his support, co-operation and suggestions at various stages of this work. I extend my thanks to him for the keen interest that he took in my work. New ideas suggested by him, has improved the quality of the work presented in this dissertation. His advice and suggestions at various stages of this work very fruitful. This manuscript has taken its complete form with his great involvement in the work. Additionally I am benefited substantially from many meetings and discussions that I had with him.

I thank **Prof. S.N. Kaul**, Coordinator, *Centre for Nanotechnology (CFN)*, University of Hyderabad for permitting me to characterize many of my superconducting samples using Physical Property Measurement System

I thank the **Dr. Maqbool Ahmed**, PSO, Central Instrument Laboratory, University of Hyderabad for permitting me to use many of the central facilities to characterize the samples like X-ray diffractometer, Scanning Electron Microscope. I also thank **Mr. C. S. Murthy**, Senior Scientific Officer for his special concern. I thank Dr.

this work by fabricating various sample holders required for erecting various measurement facilities. I specially thank **Mr. P. Krishna** for the invaluable services rendered in connection with setting up of various experimental facilities during the work carried. I also thank all the non-teaching staff specially Mr. Abraham, Mr. G.L.N. Murthy, Mr. Anantharao, Mr. Mohan Rao, Ms. Saramma, Mr. Sunil for their timely help.

I wish to thank my seniors Dr. V. L. Kameswari, Dr. S. Santhosh, Dr. K. Balkis Ameen, my colleagues A. Satish Kumar, P. M. Swaroop Raju, M. Ramudu, R. Parthasarathy, M. Mahalaxmi, S. Pavan Kumar, M. Manikanta and others at the University. I would like to specially thank **Mr. M. Ramudu and P.M. Swaroop Raju**, for helping with the thesis printing and arrangements. I also wish to acknowledge **all my friends in School of Physics** for their cooperation in carrying out my research work and also for making my stay in the University a pleasant and beneficial experience.

There are no words to express my gratitude towards my *Parents* who have borne patience and continuously supported me to make my desire a reality. I wish to extend my thanks to my brothers and my sister-in-Law and convey my love to my niece *Sai Yashaswini*.

PLACE: HYDERABAD

DATE :   11th August 2011

(N. DEVENDRA KUMAR)

<u>INDEX</u>

<u>CONTENTS</u>

CHAPTER I

INTRODUCTION

CHAPTER II

EXPERIMENTAL TECHNIQUES

CHAPTER III

DEVELOPMENT OF

PREFORM OPTIMISED INFILTRATION AND GROWTH PROCESS (POIGP)

CHAPTER IV

YBCO/Ag SUPERCONDUCTING COMPOSITES FABRICATED USING POIGP

CHAPTER V

MICROSTRUCTURAL AND MAGNETIC PROPERTIES OF Y-Ba-Cu-O SUPERCONDUCTORS FABRICATED BY INTEGRATION OF DIRECTIONAL SOLIDIFICATION WITH POIGP

CHAPTER VI

ORIGIN OF FLUX PINNING LEADING TO ENHANCED CURRENT DENSITIES TO HIGH FIELDS: FURTHER INVESTIGATIONS

CHAPTER VII

SUMMARY AND CONCLUSIONS

APPENDIX

BASIC CONCEPTS IN SUPERCONDUCTIVITY

CHAPTER I

INTRODUCTION

1.1 Superconductors

The phenomenon of Superconductivity, since its discovery in 1911 in mercury (Hg) by Kammerlingh Onnes [1], has sprung a lot of surprises. Hg was found to lose measurable electrical resistance at temperatures below 4.2 K, its critical temperature (T_c). A number of elements, alloys and compounds show superconductivity at different temperatures [2-5]. Among the elements, Niobium (Nb) has the highest T_c of 9.2 K at atmospheric pressure. The compound Nb_3Ge held the record with a high transition temperature of 23 K [6], till the discovery of high temperature superconductors (HTS) [7]. Superconductivity is one area in which many Nobel prizes have been won both for experimental discoveries, and for contributions to theories put forward to explain the observed complexities.

Till 1986, research work on superconductivity was confined to only a few laboratories across the world which had access to expensive and scarcely available liquid helium cryogen. The discovery of high temperature superconductors (HTS) in La-Ba-Cu-O system ($T_c \sim 35$ K) in 1986 [7], followed by the important discovery of Y-Ba-Cu-O compound ($T_c \sim 92$ K) [8] in 1987 and other Cu-O based superconductors subsequently [9-12], has triggered wide-spread research all over the world. This is because of the possibility of studying these materials with the readily available, cheap and abundant liquid nitrogen with boiling point of 77 K. Some of the basic properties of superconductors are briefly discussed in Appendix.

1.2 High temperature superconductors

Soon after the discovery of La-Ba-Cu-O superconductor in 1986 by Georg Bednorz and Alex Müller [7], many compounds were discovered which showed superconductivity above the boiling point of liquid nitrogen. They belong to the Y-

Ba-Cu-O, Ba-Sr-Ca-Cu-O, Tl-Ba-Ca-Cu-O and Hg-Ba-Ca-Cu-O systems with higher critical temperatures as shown in Fig. 1.1. Among the HTS, transition temperatures up to 138 K (164 K under pressure [13]) have been recorded in Hg-based superconductors [11]. Recently, superconductivity was discovered in magnesium diboride (MgB_2), which showed a T_c of 39 K [14]. Another interesting discovery has been that of superconductivity in the fulleride compound CsC_{60}, with a T_c of 38 K [15]. Most recently, iron-based series of compounds have been discovered [16] whose T_c has risen to 52 K [17]. These materials have not yet been produced in single crystal form and may have magnetically mediated pairing [18].

The evolution in the transition temperature of superconducting materials, from mercury to high temperature superconductors, is shown in Fig. 1.1. The compound YBCO shown in figure has a composition $YBa_2Cu_3O_{7-\delta}$. The compositions of the other high T_c compounds shown are described in Appendix.
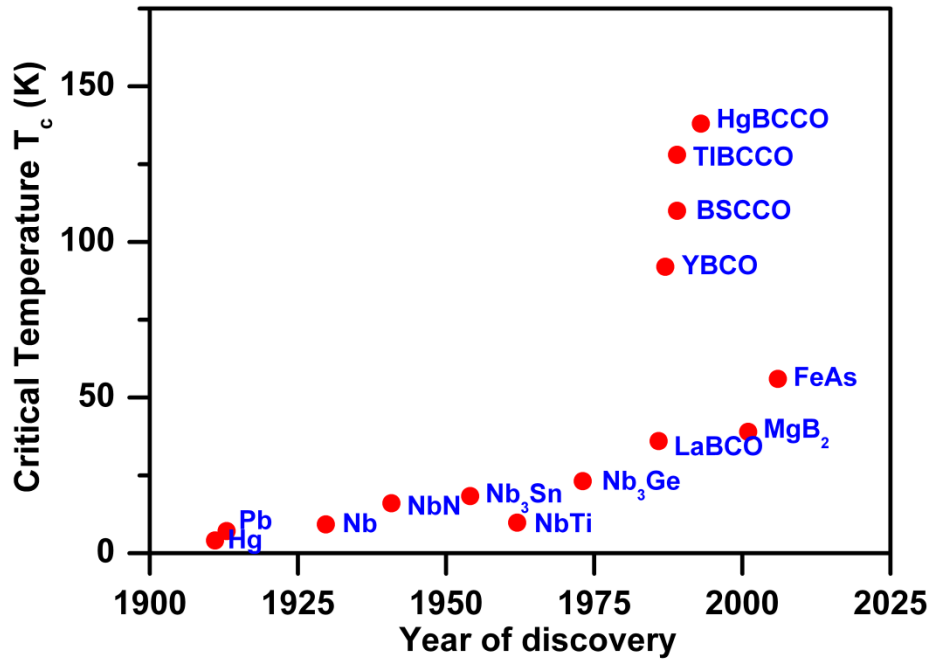
Fig. 1.1. Evolution in the transition temperatures of superconducting materials, starting with mercury. Recent discoveries are also included.

Table 1.1 compares some of the properties of conventional low temperature superconductors (LTS) with those of high temperature superconductors (HTS).

Table 1.1. Properties of some superconductors

Material	Critical Temperature T_c (K)	Coherence length ξ_o (nm)	London Penetration depth λ_L (nm)
Sn	3.7	230	34
Al	1.2	1600	16
Pb	7.2	83	37
Cd	0.52	760	110
Nb	9.2	38	39
NbN	16.0	4	250
Nb_3Ge	23.2	3	80
LaBCO	36.0	20	330
YBCO	92	2	150
BSCCO	110	2.9	165-230
TlBCCO	119	3	221
HgBCO	135	19.3	1540
MgB_2	39	4-12	85-180

Most of the research on HTS has been confined to BSSCO and REBCO systems [7-9, 12, 19-25]. MgB_2 has also been widely investigated [14, 26-28]. Research on Tl-Ba-Ca-Cu-O, Hg-Ba-Ca-Cu-O etc. compounds have been pursued to a much lesser extent due to the toxicity of the compounds and also due to the difficulties involved in their preparation [29]. BSCCO system has three superconducting phases namely: $Bi_2Sr_2CuO_6$ (Bi-2201), $Bi_2Sr_2CaCu_2O_8$ (Bi-2212) and $Bi_2Sr_2Ca_2Cu_3O_{10}$ (Bi-2223). These phases have T_c of ~ 25 K, 80 K and 110 K, respectively [30]. Recent work on superconducting materials has been focused on the development of superconducting wires and tapes which can be used in devices. Substantial amount

of work has been done on the BSCCO system in this direction due to the relative ease with which wires/tapes can be fabricated out of this material [31-34]. Bi-2223 wires carrying currents up to 126 A have been fabricated and used to produce magnets generating magnetic fields of ~ 1.3 T at 77 K [35]. Operation of these to higher magnetic fields has been limited by problems associated with flux creep [36, 37]. A further improvement resulted in the form of Dynamically Innovative BSCCO (DI-BSCCO) wire which could a carry a current of ~ 200 A at 77 K in zero field [38].

Extensive research was carried out by several groups across the world on rare-earth based REBCO HTS [21-25, 39-43]. The work on REBCO compounds is reviewed in detail in the subsequent sections because the present thesis deals with that material.

1.3 Work on High temperature REBCO superconductors

In the early days of HTS technology development, it was believed that cooling the devices made out of the materials to cryogenic temperatures would pose serious problems. With the developments in the technology of superconductor fabrication and also in cryogenics, many important applications are now being realized using these materials [44]. The most attractive material today for this purpose are the REBCO superconductors due to relatively lower toxicity, manageable flux-creep problems, reasonable transition temperatures, room available for altering their properties through process modifications etc. [45].

Most of the work on REBCO superconductors focuses today on the fabrication of wires/tapes/films of the material [46-48]. Coated conductors of REBCO are being developed on an industrial scale by techniques employing substrates coated by Ion beam assisted deposition (IBAD) [49] and using Rolling Assisted Biaxially Textured Substrates (RABiTS) [50]. Coated conductors supporting current densities as high as 1 MAcm^{-2} at 77 K and of lengths up to 1 m have been

produced on a reproducible basis [51]. Such tapes are being demonstrated in several projects [52, 53].

REBCO bulk materials also find a number of applications, though research on them has been limited in comparison with that on tapes [54]. Some examples of applications being pursued intensely are of flywheel batteries [55], trapped field magnets [56], current leads [57], hysteresis motors [58], power grids [59], fault current limiters [60] etc. Stable levitation without active control has been developed for non-contact bearings of a flywheel energy storage system [61], levitated vehicles [62] and non-contact mixers [63]. Trapped field magnets have been produced for magnetic field generation [56], magnetic separation for purifying water [64], magnetron-sputtering [65], material characterization using nuclear magnetic resonance spectrometer [66] etc. A brief description of some of the applications of bulk REBCO superconductors is provided in Appendix.

We discuss below briefly the properties of the REBCO superconductors, with particular attention paid to the $YBa_2Cu_3O_{7-\delta}$ compound whose processing is studied in this thesis.

1.4 Physical properties of YBCO

The first compound discovered among REBCO superconductors was $YBa_2Cu_3O_{7-\delta}$ (YBCO). This compound was discovered by Maw-Kuen Wu and Paul Chu in 1987 [8] which showed a T_c of 92 K. Y-Ba-Cu-O system has different phases like $YBa_2Cu_3O_{7-\delta}$ (Y-123, YBCO), $YBa_2Cu_4O_8$ (Y-124), $Y_2Ba_4Cu_7O_{14}$ (Y-247) and Y_2BaCuO_5 (Y-211) [67]. Among these phases, Y-123, Y-124 and Y-247 are superconducting phases with $T_c \sim$ 92 K, 80 K and 40 K, respectively. All the three have orthorhombic unit cells. Research on bulk Y-123 has been vigorously pursued for applications. Y-211 is a non-superconducting phase and is generally introduced as precipitates in appropriate proportions in Y-123 for enhancing flux pinning strength through creation of interfacial defects (at Y-211/Y-123 interfaces) [68]. Y-211 also has

orthorhombic symmetry. It has been found that T_c remains nearly unchanged if Y is partly or completely substituted by other rare-earth elements like Nd, Sm, Eu, Gd etc. in Y-123 [69, 70]. Improved pinning properties have been reported for compounds with two or three rare-earth elements substituted on Y site [71]; improved magnetic flux pinning in such cases is assisted by lattice mismatch effects.

1.4.1 Crystal structure of Y-123
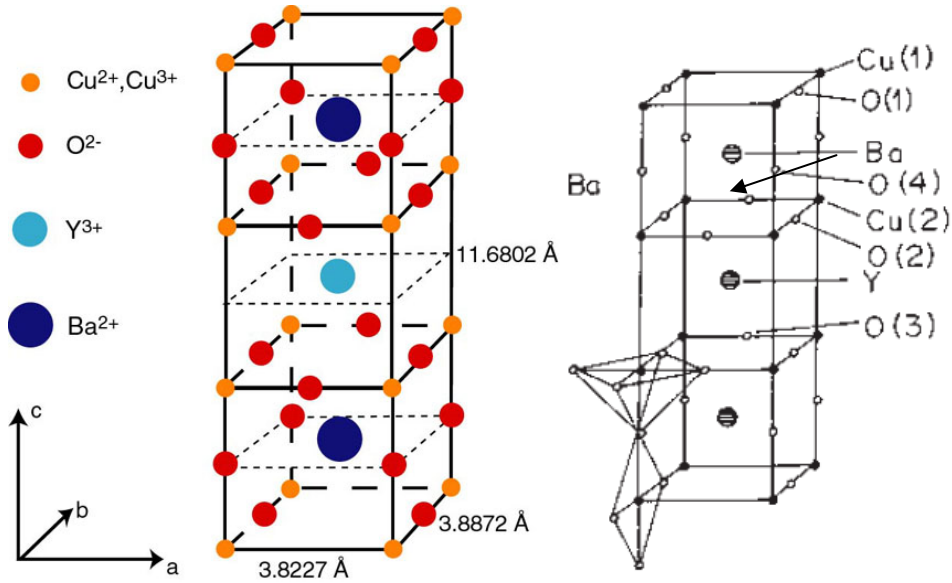
Fig. 1.2. Perovskite structure of YBCO showing the presence of copper planes and chains

The unit cell of $YBa_2Cu_3O_7$ is shown in Fig. 1.2. Y-123 has a crystal structure derived from that of a perovskite by tripling along the c-axis. It has an orthorhombic unit cell with lattice parameters a ~ 3.823 Å, b ~ 3.887 Å, c ~ 11.68 Å, and space group Pmmm [72]. The notable feature is the presence of a sequence of copper-oxygen layers perpendicular to the c-axis.

In REBCO compounds, oxygenation plays an important role in causing superconductivity [73]. In the structure of Y-123, Y and Ba are stacked in the sequence (Ba–Y–Ba) along the c-axis. From Fig. 1.2, it can be seen that all corner sites of the unit cell are occupied by Cu, which has two different coordinations, Cu(1) and Cu(2), with respect to oxygen. There are four possible crystallographic

sites for oxygen: O(1), O(2), O(3), and O(4) as shown in Fig. 1.2(b). The coordination polyhedra of Y and Ba with respect to oxygen are different.
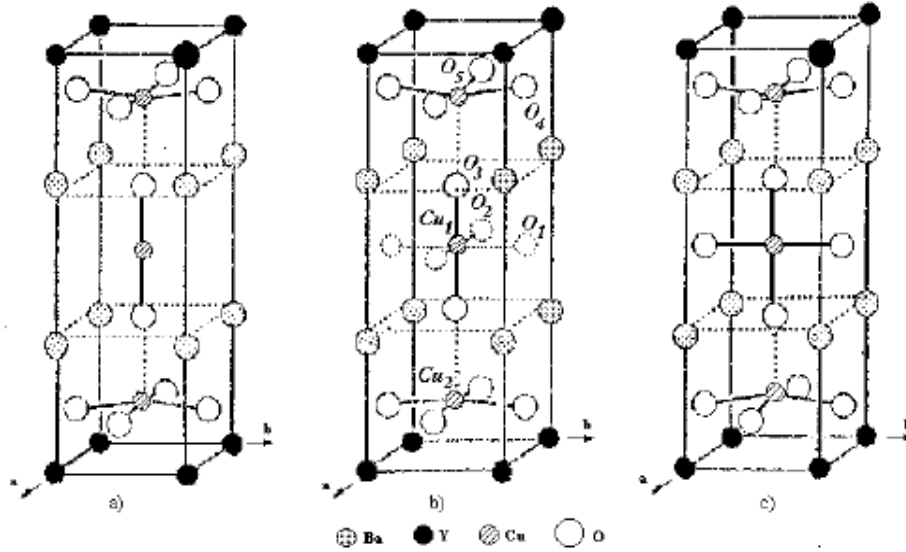
Fig. 1.3. The oxygen deficient perovskite structures for Y-Ba-Cu-O system with oxygen content (a) δ=6, (b) 6 < δ < 7, (c) δ = 7.

The tripling of the perovskite unit cell (ABO_3) leads to nine oxygen atoms, whereas $YBa_2Cu_3O_7$ has seven oxygen atoms accommodating a deficiency of two oxygen atoms. Thus, the structure of the 90 K phase deviates from the ideal perovskite structure and, therefore, is referred to as an oxygen-deficient perovskite structure. Oxygen atoms are missing from the Y plane (i.e., z - 1/2 site); thus, Y is surrounded by 8 oxygen atoms instead of the 12 if it had been in ideal perovskite structure. Oxygen atoms at the top and bottom planes of the $YBa_2Cu_3O_7$ unit cell are missing in the [100] direction, thus giving (Cu–O) chains in the [010] direction. The Ba atom has a coordination number of 10 oxygen atoms instead of 12 because of the absence of oxygen at the $\left(\frac{1}{2}, 0, z\right)$ site. The structure has a stacking of different layers: $(CuO)(BaO)(CuO_2)$-(Y)-$(CuO_2)(BaO)(CuO)$. One of the key features of the unit cell of Y-123 is the presence of two layers of CuO_2. The role of the Yttrium plane is to serve as a spacer between two CuO_2 planes. In Y-123, the Cu–O chains are known to play an important role in superconductivity [74]. T_c becomes maximum near 92 K

when δ ~ 0.15 and the structure is orthorhombic. Superconductivity disappears at δ ~ 0.6, where the structural transformation of YBCO occurs from orthorhombic to tetragonal symmetry [75]. These are shown in Fig. 1.3.

1.5 Fabrication of bulk REBCO superconductors

For realizing applications, bulk REBCO material has to be processed into near-net shape by a process that simultaneously develops microstructures that support high current densities to high magnetic fields [76]. The method chosen for processing REBCO samples has considerable influence on the properties of the end products. It is now well established that the superconducting properties of HTS are limited by high angle grain boundaries between randomly oriented grains due to their intrinsic weak link nature [77]. The development of texture in the material that aligns the ab-planes of individual grains in multi-grain samples is, therefore, essential if bulk HTS supporting high current densities are to be fabricated for applications. Additionally, it is also necessary to introduce defects of suitable sizes and density to aid flux pinning to high magnetic fields [78]. This requires that one needs to understand the flux pinning phenomenon in the REBCO material.

The flux pinning process in YBCO is a very complex phenomenon. It was found that the transition temperature of Y-123 superconductor is very sensitive to the oxygen content. The oxygen deficient regions act as low T_c phases and aid flux pinning at fields in the range of 2- 3 Tesla [79]. Recent studies show that oxygen defects, stacking faults, dislocations, twin boundaries, and columnar defects introduced by ion irradiations are found to be effective pinning centers in YBCO [80-83]. Jin et al. [21] suggested that fine-scale defects in YBCO may act as pinning centers. Furthermore, although the exact flux pinning mechanism of Y-123/Y-211 is still unknown, it is widely accepted that both mechanical properties and flux pinning of YBCO are improved by the incorporation of fine Y-211 particles in Y-123 matrix [68, 84].

It is known that the flux pinning is greatly affected by the size of defects [78, 85]. The defects depending on their spacing play an important role in affecting the flux pinning. The contribution of the defects to flux pinning is normally observed as peak effect observed in magnetization hysteresis loops recorded [86]. These effects are also reflected in the field dependence of current densities. The relation between the vortex lattice spacing (a_f) and the observed peak field (H_p) is shown below.

$$H_p = \frac{2\Phi_0}{\sqrt{3}a_f^2} \quad .... \ (1.1)$$

where Φ_0 is the flux quantum $\left(= \frac{h}{2e}\right)$ and a_f is the vortex lattice spacing.

To date, the effectiveness of possible pinning centers has not been established. However, there is much evidence that the flux pinning of YBCO can be further enhanced through chemical doping of Pt, Rh, CeO_2 etc. [87, 88]. It is found that Y site in YBCO when doped with certain metals could increase the intra-grain J_c [87, 89]. Hence chemical doping resulted as a very effective method for improving J_c. Since this a non-destructive method and aids enhancement of J_c, is of great importance both for physical understanding and practical applications.

Fabrication of large single grain REBCO superconductors can lead to large current loops and hence can support high current densities [90]. In fact, the current densities supported by sintered Y-123 with random grain orientations and no additionally introduced flux pinning centres can be as low as 100 Acm^{-2} [91]. One needs to investigate the nature of pinning centers which can enhance J_c at high fields and optimize the methods to introduce them into bulk REBCO superconductors. Hence, over the last two decades, several efforts have been made [21, 92-98] to develop a processing technique which can lead to large single domains of REBCO superconductors supporting high current density and trapping large magnetic fields, as required for large scale engineering applications, preferably at liquid

nitrogen temperatures. The major developments from the above mentioned efforts are reviewed in the Sections 1.6 and 1.7.

1.6 Melt Growth Process

For the first time, Jin et al. [21] developed a process yielding textured YBCO with a microstructure that supports high current density. It was called the Melt Growth (MG) process. A pseudobinary phase diagram for YBCO is shown in Fig. 1.4
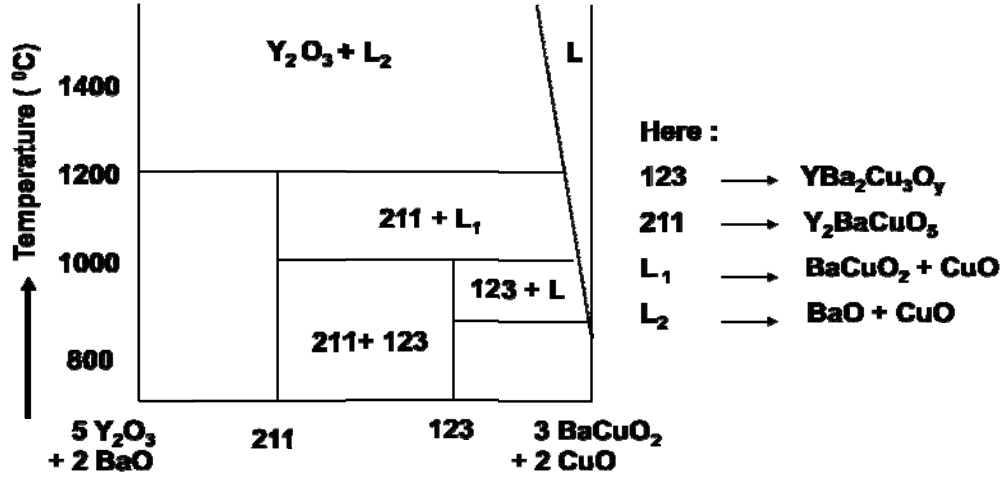
Fig. 1.4. A pseudo-binary phase diagram for the Y-Ba-Cu-O system [*21*]. The peritectic temperature of Y-123 is ~1008°C in air. Above this temperature, solid Y-123 disassociates into solid Y-211 and barium rich liquid phases (L$_1$). Above 1200°C, the Y-211 phase further disassociates to form Y_2O_3 and liquid phases L$_2$ comprising of BaO and CuO.

MG process involves the formation of RE-123 by a reaction between the solid primary phase RE_2BaCuO_5 (RE-211) and liquid phases ($BaCuO_2$ and CuO), on cooling through the peritectic formation temperature (T_p), as described in Eq. 1.1.

$$Y_2BaCuO_5 + 3\ BaCuO_2 + 2\ CuO \rightleftharpoons 2\ YBa_2Cu_3O_{6.5} \text{ ....(1.2)}$$
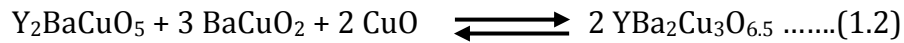
REBCO pellets made are rapidly heated to above its T_p, where RE-211 and liquid phases co-exist. Here, the sample is held for about 0.5 – 1 hour and sample is rapidly cooled down to a point just above the peritectic temperature and then cooled very slowly (at the rate of 0.5 – 1°C per hour) down to temperatures of 900°C

[25]. This resulted in textured products. This led to a significant reduction in the number of grain boundaries. After the melt texturing process, the samples were heated in the oxygen atmosphere in the temperature range 350°C – 650°C, during which the Y-123 phase transforms from the tetragonal state to orthorhombic state exhibiting superconductivity. A typical microstructure obtained in a melt processed YBCO sample is shown in Fig. 1.5.
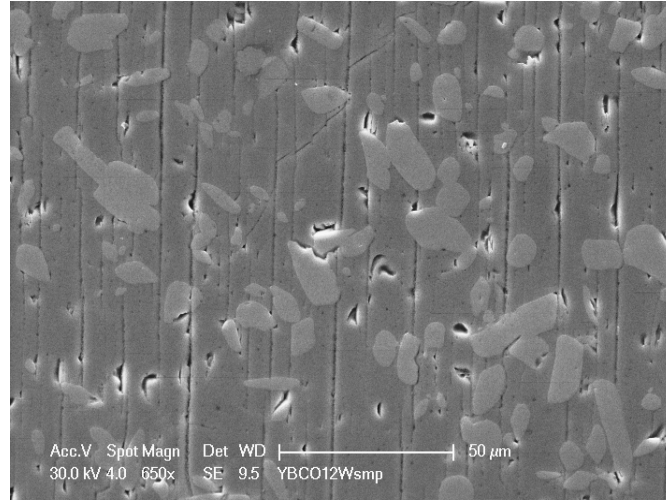
Fig. 1.5. Microstructure of a melt-grown YBCO sample obtained using a scanning electron microscope. Presence of platelets can be seen. Y-211 particles were found to be large in size and acicular in morphology.

The current densities (J_c) obtained in MG processed samples were initially too low and their magnetic field dependence was not good enough for applications [21, 25]. Through modifications to the MG process, the microstructures were altered to introduce optimum amount of RE-211 inclusions in the RE-123 matrix which enhanced the current density supported by the samples to 100 kAcm^{-2} at 77 K at zero field [96].

Numerous variations of melt texturing techniques under a variety of names like Quenched Melt Growth (QMG), Melt Powder Melt Growth (MPMG), Powder Melting Process (PMP), Oxygen Controlled Melt Growth (OCMG), Top Seeded Melt Growth (TSMG) etc. were developed [92-96] with a view to improve the quality of the bulk material. The modified MG processes could improve the magnitudes of

current densities to a reasonable value of ~ 100 kAcm^{-2} at zero field [95]. However, the field dependence of J_c suffered a rapid decay as the magnitudes dropped to $\sim 10^2$ Acm^{-2} by fields of ~ 3 Tesla. Hence efforts were made to grow single grains of REBCO and in this connection, the Top Seeded Melt Growth (TSMG) process was developed by Murakami et al. [96]. TSMG involves seeding the melt growth by a structurally and chemically compatible seed crystal, usually a REBCO material with a higher peritectic decomposition temperature [96]. The peritectic decomposition temperatures of various REBCO materials are given in table 1.2.

Table 1.2. Peritectic temperature (T_p) of various REBCO compounds.

RE in ($REBa_2Cu_3O_{7-\delta}$)	Y	Nd	Gd	Sm	Eu	Dy	Ho	Er	Yb
Peritectic Temperature T_p (^{o}C) (Error: ±5°C)	1005	1068	1030	1054	1046	1010	1005	990	960

The seed crystal initiates the nucleation and growth of RE-123 phase in the incongruent melt, which subsequently solidifies into a single grain during controlled cooling. It was demonstrated that a YBCO disc of 1" diameter fabricated by the TSMG process showed an ability to trap a magnetic field of 17 Tesla at 29 K without fracturing [99]. TSMG process was also extended to fabricate light and mixed rare-earth superconductors [100, 101]. Some of the significant results achieved in systems employing TSMG are discussed below.

YBCO superconductor with nano-sized Y-211 particles could retain J_c in excess of 10 kA cm^{-2} up to fields of 2.5 Tesla at 77 K [102]. Chu et al. have shown that magnetic field up to 18 Tesla could be shielded at 4 K [103, 104]. Tomita and Murakami [99] reported that magnetic field up to 17 Tesla had been trapped at 29 K within a gap of two single-grain pieces of Y-Ba- Cu-O using 19 Tesla magnetization field. The critical current densities of a GdBCO superconductor containing Gd-211 and Pt, fabricated by TSMG process, maintained J_c in excess of 10 kAcm^{-2} up to fields of 2.5 Tesla at 77 K [105]. In mixed REBCO superconductors the current densities

are enhanced due to the presence of defects arising from lattice mismatch effects and also due to the solid solutions that can occur in these materials [100, 101]. For example, a (NSG)BCO superconductor containing Gd-211, Pt and CeO_2, fabricated by TSMG process, showed zero field current density of $\sim$ 50 kA cm^{-2} and the sample supported J_c in excess of 10 kAcm^{-2} up to fields of 5.5 Tesla at 77 K [100].

The MG process takes place in the presence of a substantial amount of liquid phases. Hollow regions can occur in the interior of the samples due to liquid phase outflow, which is difficult to avoid in this process [39, 41, 106]. The samples shrink by $\sim$ 13-22% during the process making it difficult to fabricate complex parts [39]. Due to the outflow of the liquid phases during processing, many major defects like macro-cracks and distortions appear in the final products [41, 106]. In the MG and its derivative processes, RE-211 inclusions were found to be acicular and generally large in size lying in the range 5 – 100 μm [106] thus demanding the need for addition of grain refining compounds. Different methods to limit the coarsening of the RE-211 inclusions during melt growth were tried; these include use of grain refiners like Pt, PtO_2, CeO_2, $BaSnO_3$ etc. [106, 107, 108].

The major developments in the optimization of the properties of REBCO bulk processed by the MG process, were the following. Right after the work of Jin et al. [21], it was discovered that the flux pinning and J_c in the material can be substantially improved by the introduction of RE-211 precipitates in the RE-123 matrix [68, 106]. This was accomplished by working with a composition richer in Y-211 in the pseudo-binary phase diagram of Y-123 shown in Fig. 1.4. This led to a microstructure with Y-211 precipitates in a textured Y-123 matrix [92-94]. At lower concentrations of excess Y-211, the precipitates were large and acicular; and the improvement in current density was not substantial [109]. Optimizing the amount of Y-211 inclusions led to higher J_c and better dependence of J_c on H [110]. The precipitates also became finer and more spherical with increasing concentration of

Y-211 in the Y-123 matrix [110]. An optimum amount of 30% of Y-211 was reported to yield the best performance in the earlier papers [111].

Numerous papers have reported on the addition of silver to the Y-123 while melt processing [112-114]. This led to the closing of the inter-platelet gaps in the melt processed Y-123 [113]. In some cases, there were reports of improvement in J_c through Ag addition. In Ag-added YBCO samples, the current density achieved was $\sim$ 90 kAcm^{-2} at zero field at 77 K [114]. Also, the mechanical properties of the bulk melt processed Y-123 was sought to be improved by silver addition [115, 116]. Another landmark development was the finding that in mixed rare earth systems, fabricated by MG process, remarkable high current densities up to high magnetic fields can be obtained [100]. The processing of the mixed rare earth systems has to be done under carefully chosen atmospheres because REBCO compounds with Gd, Sm and Nd can form solid solutions such as $RE_{1+x}Ba_{2-x}Cu_3O_y$ [95]. The lattice mismatch in mixed rare earth systems were reported to yield the best reported current densities as function of magnetic fields. $(Nd_{0.33}Sm_{0.33}Gd_{0.33})Ba_2Cu_3O_y$ is reported to exhibit current densities of $\sim$ 93 kAcm^{-2} at zero field at 77 K [101].

1.7 Infiltration Growth Process

To overcome the difficulties associated with the MG process, the Infiltration Growth (IG) process was developed [97]. It allows near-net shape fabrication of REBCO with microstructures that support high current density [106, 117]. IG process involves the infiltration of liquid phases (BaCuO$_2$ and CuO) into a porous preform of the primary RE-211 phase and allowing subsequent reaction between them to form RE-123 on cooling below the peritectic formation temperature [6, 23, 24]. The reaction occurring between RE-211 and the liquid phases is shown below.

$$RE_2BaCuO_5 + \{3\ BaCuO_2 + 2\ CuO\} \longrightarrow 2\ REBa_2Cu_3O_{6.5}\ ....(1.3)$$
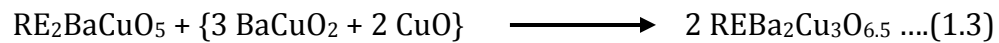
In the IG process, the preform of RE-211 with infiltrated liquid is subjected to a slow cooling (i.e. at ∼ 0.5ºC per hour) through its T_p. This slow cooling is continued to a temperature of ∼ 30ºC below T_p. The products thus obtained were oxygenated for about 60 – 100 hours at a temperature of 460ºC in flowing oxygen. At this stage, the RE-123 phase transforms from the tetragonal to orthorhombic state.

Cloots et al. [106] reviewed different techniques available for RE-123 bulk fabrication. They discussed various parameters that affect the final microstructures. They have compared the IG process with the TSMG process. A comparison between the two processes can be done with the help of Fig. 1.6.
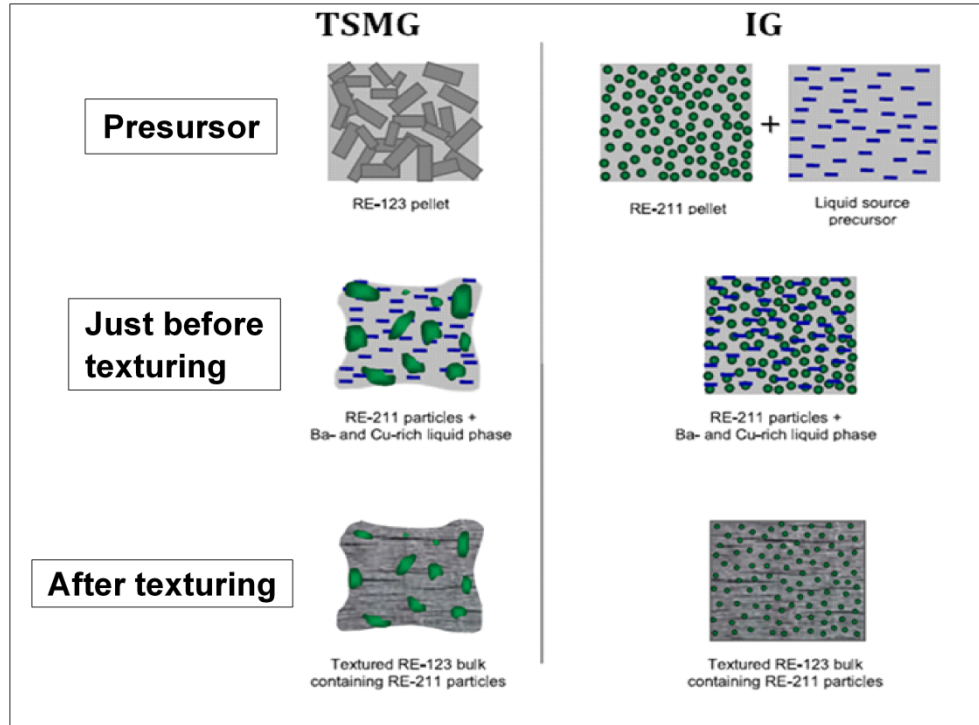
Fig. 1.6. A schematic sketch comparing TSMG and IG processes [106].

In the TSMG process, the RE-123 phase melts at temperatures above T_p during which the solid RE-123 phase disassociates to form solid RE-211 and liquid phases. Below T_p, the two recombine to yield textured RE-123 with RE-211

precipitates. A substantial amount of shrinkage and distortions accompany the process. The RE-211 particles in the final microstructure are mostly large and acicular. The outflow of liquid phases can also cause cracks and distortions in the final product. On the other hand, in the IG process, liquid phases are infiltrated into a preform of the required geometry at high temperature and the two are recombined below the peritectic formation temperature to form RE-123. Since the RE-211 does not melt during the texturing step and since a continuous supply of liquid phases are provided throughout the texturing process, there are no distortions or shrinkage in the final product. There are no major macroscopic defects like porosity in the final product. Also, the RE-211 grains are substantially refined in the final product. The IG process has been applied to several yttrium [117-119] and light rare earth superconducting systems such as Nd–Ba–Cu–O [120], Sm–Ba–Cu–O [121], Gd–Ba–Cu–O [122] and Dy–Ba–Cu– O [123]. Fabrication of hollow cylinders [117], superconducting foams [124], fabrics [125, 126] and large single crystals for application as trapped field magnets [127] has been reported.

Gd-123 single-grain bulk superconductor has been fabricated successfully by IG technique with a diameter of ~ 30 mm [127]. IG processed YBCO superconductors containing nano-dopants and grain refiners (CeO_2) exhibit current densities of ~ 100 kAcm^{-2} at 77 K [128]. The samples retained current densities of ~ 10^3 Acm^{-2} up to applied fields of 3.5 Tesla at 77 K. The irreversibility field reported for this material was less than 5 Tesla at 77 K [128]. The irreversibility field (H_{irr}), defined as the field by which J_c reaches 100 Acm^{-2}, of YBCO is in the range of 3 – 5 Tesla at 77K [127, 128].

An important contribution was the development of a generic seed by the Cambridge group [129] to avoid hot seeding. A generic seed crystal with higher T_p was prepared which can aid the nucleation of RE-123 and leads to large grain REBCO superconductors. Nd-123+ 12mol% Nd-422+1wt.%MgO was used as seed material. Yet another breakthrough was the addition of excess Ba in RE-123

compounds which resulted in minimizing the formation of solid solutions [130]. At a definite amount of excess BaO_2 content, the RE-123 samples have eliminated solid solution formations. Large sized REBCO samples (up to 1" diameter) exhibiting considerable trapped magnetic fields of ~ 1.5 T at 77 K have been realized following these improved processing routes [131].

1.8 Motivation of the present work

As shown in the review above on melt growth processed REBCO, optimization of the RE-211 content in the RE-123 matrix dramatically improved the current carrying capacity of the material from ~100 Acm^{-2} to ~ 50 $kAcm^{-2}$ at 77 K in zero field [21, 25]. Y-211 content in MG processed YBCO superconductor can be conveniently controlled by choosing a suitable starting composition as Y-123 + x % Y-211. The inherent advantages of the Infiltration Growth process in comparison with the Melt Growth process have been brought out above. The work on the optimization of RE-211 content in melt processed RE-123 and the advantages that followed from it motivated us to try and optimize the RE-211 content in IG processed RE-123.

One can hope to modify the content and characteristics of the Y-211 in the final microstructure of IG processed samples by controlling the particle size of the initial Y-211 powders, by limiting their grain growth during sintering, adjusting the level of porosity in the preform and by controlling heat treatments after the infiltration of liquid phases. Mahmood et al. [131] studied the effect of preform sintering temperature on the properties of IG processed Y-123. They reported a decrease in pore volume in the preform (from ~ 12 % to 1.7 %) with increasing sintering temperature, and an increase in J_c from 7.25 $kAcm^{-2}$ to 12.2 $kAcm^{-2}$ at zero field and 77 K, after IG processing. Their results confirmed the importance of monitoring and optimizing the preform fabrication process for enhancing the current carrying capacity of IG processed samples. Since sintering the Y-211

preform for prolonged durations at high temperature as done in Mahmood's work, was observed to cause Y-211 grain growth, we looked for alternative ways of controlling the characteristics of the Y-211 preforms used in IG process.

Though the IG process has been acknowledged to be superior to the MG process [106, 117] because it minimizes shrinkage, cracks and distortions in the final product, various reports discuss the occurrence of inhomogeneity in the distribution of the Y-211 particles [119, 132]. This causes a wide variation, across the sample volume, in the properties such as microstructure and current densities [119, 132]. In addition, the samples also show distribution in critical temperature (T_c) [133]. The problem of inhomogeneity in the RE-211 distribution and hence the non-uniformity in $J_c(H)$ has been existing even in MG processed samples [134-136].

In literature, the inhomogeneities in the distribution of RE-211 inclusions in RE-123 matrix were attributed to pushing effects [137, 138]. It was reported that during the growth of RE-123, particles of RE-211 get pushed along with the RE-123 growth front causing inhomogeneity in their distribution across the volume of the bulk. For instance, the Y-211 content in seeded IG processed bulk YBCO material showed a variation of ~ 5 – 30% across the sample volume [132]. The Y-211 content close to seed crystal was found to be very low compared to the regions away from the seed crystal. These inhomogeneities in RE-211 distribution led to non-uniformities in the $J_c(H)$ across the volume of the samples [132]. The variation in the magnitude of J_c was as severe as ~ 17 % when measured across the volume of the bulk. This has been an issue of serious concern.

We used very fine Y-211 particles of ~1 μm size prepared by chemical methods in the work reported in this thesis. The preform compaction pressure and its sintering temperature were optimized to yield the best possible YBCO products. The optimized YBCO sample yielded current densities in excess of 10^3 Acm^{-2} to fields as high as 6.5 Tesla at 77 K. The superior $J_c(H)$ was obtained in a simple YBCO system with no added

grain refiners / nano-dopants, and also a very uniform microstructure with fine Y-211 particles motivated us to make a thorough microstructural investigation of our samples. A systematic study of our materials was done using techniques such as Field Emission Scanning Electron Microscopy, Electron Back Scattered diffraction and Transmission Electron Microscopy. We have correlated the observed microstructures to the high current densities to large applied magnetic fields in the optimized material. Also, a systematic study of the introduction of silver into the Y-123 matrix under the optimized processing conditions is presented in the thesis. The results of combining directional solidification with the modified IG process are also discussed.

1.9 Organization of the thesis

The **first** chapter presents a brief introduction to the area of superconductivity in general and high temperature superconductivity in particular. Various efforts reported in the literature to improve the current density at zero field $J_c(0)$ and its field dependence $J_c(H)$ are discussed. This chapter discusses the aims of the present work which include

(a) studying the effect of preform fabrication conditions on the final microstructures and $J_c(H)$ in the bulk YBCO superconductors fabricated by the modified IG process

(b) optimizing the methodology of introducing metallic Ag in IG processed bulk YBCO superconductors to obtain spatial uniformity in the distribution of Y-211 and Ag.

(c) fabricating YBCO superconductors in short-time durations by integrating directional solidification with seeded POIGP

(d) arriving at correlations between the microstructural features and the field dependence of J_c to understand the origin of flux pinning.

The **second** chapter describes initially the preparation of precursor powders and their characterization. Confirmation of phase formation of Y-123 and Y-211 by

X-ray diffraction studies is discussed. The method of fabricating YBCO and YBCO/Ag composites by preform Optimized Infiltration and Growth process (POIGP) and Directionally Solidified Preform Optimized Infiltration and Growth Process (DS-POIGP) are discussed. The arrangements of the preform pellets used, the heat treatments followed and the oxygenation process are described.

In order to characterize the samples fabricated and to study the electrical, magnetic and microstructural properties, dc electrical resistivity set up, ac susceptometer, Physical Property Measurement System (PPMS), Optical Microscope, Field-Emission Scanning Electron Microscope and Transmission Electron Microscope etc. were employed. Orientation studies were carried out using Electron Back scattered diffractometer. This chapter provides a concise description of each of the experimental techniques used in the present work, discussing briefly their principles of operation.

The **third** chapter describes the effect of preform compaction pressure on the final microstructures and the resultant current densities, $J_c(H)$ in the YBCO superconductors fabricated by POIGP. Initial part of the chapter demonstrates the need for pre-sintering the Y-211 preforms prior to infiltration of liquid phases in the IG process. The parameters associated with sintering temperature and sintering duration of the Y-211 preforms, were optimized. It is observed that preform optimization has led to improved microstructures with reduced porosity, and with uniformity in the distribution of fine sized Y-211 particles in the Y-123 matrix.

Preforms of Y-211 were made under different compaction pressures in the range 300 MPa to 540 MPa and were subjected to pre-sintering followed by liquid phase infiltration and IG process. The temperature dependences of electrical resistivity and ac susceptibility were carried out. Sharp superconducting transitions at ~ 92 K with transitions widths of ~ 1- 2 K were obtained for all the samples which establish the high quality of the POIGP samples.

A detailed microstructural characterization was carried out on the samples employing a Field Emission Scanning Electron Microscope (FE-SEM). The effect of preform compaction pressure on the final microstructures in terms of cracks, pores and size of Y-211 particles is studied. In all the POIGP samples, spatial homogeneity in the distribution of Y-211 particles in the matrix of Y-123 is established by investigating specimens from different regions of the samples. It is observed that the porosity and the macro-crack density have decreased significantly with increasing preform compaction pressure. The variation in Y-211 content was < 4%, when measured across the volume of the samples. The Y-211 particles were found to be in the size range 200 nm – 4 μm.

Field dependence of current density, $J_c(H)$ in the present POIGP samples is superior to those reported in literature on YBCO samples without nano-dopants or grain refiners [21-25, 117-119]; the sample whose preform was fabricated under a compaction pressure of 460 MPa showed the best field dependence of J_c with $J_c(0)$ of 19.2 kA cm^{-2} at 77 K. On application of magnetic field this sample maintained J_c better than 10^3 Acm^{-2} up to applied fields of 6.5 Tesla at 77 K and better than 25 kAcm^{-2} up to 13 Tesla at 50 K. We observed that homogeneous distribution of Y-211 particles has also resulted in spatial uniformity in $J_c(H)$.

In order to understand the nature of flux pinning in the POIGP samples, field dependences of flux pinning force (F_p) and normalized current density $J_c(H)/J_c(0)$ are studied. It is observed that the $J_c(H)$ is governed by two different pinning mechanisms, one active at low fields and the other active at high fields. Interfacial defect density is identified to govern the flux pinning at low fields as suggested in literature [68, 78 106]. The origin of pinning at high fields is further investigated and presented later in Chapter Six.

The **fourth** chapter describes the fabrication of YBCO/Ag composites by POIGP. Two different methods were explored to introduce metallic Ag into the YBCO

superconductors, one by adding Ag to Y-211 preform directly and the other by adding Ag along with liquid phases during infiltration. The widths and fraction of macro-cracks were minimized successfully with Ag addition along with liquid phases. The distribution of Y-211 and Ag particles were found to be spatially homogeneous in the final microstructures of these samples. It was found from Energy Dispersive Spectroscopy (EDS) / Wavelength Dispersive Spectroscopy (WDS) studies that Ag when introduced along with the liquid phases fuses the macro-cracks. Further it is also observed that Ag addition refines the size of Y-211 particles. The field dependences of critical current densities were measured in the YBCO/Ag samples. The optimized samples exhibited zero field J_c of 13.3 kAcm^{-2} and 7 kAcm^{-2} respectively at 77 K and maintained J_c in excess of 10^3 Acm^{-2} up to fields of 2.7 Tesla and 100 Acm^{-2} up to fields of 6 - 8 Tesla at 77 K, exceeding the performance reported for YBCO/Ag composites in the literature so far [112-114, 139, 140].

The **fifth** chapter presents the results of integrating the directional solidification with preform optimized Infiltration growth process (PO-DSIG). This method has helped in fabricating YBCO samples in short time durations of ∼ 30 hours instead of ∼ 130 hours and may be significant in the fabrication of YBCO wires.

The effect of preform compaction pressure on the end microstructures of the DS-POIGP samples was studied. The critical current densities were measured and the samples were found to show nearly a flat $J_c(H)$ response to fields as high as 13 Tesla at 50 K. The sample, fabricated under a preform compaction pressure of 460 MPa, showed a zero field J_c of 10 kAcm^{-2} and maintained a J_c better than 100 Acm^{-2} up to applied fields of 6 Tesla at 77 K. These values are found to be similar to the ones reported in the literature obtained through long heat treatments [102].

The **Sixth** chapter of the thesis is dedicated to a study of the origin of observed high current densities to high applied magnetic fields in the optimized YBCO sample made through POIGP. The fact that enhanced current densities are achieved without any additives to refine the Y-211 particle size or dopants to incorporate additional flux pinning, has provided motivation to carry out detailed study of microstructural features. The peak field H_p, where flux pinning shows an enhancement, is obtained from magnetic hysteresis (*M-H*) loops recorded at several temperatures in the range 15 – 89 K. It is observed that H_p remains temperature independent up to temperatures of 77 K suggests the source of pinning to be temperature independent structural defects. Investigations employing TEM showed presence of nano-sized defects of ~ 15 – 50 nm in the Y-123 matrix. EBSD studies carried out showed the presence of high angle domain boundaries in the size range 50 - 200 nm. The orientation studies were also carried out on the optimized sample using this technique. Pole figure analysis showed the presence of three mutually orthogonal orientations of Y-123 phase.

Wide spread twinning on a nanometer-scale in the Y-123 matrix was observed in all the POIGP samples in FE-SEM studies. The widths of the twin variants were in the range 25 to 100 nm. It was observed that in areas where the Y-211 grains are in close proximity crossing twins were observed indicating high twin boundary (TB) density. The TB energy was computed and was found to be the lowest for the optimized sample, fabricated under preform compaction pressure of 460 MPa. Twinning was also observed in the YBCO and YBCO/Ag composites fabricated by POIGP and DS-POIGP. The presence of various types of defects with different size ranges are discussed, which appear to be the reason for the observation of enhanced flux pinning in a wide range of applied fields resulting in a flat $J_c(H)$ response.

The **Seventh** chapter presents a summary of the work done and the conclusions drawn from the present investigations.

An **Appendix** is also included in this thesis which discusses briefly the basic properties of superconductors relevant to the present work. A brief discussion on the possible applications of bulk REBCO superconductors is also given.

References

[1]   Kammerlingh Onnes H 1911 *Leiden Commun.* **120b** 1226

[2]   Narlikar A V and Ekbote S N 1983 *Superconductivity and Superconducting Materials* (South Asian Publishers, New Delhi, India) p 12

[3]   Easterling K E *Tomorrow's materials* 1990 Ed. II (Inst. Of Metals, London) p 112

[4]   Mathias B T, Geballe T H, Geller S and Corenzwit E 1954 *Phys. Rev.* **95** 1435

[5]   Kunzler J E 1961 *Rev. Mod. Phys.* **33** 501

[6]   Tilley R 2004 *Understanding Solids: The Science of Materials* (Wiley Publishers, West Sussex, England) p 415

[7]   Bednorz J and Muller K A 1986 *Z. Phys. B: Cond. Matter.* **64** 189

[8]   Wu M X, Ashburn J R, Torang C J 1987 *Phys. Rev. Lett.* **58** 908

[9]   Maeda H, Tanaka Y, Fukutumi M, Asano T 1988 *Jpn. J. Appl. Phys.* **27** L209

[10]   Sheng Z Z, Hermann A M 1988 *Nature* **332** 138

[11]   Chu C W, Gao L, Chen F, Huang Z J, Meng R L and Xue Y Y 1993 *Nature* **365** (6444): 323

[12]   Tallon J L, Buckley R G, Gilberd P W, Presland M R, Brown I W M, Bowden M E, Christian L A and Goguel R 1988 *Nature* **333** (6169): 153

[13]   Gao L, Xue Y Y, Chen F, Xiong Q, Meng R L, Ramirez D, Chu C W, Eggert J H and Mao H K 1994 *Phys. Rev. B* **50** 4260

[14]   Nagamatsu J, Nakagawa N, Muranaka T, Zenitani Y and Akimitsu J 2001 *Nature* **410** 63

[15]   Ganin A Y, Takabayashi Y, Khimyak Y Z, Margadonna S, Tamai A, Rosseinsky M J and Prassides K 2008 *Nature Mater.* **7** 367

[16] Takahashi H, Igawa K, Arii K, Kamihara Y, Hirano M and Hosono H 2008 *Nature* **453** 376

[17] Kamihara Y, Watanabe T, Hirano M and Hosono H 2008 *J. Am. Chem. Soc.* **130** 3296

Bharathi A, Sharma S, Paulraj S, Satya A T, Hariharan Y and Sundar C S 2010 *Physica C* **470** 8

Awana V P S, Meena R S, Pal A, Vajpayee A, Rao K V and Kishan H 2011 *Euro. Phys. J. B* **79** 139

[18] Day C 2009 *Phys. Today* **62** 36

[19] Subramanian M A, Torardi C C, Calabrese J C, Gopalakrishnan J, Morrissey K J, Askew T R, Flippen R B, Chowdhry U and Sleight A W 1988 *Science* **239** 1015

[20] Golovashkin A I, Ivanenko O M, Kudasov Yu B, Mitsen K V, Pavlovsky A I, Platonov V V and Tatsenko O M 1991 *Physica C* **185-189** 1859

Sharma S V, Sudhakari N, Majumdar A K, Gupta K P and Bahadur D 1993 *J. Mater. Sci. Lett.* 12 1371

[21] Hari Babu N, Shi Y-H, Pathak S K, Dennis A R and Cardwell D A 2011 *Physica C* **471** 169

[22] Murakami M, Fujimoto H, Gotoh S, Yamaguchi K, Koshizuka N and Tanaka S 1991 *Physica C* **185-189** 321

[23] Hari Babu N, Rajasekharan T and Seshu Bai V 1998 *Eur. Phys. J. B.* **4** 55

[24] Sudhakar Reddy E and Rajasekharan T 1998 *Supercond. Sci. Technol.* **11** 523

[25] Hari Babu N, Kambara M, Shi Y-H, Cardwell D A, Tarrant C D and Schneider K R 2002 *Supercond. Sci. Technol.* **15** 104

[26] Jin S, Mavoori H, Bower C and van Dover R B 2001 *Nature* **411** 563

[27] Buzea C and Yamashita T 2001 *Supercond. Sci. Technol.* **14** R115

Sinha B B, Kadam M B, Mudgel M, Awana V P S, Kishan H and Pawar S H 2010 *Physica C* **470** 25

[28] Varghese N, Vinod K, Rahul S, Devadas K M, Thomas S, Pradhan S and Syamaprasad U 2011 *J. Appl. Phys.* **109** 033902

Vajpayee A, Jha R, Srivastava A K, Kishan H, Tropeano M, Ferdeghini C and Awana V P S 2011 *Supercond. Sci. Technol.* **24** 045013

[29] Subramanyam G and Boolchand P 1999 *Superconductors: Processing of High-T_c Bulk, Thin Film, and Wires* (Wiley)

[30] Tovar H and Fortier J 2009 *Superconducting magnets and superconductivity* (Nova Science Publishers Inc. New York)

[31] Heine K, Tenbrink J and Thoner M 1989 *Appl. Phys. Lett.* **55,** 2441

[32] Kikuchi M, Ayai N, Ishida T, Tatamidani K, Hayashi K, Kobayashi S, Ueno E, Yamazaki K, Yamade S, Takaaze H, Fujikami J and Sato K-I 2008 *SEI Tech. Rev.* **66** 73

[33] Masur L, Parker D, Tanner M, Podtburg E, Buczek D, Scudiere J, Caracino P, Spreafico S, Corsaro P and Nassi M 2001 *IEEE Trans. Appl. Supercond.* **11** 3256

[34] Nielsen M S, Bech J I, Eriksen M, Bay N 2002 *Physica C* **372–376** 966

[35] Kang M, Kim Y, Lee H, Cha G and Ryu K 2011 *IEEE Trans. Appl. Supercond.* **21** 2271

[36] Cohen L F, Totty J T, Perkins G K, Doyle R A and Kadowaki K 1997 *Supercond. Sci. Technol.* **10** 195

[37] Togano K, Kumakura H, Maeda H, Yanagisawa E and Takahashi K 1988 *Appl. Phys. Lett.* **53** 1329

[38]   Yamade S, Ayai N, Fujikami J, Kobayashi S, Ueno E, Yamazaki K, Kikuchi M, Kato T, Hayashi K, Sato K, Kitaguchi H and Shimoyama J 2007 *Physica C* **463–465** 821

[39]   Viswanath N V N, Rajasekharan T, Harish Kumar N, Menon L and Malik S K 1998 *Supercond. Sci. Technol.* **11** 420

[40]   Meslin S, Iida K, Hari Babu N, Cardwell D A and Noudem J G 2006 *Supercond. Sci. Technol.* **19** 711

[41]   Muralidhar M and Murakami M 2000 *Physica C* **341-348** 2431

[42]   Chen S-Y, Hsiao Y-S, Chen C-L, Yan D-C, Chen I-G and Wu M-K 2008 *Mater. Sci. Eng. B* **151** 31

[43]   Coombs T A 2010 *Physica C* **470** 1845

[44]   Li T Y, Cheng L, Yan S B, Sun L J, Yao X, Yoshida Y and Ikuta H 2010 *Supercond. Sci. Technol.* **23** 125002

[45]   MacManus-Driscoll J L 1998 *Annu. Rev. Mater. Sci.* **28** 421

[46]   Foltyn S R, Civale L, MacManus-Driscoll J L, Jia Q X, Maiorov B, Wang H and Maley M 2007 *Nature. Mater.* **6** 631

[47]   Shiohara Y, Yoshizumi M, Izumi T and Yamada Y 2007 *Physica* C **463–465** 1

[48]   Selvamanickam V Dackow J and Xie Y-Y 2009 *Progress in SuperPower's 2G HTS Wire Development Program* US Department of Energy Superconductivity for Electric Systems

         Irjala M, Huhtinen H, Jha R, Awana V P S and Paturi 2011 *IEEE Trans. Appl. Supercond.* **21** 2762

         http://www.htspeerreview.com/2009/pdfs/summaries/day%201/joint/2-Joint-Progress-in-SuperPowers-2G-HTS.pdf

[49]   Ibi A, Iwai H, Takahashi K, Muroga T, Miyata S, Watanabe T, Yamada Y and Shiohara Y 2005 *Physica C* **426–431** 910

[50]   Liu L, Zhao Z, Liu H and Li Y 2010 *IEEE Trans. Appl. Supercond.* **20** 1553

[51]   Yang J, Zhang H, Wang S M, Lin C G, Shi D Q and Dou S X 2011 *Physica C* **471** 233

[52]   Shiohara Y, Yoshizumi M, Izumi T and Yamada Y 2008 *Supercond. Sci. Technol.* **21** 034002

[53]   Verebelyi D T, Schoop U, Thieme C, Li X, Zhang W, Kodenkandath T, Malozemoff A P, Nguyen N, Siegal E, Buczek D, Lynch J, Scudiere J, Rupich M, Goyal A, Specht E D, Martin P and Paranthaman M 2003 *Supercond. Sci. Technol.* **16** L19

[54]   Murakami M 2007 *Int. J. Appl. Ceram. Technol.* **4** 225

[55]   Nagaya S, Kashima N, Minami M, Kawashima H and Unisuga S 2001 *IEEE Trans. Appl. Supercond.* **11** 1649

[56]   Oka T, Itoh Y, Yanagi Y, Yoshikawa M, Ikuta H and Mizutani U 2000 *Physica C* **335** 101

[57]   Scheller H, Rothfeld R, Werfel F and Gehring M 2002 *IEEE Trans. Appl. Supercond.* **12** 1

[58]   Driscoll D, Dombrovski V and Zhang B 2000 *IEEE Power Eng. Rev.* **20** 12

[59]   Malozemoff A P   2007 *Nature Mater.* **6** 617

[60]   Ganados X, Puig T, Teva J, Mendoza E and Obradors X 2001 *IEEE Trans. Appl. Supercond.* **11** 2406

[61]   Han Y H, Lee J-S, Sung T-H, Han S-C, Kim Y-C and Kim S-J 2002 *Physica C* **372-376** 1457

[62]   Murakami M 1993 *Appl. Supercond.* **1** 1157

[63]   Akiyama S *Noncontact rotary apparatus* 2000 Patent Abstracts of Japan Appl. No. 10298750

[64]   Watson J H P and Younas I 1998 *Mater. Sci. Eng. B* **53** 220

[65]   U Mizutani, Masuda T, Yanagi Y, Itoh Y and Ikuta H 2003 *Ceram. Trans.* **141** 273

[66]   Nakamura T, Kita R, Miura O, Ichinose A, Matsumoto K, Yoshida Y, Mukaida M and Horii S 2007 *Physica C* **463-435** 540

[67]   Baranauskas A, Jasaitis D, Kareiva A, Haberkorn R and Beck H P 2001 *J. Euro. Ceram. Soc.* **21** 399

[68]   Lee D F, Selvamanickam V and Salama K 1992 *Physica C* **202** 83

[69]   Cyrot M and Pavuna D 1992 *Introduction to Superconductivity and high T_c materials* (World Scientific, Singapore)

         Jin S, Tiefei H, Kammlott G W, Fastnacht R A and Graebner J E 1991 *Physica C* **173** 75

[70]   Li J, Fang M, Hu G, Zhang X, Jiao Z, Zhang Q, Zhang Y, Jin X and Yao X 1992 *Chin. Phys. Lett.* **9** 667

[71]   Yamada T, Ikuta H, Yoshikawa M, Yanagi Y, Itoh Y, Mizutani U 2003 *Physica C* **392–396** 623

[72]   Bell J M 1988 *Phys. Rev. B.* **37** 541

[73]   Salama K, Parih A S and Woolf L 1993 *Appl. Phys. Lett.* **68** 1996

[74]   Gupta M and Gupta R P 1991 *Physica C* **185-189** 851

[75]   Hauck J 1996 *Supercond. Sci. Technol.* **9** 1033

[76]   Krabbes G, Fuchs G and Canders W-F 2005 *High Temperature Superconductor Bulk Materials: Fundamentals - Processing - Properties Control - Application Aspects* (Wiley, GmbH, KGaA, Weinheim)

[77]   Salama K, Selvamanickam V, Gao L and Sun K 1989 *Appl. Phys. Lett.* **54** 2352

[78]   Salama K, Selvamanickam V and Lee D F 1993 *Physica C* **209** 187

[79]   Chudnovsy E M 1990 *Phys. Rev. Lett.* **65** 3060

[80]   Ramesh R, Jin S, Nakahara S and Tefel T H 1990 *Appl. Phys. Lett.* **57**1458

[81]   Kes P H 1991 *Physica C* **185–189** 288

[82]   Civale L, Marwich A D, Thompson J R, Krusin-Elbaum L and Holtzberg F 1991 *Phys. Rev. Lett.* **67** 648

[83]   Ekin J W, Salama K and Selvamanickam V 1991 *Appl. Phys. Lett.* **59** 360

[84]   Leenders A, Ullrich M and Freyhardt H C 1999 *IEEE Trans. Appl. Supercond.* **9** 2074

[85]   Nakamura M, Hirayama T, Yamada Y, Ikuhara Y and Shiohara Y 1996 *Jpn. J. Appl. Phys.* **35** 3882

[86]   Suematsu H, Okamura H, Nagaya S and Yamauchi H 1999 *Supercond. Sci. Technol.* **12** 274

[87]   Ogawa N, Yoshida M, Hirabayashi I and Tanaka S 1992 *Supercond. Sci. Technol.* **5** S89

[88]   Kim C J, Kim K B, Won D Y, Moon H C, Suhr D S, Lai S H and McGinn P J 1994 *J. Mater. Res.* **9** 1952

[89]   Feng Y, Zhou L, Du S, Wu X, Tholence J L, Vallier J C, Monceau P, Yin B, Li J, Zhao Z and Zhang Y 1996 *J. Appl. Phys.* **80** 993

[90]   Saitoh T, Segawa K, Kamada K, Sakai N, Segawa T, Yoo S I and Murakami M 1997 *Physica C* **288** 141

[91]   Stucki F, Brüesch P and Baumann T 1988 *Physica C* **153-155** 200

[92]   Jin S, Tiefel T H, Sherwood R C, Davis M E, van Dover R B, Kammlott G W, Fastnacht R A and Keith H D 1988 *Appl. Phys. Lett.* **52** 2074

[93] Fujimoto H, Murakami M, Gotoh S, Koshizuka N and Tanaka S 1990 *Adv. Supercond.* **2** 285

[94] Murakami M, Morita M, Doi K and Miyamoto K 1989 *Jpn. J. Appl. Phys.* **28** 1189

[95] Yoo S I, Sakai N, Takaichi H and Murakami M 1994 *Appl. Phys. Lett.* **65** 633

[96] Takebayashi S and Murakami M 2001 *Supercond. Sci. Technol.* **14** 741

[97] Sudhakar Reddy E and Rajasekharan T 1998 *J. Mater. Res.* **13** 2472

[98] Hari Babu N, Kambara M, Smith P J, Cardwell D A and Shi Y 2000 *J. Mater. Res.* **15** 1235

[99] Tomito M and Murakami M 2003 *Nature* **421** 517

[100] Muralidhar M, Koblischka M R and Murakami M 2000 *Supercond. Sci. Technol.* **13** 693

[101] Muralidhar M, Jisra M, Sakai N and Murakami M 2003 *Supercond. Sci. Technol.* **16** R1

[102] Yeoh W K, Pathak S K, Shi Y-H, Dennis A R, Cardwell D A, Hari Babu N, Iida K and Strasik M 2009 *Supercond. Sci. Technol.* **22** 065011

[103] Gao L, Xue Y Y, Meng R L, Chu C W, Hannahs S, Thang V and Rubin L 1994 *Appl. Phys. Lett.* **65** 907

[104] Chen I-G, Jamn G, Hsu J-C and Wu M K 1997 *J. Appl. Phys.* **81** 4947

[105] Cardwell D A, Shi Y-H, Hari Babu N, Pathak S K, Dennis A R and Iida K 2010 *Supercond. Sci. Technol.* **23** 034008

[106] Cloots R, Koutzarova T, Mathieu J-P and Ausloos M 2005 *Supercond. Sci. Technol* **18** R9

[107] Kim S J 2006 *J. Ceram. Process. Res.* **7** 235

[108] Muralidhar M, Jisra M, Nariki S and Murakami M 2001 *Supercond. Sci. Technol*. **14** 832

[109] Salama K and Lee F Dominic 1994 *Supercond. Sci. Technol*. **7** 177

[110] Nariki S, Sakai N and Murakami M *Supercond. Sci. Technol.* 2005 **18** S126

[111] Hari Babu N, Kambara M, Cardwell D A, Tarrant C D and Schneider K 2002 *Physica C* **372−376** 1183

[112] Mendoza E, Puig T, Varesi E, Carrillo A E, Plain J and Obradors X 2000 *Physica C* **334** 7

[113] Lee D F, Chaud X and Salama K 1991 *Physica C* **181** 81

[114] Joo J, Kim J-G and Nah W 1998 *Supercond. Sci. Technol.* **11** 645

[115] Schatzle P, Krabbes G, Gruss S and Fuchs G, 1999 *IEEE Trans. Appl. Supercond.* **9** 2022

[116] Miyamoto T, Katagiri J, Nagashima K and Murakami M1999 *IEEE Trans. Appl. Supercond.* **9** 2066

[117] Sudhakar Reddy E and Rajasekharan T 1998 *Supercond. Sci. Technol.* **11** 183

[118] Fang H, Zhou Y X, Ravi-Chandar K and Salama K 2004 *Supercond. Sci. Technol.* **17** 269

[119] Meslin S and Noudem J G 2004 *Supercond. Sci. Technol.*, **17** 1324

[120] Chen Y L, Chan H M, Harmer M P, Todt V R, Sengupta S and Shi D 1994 *Physica* C **234** 232

[121] Hari Babu N and Rajasekharan T 1999 *J. Am. Ceram. Soc.* **82** 2978

[122] Sudhakar Reddy E and Rajasekharan T 1999 *Physica* C **316** 279

[123] Mathieu J P, Koutzarova T, Rulmont A, Fagnard J F, Laurent P, Mattivi B, Vanderbemden Ph, AusloosM and Cloots R 2005 *Supercond. Sci. Technol.* **18** S136

[124] Sudhakar Reddy E and Schmitz G J 2002 *Supercond. Sci. Technol.* **15** L21

[125] Sudhakar Reddy E, Noudem J G, Tarka M and Schmitz G J 2000 *Supercond. Sci. Technol.* **13** 716

[126] Sudhakar Reddy E and Schmitz G J 2002 *Supercond. Sci. Technol.* **15** 727

[127] Iida K, Hari Babu N, Shi Y H, Cardwell D A and Murakami M 2006 *Supercond. Sci. Technol.* **19** 641

[128] Cardwell D A and Hari Babu N 2006 *Physica C* **445-448** 1

[129] Hari Babu N, Shi Y, Iida K and Cardwell D A 2005 *Nature Mater.* **4** 476

[130] Shi Y, Hari Babu N and Cardwell D A 2005 *Supercond. Sci. Technol.* **18** L13

[131] Mahmood A, Jun B H, Park H W and Kim C J 2008 *Physica C* **468** 1350

[132] Iida K, Hari Babu N, Withnell T D, Shi Y, Haindl S, Weber H W and Cardwell D A 2006 *Physica C* **445–448** 277

[133] Iida K, Hari Babu N, Shi Y and Cardwell D A 2005 *Supercond. Sci. Technol.* **18** 1421

[134] Jiao Y L, Xiao L, Ren H T, Zheng M H and Chen Y X 2003 *Physica C* **386** 266

[135] Chow J C L, Leung H T, Lo W and Cardwell D A 1998 *J. Mater. Sci.* **33** 1083

[136] Endo A, Chauhan H S and Shiohara Y 1996 *Physica C* **273** 107

[137] Diko P, Zmorayova K, Granados X, Sandiumenge F and Obradors X 2003 *Physica C* **384** 125

[138] Diko P, Zmorayova K, Hari Babu N and Cardwell D A 2003 *Physica C* **398** 1

[139] Iida K, Hari Babu N and Cardwell D A 2007 *Supercond. Sci. Technol.* **20** 1065

[140] Hsu S-H, Chen I-G and Wu M-K 2002 *Supercond. Sci. Technol.* **15** 653
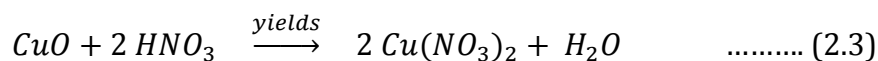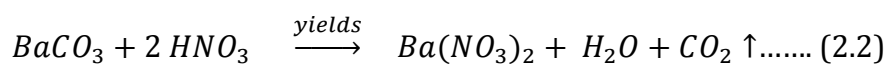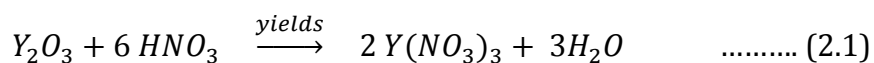
CHAPTER II

EXPERIMENTAL TECHNIQUES

This chapter presents sample preparation techniques used in the present work. It also describes various measurement techniques used.

2.1   Preparation and characterization of precursor powders

2.1.1   Powder Preparation by chemical routes

The $YBa_2Cu_3O_7$ (Y-123) and Y_2BaCuO_5 (Y-211) powders were synthesized following a chemical route employing citrate precursors [1, 2]. Chemical synthesis route is chosen as the homogeneity of the product can be expected to be superior to those produced by solid state routes. An additional advantage is the possibility of producing very fine-sized powders [3, 4].

In order to prepare powders of Y-123 and Y-211, Yttrium oxide (Y_2O_3) of Indian Rae-Earth make, Barium Carbonate ($BaCO_3$) and Copper Oxide (CuO) of E-merck make, each of them of 99.99 % purity were weighed out in stoichiometric ratios and were dissolved in nitric acid (HNO_3) to make corresponding nitrates as indicated below:

$$Y_2O_3 + 6\,HNO_3 \xrightarrow{yields} 2\,Y(NO_3)_3 + 3H_2O \qquad \text{.......... (2.1)}$$

$$BaCO_3 + 2\,HNO_3 \xrightarrow{yields} Ba(NO_3)_2 + H_2O + CO_2 \uparrow \text{....... (2.2)}$$

$$CuO + 2\,HNO_3 \xrightarrow{yields} 2\,Cu(NO_3)_2 + H_2O \qquad \text{.......... (2.3)}$$

Requisite amount of citric acid was added to the nitrate precursor solution along with a small amount of chelating agent Ethylene glycol. The pH of the solution was adjusted to 8 by adding appropriate amounts of ammonia (NH_3). A gel was formed by evaporating the clear solution which was heated to about 250°C. Spontaneous combustion of the gel then generated voluminous material as shown in Fig. 2.1. Each batch of the powders (precursors to Y-123 and Y-211) shown in the figure is ∼ 25 g by weight.
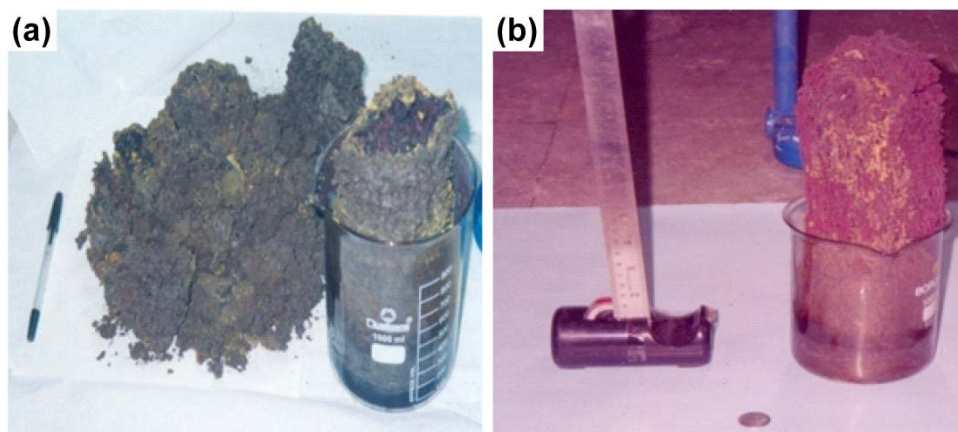
Fig. 2.1. Powders of (a) Y-123 and (b) Y-211 as obtained after combustion process.

Submicron-sized powders thus obtained were heated for 12 hours at 900°C and 950°C to form Y-123 and Y-211 compounds respectively. Formation of the correct phase was confirmed by X-ray diffraction. A photograph of the obtained sintered powders is shown in Fig. 2.2(a). The particle size of the Y-211 thus obtained was observed using a Scanning Electron Microscope (SEM) after dispersing them in ethanol medium. The particles were observed to be in the size range of 400 nm to 1000 nm as shown in Fig. 2.2(b).
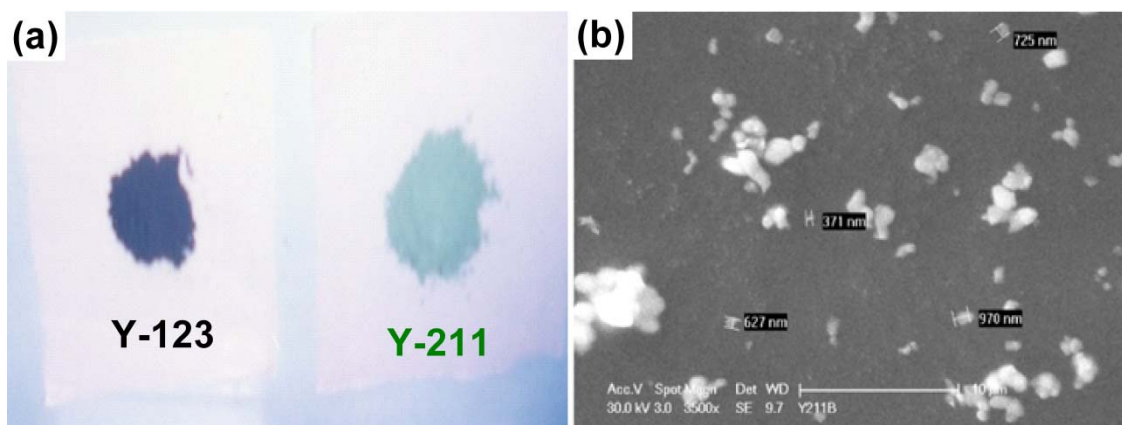
Fig. 2.2. (a) Photograph of the sintered powders of Y-123 and Y-211 is shown. (b)Scanning electron micrograph obtained from sintered Y-211 powder used in the present experiments is shown. The micrograph shows that the Y-211 particles are of size in the range 400 nm – 1000 nm.

2.1.2 Furnaces – Heat treatments

In the present work, two different furnaces were employed, one for sintering the precursor powders of Y-123 and Y-211, and also for the Infiltration Growth (IG) process. The second was used for oxygenating the IG processed samples. Both the furnaces were home-made and had tubular muffles made of re-crystallized alumina (Al_2O_3). Kanthal APM wires were used as heating elements. Chromel–Alumel thermocouples were used for temperature measurement. Eurotherm-make temperature controller (model 2404) and thyristor (model TE10A) were used for controlling the temperature in the furnaces to an accuracy of ± 2°C. In the case of oxygenation furnace, a long quartz muffle of length ∼ 100 cm was introduced into the alumina muffle. The quartz muffle of the furnace after loading with the samples was sealed with rubber cork and plaster of Paris clothe and sealed with Teflon tapes. A schematic picture of the furnace along with the temperature controller and thyristor are shown in Fig. 2.3.
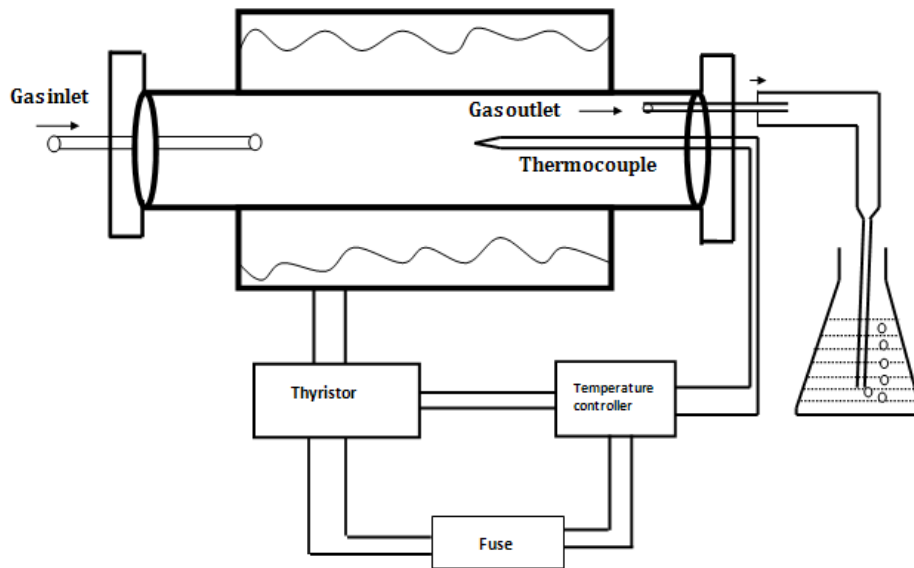
Fig. 2.3. A schematic diagram of the furnace used.

The heat profiles obtained by measuring the temperature as a function of depth in the muffles of the furnaces are shown in Figs. 2.4(a) and (b).
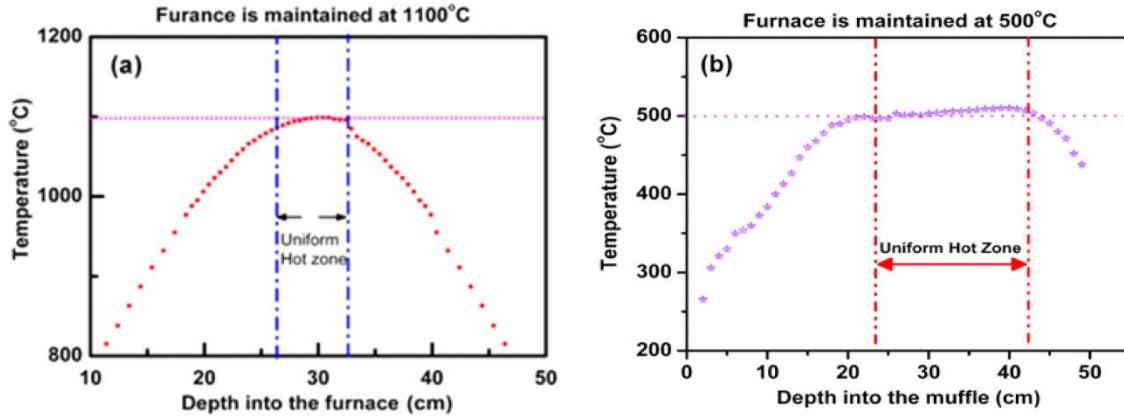
Fig. 2.4. The heat profiles showing the temperature distribution obtained along the length of the muffle in tubular furnaces used for (a) sintering / IGP and (b) oxygenation.

2.1.3 X-ray Diffraction study – Determination of structure

Principle of Operation:

When a beam of parallel mono-chromatic beam of x-rays of approximately 0.1 nm wavelength strikes a crystal, the crystal acts as a three-dimensional diffraction grating and produces an X-ray diffraction pattern. This diffraction comprises of a three dimensional array of reflections which satisfy the condition of Bragg's law:

$$2d\ sin\theta = n\lambda \ .... (2.6)$$

Where 'n' represents the order of diffraction, λ represents the wave-length of the X-rays, 'd' is the distance between a set of parallel lattice planes and θ is the angle between the incident X-ray beam and the atomic lattice plane in the crystal.

The reflection angle for a particular set of lattice planes (hkl) is

$$2\theta = 2\sin^{-1}\left(\frac{\lambda}{2d_{hkl}}\right) .... (2.7)$$

Where (hkl) are miller indices defining the orientation of the plane with respect to the crystallographic axes. In general, the powder x-ray diffraction pattern is a set of reflections in which the lattice spacings and relative intensities are unique from each crystalline substance.

38

X-ray diffractograms were recorded on the sintered powders of Y-123 and Y-211 to confirm their phase formation. Copper K_α radiation with wavelength λ of 1.5414 Å was used. X-ray diffractometer of Bruker make was used for this purpose. The patterns obtained for Y-123 and Y-211 along with indexing are shown in Figs. 2.5(a) and (b) respectively.
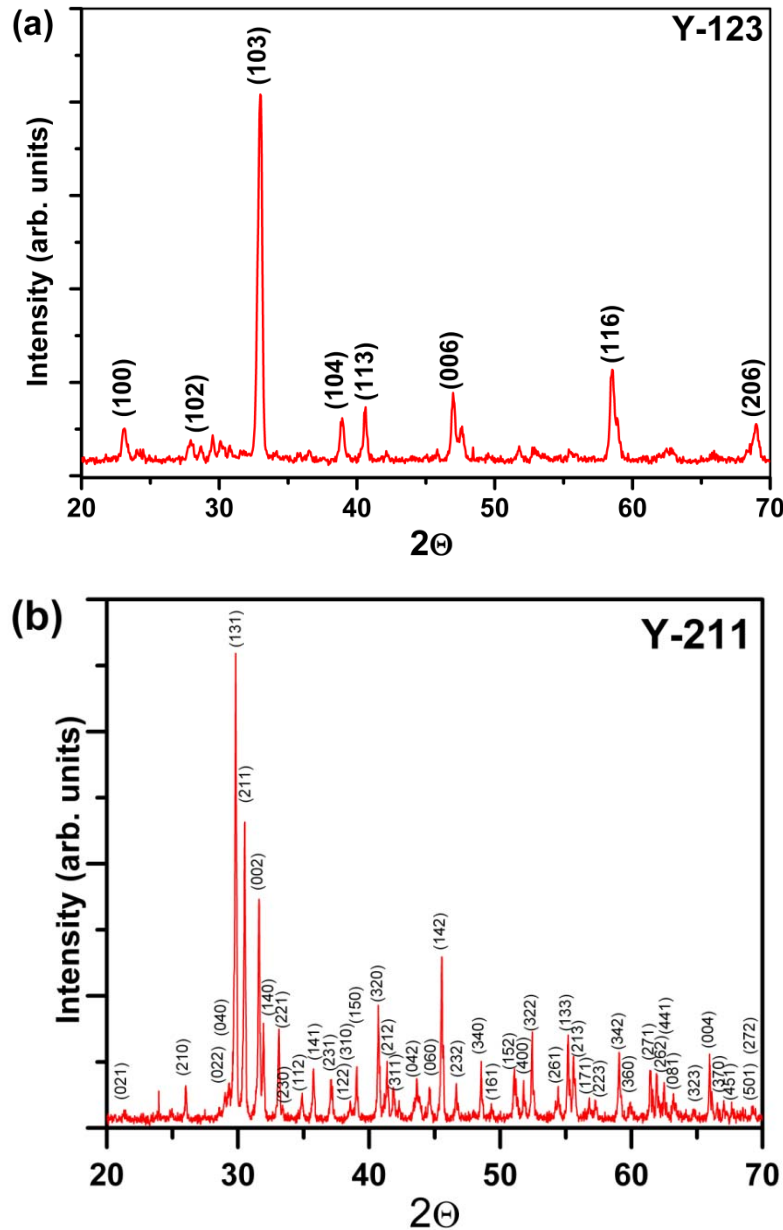
Fig. 2.5. X-ray diffractograms obtained from sintered powders of (a) Y-123 and (b) Y-211

Y-123, as sintered has tetragonal structure while Y-211 has orthorhombic structure. The obtained lattice parameters of the unit cells of both Y-123 and Y-211 are provided in table 2.1.

Table 2.1. Details of crystal structure and unit cell dimensions as analyzed from X-ray diffractograms obtained from sintered powders of Y-123 and Y-211

Sample	Structure	a (Å)	b (Å)	c (Å)	Volume of the unit cell (Å)³
Y-123	Tetragonal	3.829	3.829	11.633	170.532
Y-211	Orthorhombic	7.134	12.18	5.66	491.822

2.2 Fabrication of YBCO superconductors by the modified Infiltration and Growth Process

Infiltration Growth (IG) process enables fabrication of REBCO products with near-net shape and overcomes defects like shrinkage, cracks, pores etc. [5, 6]. However, this process suffers from serious problems like inhomogeneities in the distribution of Y-211 particles [7, 8] and hence often results in non-uniform current densities [7-10] across the volume of the samples.

2.2.1 Preform Fabrication

Sintered powders of Y-123 and Y-211 were compacted into pellets of dimensions of 16 mm X 16 mm X ~ 15 mm and 16 mm X 16 mm X ~ 8 mm respectively by applying uni-axial pressure. For this purpose, a hydraulic press was used. The preforms were made at different compaction pressures in the range 300 – 540 MPa. The photographs of the pellets as compacted are shown in Fig. 2.6.
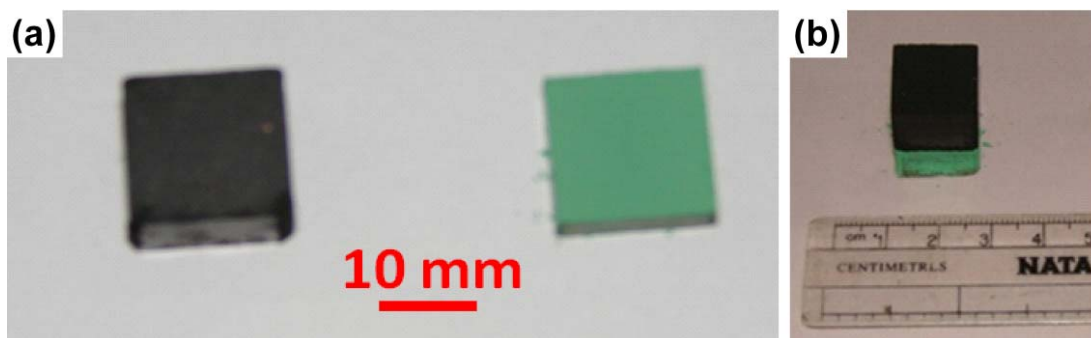
Fig. 2.6. (a) The compacted pellets of Y-123 (black in color) and Y-211 (green in color) made under an applied uniaxial pressure of 460 MPa are shown. (b) Y-123 and Y-211 pellets as arranged for IG process is shown.

2.2.2 Y-Ba-Cu-O superconductors by Preform Optimized IG Process (POIGP)

Bulk YBCO samples are fabricated employing modified Infiltration Growth process. A schematic of the sample assembly employed is shown in Fig. 2.7.

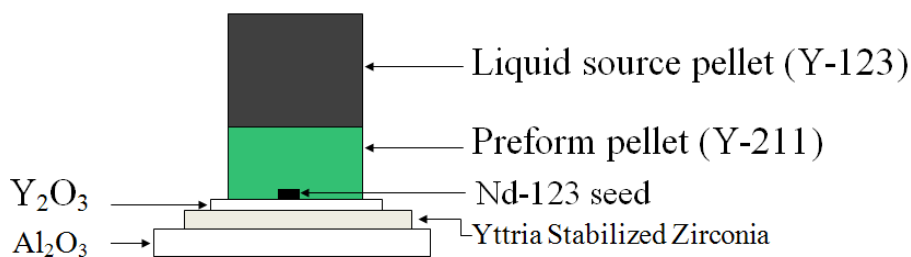**Fig. 2.7.** A schematic of the arrangement of the sample assembly followed for fabrication of YBCO bulk superconductors by modified Infiltration Growth (IG) process is shown. The arrangement typically comprises of pellets of Y-123 and Y-211 arranged one above the other as shown. Nd-123 was used to seed the samples under present study. Layers of Y_2O_3, Ytrria-Stabilized Zirconia (YSZ) and Al_2O_3 were used to minimize the outflow of the liquid phases during heat-treatments.

The Y-211 preform was supported with thin layers of Y_2O_3, Yttria-Stabilized Zirconia (YSZ) and alumina (Al_2O_3) to minimize the outflow of liquid phases during heat treatment. The presence of Y_2O_3 and YSZ layers also help in avoiding contamination of the sample by alumina at elevated temperatures. Y-123 pellet, which is the source of liquid phases, was placed above the Y-211 preform. $NdBa_2Cu_3O_7$ (Nd-123) seeds fabricated following a procedure reported by Hari Babu et al. [11] were used to promote the textured growth of Y-123 during IG process. Y-

41

211 grain-refining compounds like Pt, PtO_2 or CeO_2 were not used in the fabrication of any of the samples under present study.

The samples arranged as described above were heat-treated in a tubular furnace, which has a uniform hot-zone of ~ 60 mm. The temperature of the furnace was controlled and monitored using a temperature controller (model 2404) and thyristor (model TE10A) of Eurotherm make. The sample assembly, as discussed in Fig. 2.7, was heated to 950°C at a rate of 150°C per hour, followed by a 4 hour dwell at that temperature for sintering the preform. (The sintering temperatures and durations were initially optimized with feedback from microstructural and $J_c(H)$ observations. The aim was to provide sufficient strength for the preform to be stable during infiltration and at the same time allow only tolerable levels of grain growth as discussed in the Chapter III). The temperature was then ramped to 1100°C and maintained there for 1 hour to ensure complete infiltration of liquid phases into the Y-211 preform. The samples were then quickly cooled to 1010°C, and then cooled very slowly (at 0.5°C per hour) through the peritectic formation temperature of Y-123 (T_p~1008°C) to 980°C. They were maintained there for 48 hours to ensure complete grain growth of Y-123, and were then furnace-cooled to room temperature. The heat treatment followed is shown in Fig. 2.8.
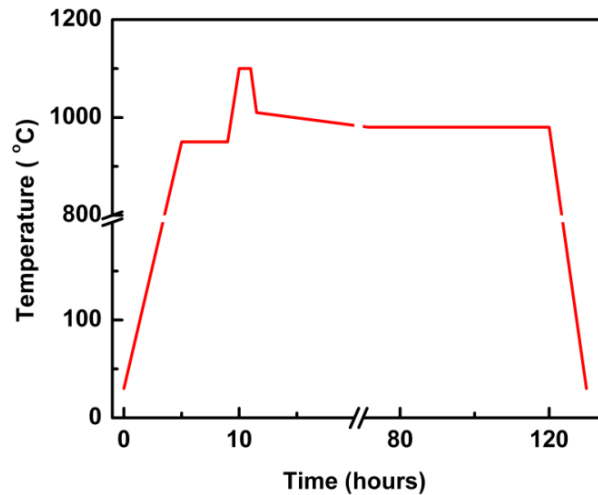
Fig. 2.8. Time – Temperature profile followed for fabrication of YBCO bulk superconductors by modified Infiltration Growth (IG) process termed as Preform Optimized IG process (POIGP).

2.2.3 Oxygenation

The IG processed samples were oxygenated in an atmosphere controlled furnace. The temperature profile recorded showed a uniform hot zone to be of ~ 250 mm (see Fig. 2.5(b)). A quartz tube was introduced in to the alumina muffle of the furnace. A sample holder was fabricated to accommodate five samples at a time for oxygenation. The ends of the quartz muffle, after loading with the samples, were sealed with plaster of Paris clothe to make the furnace leak proof. Inlet and outlet provisions were made to the quartz tube for a controlled flow of oxygen gas in the furnace. The samples were heated in the oxygen atmosphere at 460^0C for about 100 hours. The temperature in the furnace was controlled by a temperature controller and thyristor of WEST make. During the oxygenation process, the Y-123 phase is known to undergo a transformation from the tetragonal state to orthorhombic state.

2.3 Fabrication of YBCO/Ag composites

Addition of Ag is known to modify the microstructures of REBCO superconductors [12-16] and improve their mechanical properties [17, 18]. In order to add Ag to YBCO samples, weighed amounts of metallic Ag was added to the precursor powders of Y-123 and Y-211 as required for various experiments. The added Ag powder was mixed with the Y-123 / Y-211 powders using an ultrasonicator. Ethanol was used as medium for mixing these powders. The resulting powders were ground in an agate mortar and dried before compaction. The resulting powders were filled into steel dies having square cross-sectional area and were made into pellets of by applying a uniaxial pressure of 460 MPa. A hydraulic press was used for applying the pressure.

2.4   Integration of directional solidification with POIGP

The technique of directional solidification has been employed successfully in Melt Growth process [19-22]. In the present work, directional solidification is combined with IG process to fabricate YBCO samples in short time durations.

Furnace for Directional Solidification

A vertical furnace was employed in order to fabricate YBCO samples employing directional solidification. A dc motor was coupled to a pulley stage for lowering the sample assembly at a controlled rate through the hot zone of the furnace. A schematic sketch of the furnace dedicated for directional solidification is shown in Fig. 2.9. The heat profile in the vertical furnace is shown in Fig. 2.10.
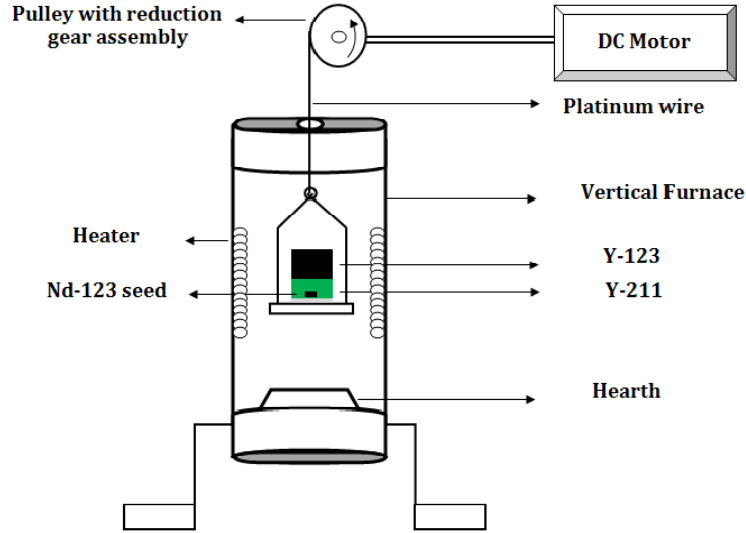
Fig. 2.9. A schematic representation of the vertical furnace dedicated for fabrication of YBCO samples by directional solidification is shown.
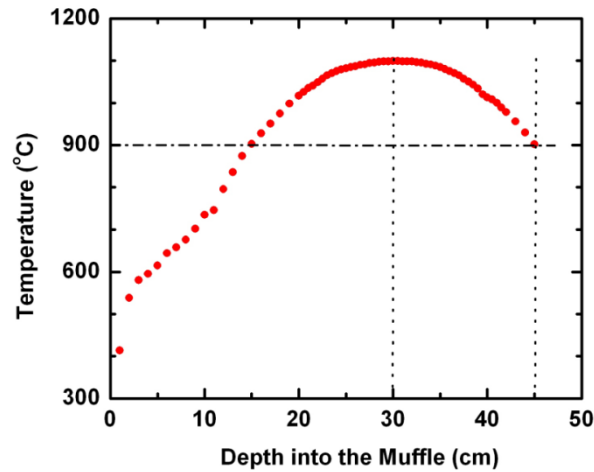
Fig. 2.10. Heat profile of the vertical tubular furnace employed for fabricating YBCO samples is shown. The dotted vertical lines shown in the figure represent the region in which the sample was lowered. The sample was lowered up to a depth in the furnace where the temperature was ∼ 900ºC.

44

2.5 Electrical characterization

2.5.1 Four probe electrical resistivity measurement

The temperature dependence of dc electrical resistivity (ρ) was obtained by employing four probe technique to determine the critical temperature ($T_c$) and transition widths of the samples under study. A sample holder assembly was fabricated to measure electrical resistance as a function of temperature. A programmable constant current source (model 224, Keithley make) was used to send a constant dc current through the sample and a nano-voltmeter (model 181, Keithley make) was used to measure the voltage drop across the sample. Temperature of the sample was measured by placing a Platinum sensor (PT-100) in the close vicinity of the sample. The temperature of the sample was measured and controlled using a cryogenic temperature controller (model DRC-93C, Lakeshore make) with heater attachment. The temperature controller can measure temperature with an accuracy of 10 mK.

A schematic sketch showing the connections made is presented in Fig. 2.11. Typical sample puck and sample holders made for this purpose are shown in Fig. 2.12. The connections made to the sample can also be seen in the figure.
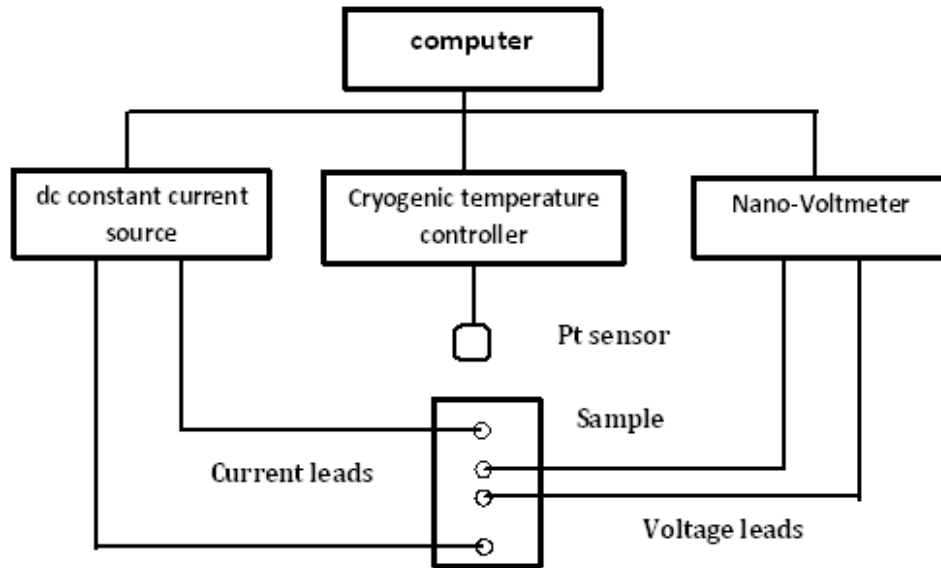
Fig. 2.11. Block diagram for measuring dc electrical resistivity.
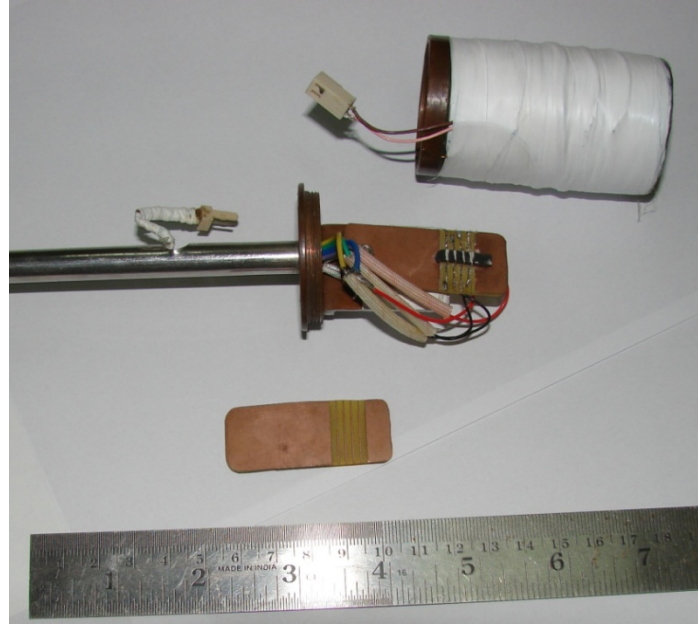
Fig. 2.12. The sample holder fabricated for measuring electrical resistance of superconductors is shown. The sample puck and the heater cavity made can also be seen in the figure.

In order to avoid thermal effect contributions, current at every temperature was reversed during the measurement for thermo-emf corrections.

$$\text{Resistance (R)} = \frac{V^+ - V^-}{I^+ - I^-} = \frac{V^+ - V^-}{2I} \quad \text{.......... (2.8)}$$

Where

V⁺: voltage obtained when positive current (I^+) is sent through the sample

V⁻: voltage obtained when negative current (I^-) is sent through the sample

I : current flowing in the sample

The thermo-emf corrections are made by reversing the current flow through the sample and by measuring the voltage drop across the leads. The difference of V⁺ and V⁻ gives the information on the resistance of the sample.

$$V^+ = V_S + V_{Th} \quad \text{.......... (2.9)}$$

$$V^- = - V_S + V_{Th} \ldots\ldots (2.10)$$

$$V^+ - V^- = V_S + V_{Th} - (-V_S + V_{Th}) = 2\ V_S \ldots\ldots (2.11)$$

$$\therefore\ R = \frac{V^+ - V^-}{2I} = \frac{V_S}{I} \ldots\ldots (2.12)$$

where V_S is the voltage drop across the sample and V_{Th} is the thermo-emf voltage due to heating effects in the sample due to passage of current.

2.6   Magnetic characterization

2.6.1   ac susceptibility measurements

A block diagram for measuring susceptibility as a function of temperature of a sample is shown in Fig. 2.13.
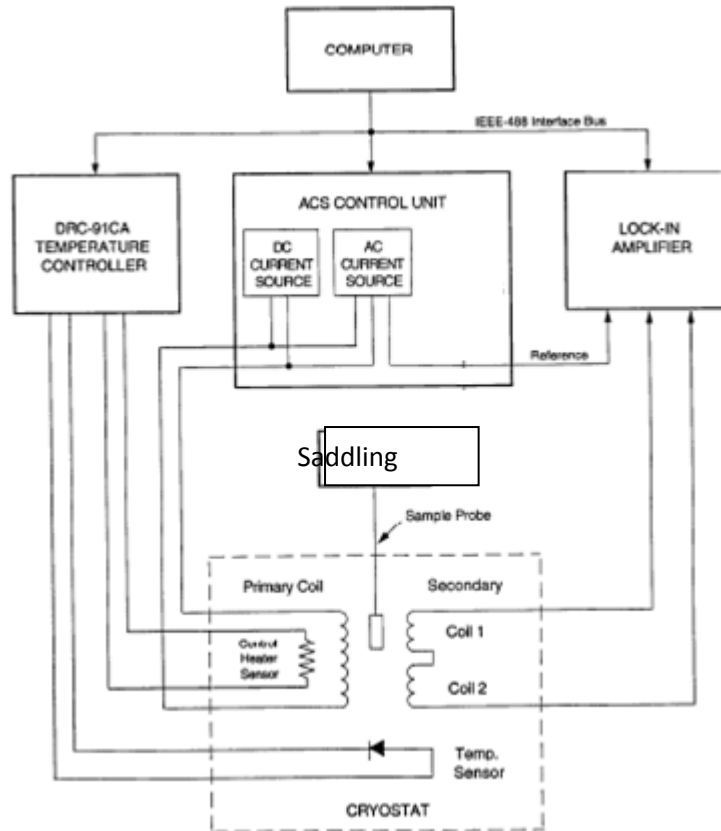
Fig. 2.13. Block diagram for ac susceptibility measurement.

In the ac magnetic measurements, a small ac drive magnetic field is applied causing a time-dependent moment in the sample. The field of the time-dependent moment induces a current in the pickup coils, allowing measurement without the sample motion. The detection circuitry is configured to detect only in a narrow frequency band, normally at the fundamental frequency (that of the ac drive field).

If the applied ac voltage is $H = H_o \cos \omega t$, where ω is the angular frequency $(=2\pi f)$, the resulting magnetization amounts to

$$M = H_o(\chi' \cos\omega t + \chi'' \sin\omega t) \text{ .... (2.13)}$$

where χ' and χ'' represent the real and imaginary components of the fundamental ac susceptibility.

The fundamental principle on which this measurement works is based on the mutual induction (Faraday's law)

$$\nabla \: X \: E = -\frac{\partial B}{\partial t} \text{ .... (2.14)}$$

Basically the assembly comprises of a mutual inductance coil assembly with two secondary coils co-axially mounted in a primary solenoid. The two secondary coils are identical and are connected in opposition in order to cancel the voltages induced by the ac field itself. A constant current source is employed to drive an ac current in the primary solenoid. The field produced by a current with r.m.s. value 'I_{rms}' in a solenoid is given by

$$H_{rms} = \frac{4\pi N_p I_{rms}}{10 \: L_p} \text{ .... (2.15)}$$

where N_p is the number of turns in the primary coil, L_p is the length of the primary coil (in cm) and I_{rms} is the root mean square (rms) value of the ac current through the primary coil. The field amplitude H_{ac} in Oe is $\sqrt{2} \: H_{rms}$

If the secondary coils are ideally made i.e. both the coils are made under similar conditions (number of turns, diameter, etc.), no voltage will be detected by the lock-in amplifier when the coil assembly is empty. But, in practice, the net output from the secondary coils is often non-zero and is temperature dependent. This is eliminated by measuring and subtracting the back ground voltage from the signal measured after introducing the sample in similar conditions. Additionally, there is a need to correct the extraneous phase shifts arising from various sources in the setup. This is done by shifting the phase of the references so as to obtain $\chi'' = 0$ well above T_c as well as well below T_c.

When the induced voltages in the secondaries in sensed at the input of the dual phase lock-in amplifier, it gives out a signal in the form of dc voltages ϵ_r and ϵ_i proportional to the real and imaginary parts of M that are in in-phase and out-of phase, respectively, with respect to the reference signal which is in-phase with the applied field H.

From the measured ϵ_r and ϵ_i, the real and imaginary components of the ac susceptibility χ' and χ'' are determined using the formulae

$$\chi_r = \frac{\epsilon_r}{\alpha\omega AN\mu_o H_m(1-D)} \dots\dots (2.16)$$

$$\chi_i = \frac{\epsilon_i}{\alpha\omega AN\mu_o H_m(1-D)} \dots\dots (2.17)$$

Here N is the number of turns in the secondary across the sample, H_m is the amplitude of the applied ac field, A is the cross-section of the sample, D is the demagnetization factor and α is the filling factor [23]. The absolute values of the ac susceptibility for non-zero demagnetization D values are calculated using the expressions given by Murphy et al. [24].

$$\chi' = \frac{\chi_r - D(\chi_r^2 + \chi_i^2)}{(1 - \chi_r D)^2 + D^2 \chi_i^2} \quad\text{..........(2.18)}$$

$$\chi'' = \frac{\chi_i}{(1 - \chi_r D)^2 + D^2 \chi_i^2} \quad\text{..........(2.19)}$$

Following this procedure, the temperature variations of χ' and χ'' are obtained from the measured temperature dependence of ϵ_r and ϵ_i.

2.6.2 M-H hysteresis loops and critical current density measurements

(A) Bean's model

The critical current density J_c in type-II superconductors can be estimated by analyzing the magnetization using critical state model proposed by C.P. Bean [25]. The model assumes that the penetrated super-currents flow with a density equal to the J_c independent of the local internal field and the flux vortex array is stable and there is no flux creep and the lower critical field is zero. If this magnitude of the current flows everywhere in the specimen, it is in the critical state.

The process of magnetization of a slab of thickness $2a$ in a field parallel to its surface is shown in Fig. 2.14, when the current density is independent of the external field.
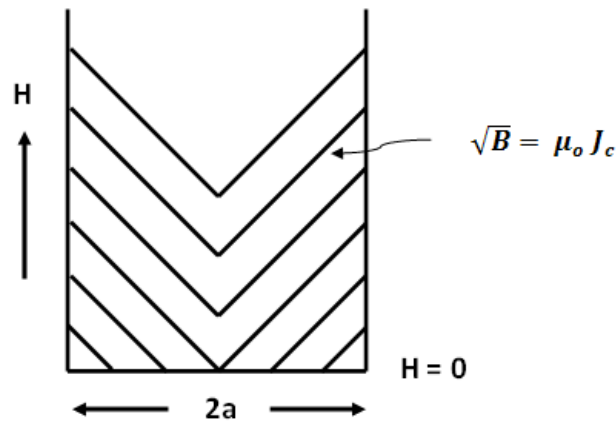
Fig. 2.14. Magnetization process of thin slab of thickness 2a in a field parallel to the surface.

The field within the specimen decreases linearly with the distance, if the material is in the critical state. The Maxwell's equation is

$$\sqrt{B} = \mu_o J_c \ \text{..........} \ (2.20)$$

where J_c is the critical current density in A m^{-2}, B is the magnetic induction in Tesla and μ_o is the absolute permeability

The local internal field H_i is given as

$$H_i = \frac{B}{\mu_o} \ \text{..........} \ (2.21)$$

where B is the macroscopic local flux density.

The local magnetization M_i becomes $M_i = H_i - H$, where H is the applied field. Therefore the total magnetization M is the average of M_i, over the sample cross-section.

If we consider the magnetization for two stages namely

(i) $0 < H < H^*$ and   (ii) $H^* < H$

where H^* is the applied magnetic field at which the internal field reaches the centre of the specimen.

For an infinite slab, the initial magnetization curve $M(H)$ becomes

$$M(H) = -H + \frac{H^2}{2J_c a}, \text{ for } 0 < H < H^* \ \text{..........} \ (2.22)$$

$$M(H) = -\frac{J_c a}{2}, \text{ for } H^* < H \ \text{..........} \ (2.23)$$

The reverse curve for the high $-H_m$ ($H^* < H_m$) case is given by

$$M(H) = -\frac{J_c a}{2} + H_m - H - \frac{(H_m - H)^2}{4J_c a}, \text{ for } H_m - 2H^* < H < H_m \ \text{....} \ (2.24)$$

$$M(H) = \frac{J_c a}{2}, \text{ for } -H_m - H < H_m - 2H^* \ \text{..........} \ (2.25)$$

Where H is the applied magnetic field, H_m is the maximum applied field and $2a$ is the thickness of the slab.

When $H_m > 2H^*$, J_c is related to the magnetization M for slab of thickness $2a$ as

$$M(H^+) - M(H^-) = J_c\, a \quad \cdots\cdots\cdots (2.26)$$

Therefore J_c can be determined by measuring the width of an M-H hysteresis loop at a given field.

(B) Relation of J_c to the magnetization in orthorhombic samples

The discussion made above is applicable only if the sample is considered as an infinite slab. The formulation for the samples in orthorhombic geometry is discussed below:
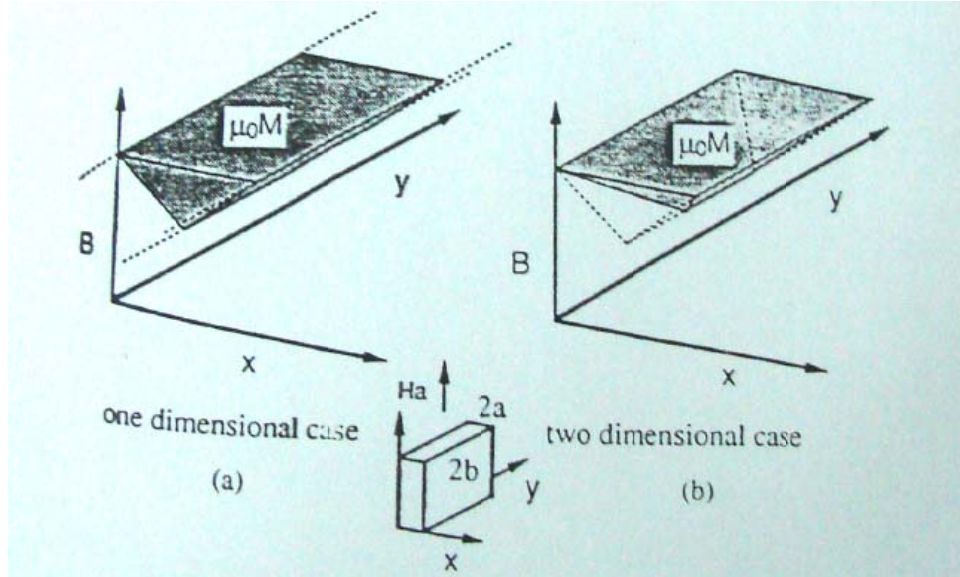
Fig. 2.15. Schematic illustration of the field penetration for (a) one dimensional case and (b) orthorhombic geometry.

Fig. 2.15 shows a schematic illustration of the field penetration for one-dimensional orthorhombic case. When J_c along each side of the cross-section of the sample is same as the initial M(H) curve is given by

$$M(H) = -H + \frac{H^2}{2J_c}\left(\frac{1}{a} + \frac{1}{b}\right) - H^3(3J_c\, 2ab), \text{ for } 0 < H < H^* \quad \cdots\cdots (2.27)$$

$$M(H) = -J_c a \left(\frac{1}{2} - \frac{a}{6b}\right), \text{for } H^* < H \text{ .... (2.28)}$$

And the reverse curve is given by

$$M(H) = -J_c a \left(\frac{1}{2} - \frac{a}{6b}\right) + H_m - H - \left[\frac{(H_m-H)^2}{4J_c}\right]\left(\frac{1}{a} + \frac{1}{b}\right) + \frac{(H_m-H)^3}{12J_c 2ab}, \text{for} \quad H_m - 2H^* <$$
$$H < H_m$$

$$\text{.......... (2.29)}$$

$$M(H) = -J_c a \left(\frac{1}{2} - \frac{a}{6b}\right), \text{for } -H_m < H < H_m - 2H^* \text{ .... (2.30)}$$

Where a and b are dimensions of the cross section of a sample with $a \geq b$

Therefore for the orthorhombic geometry, when H_m is larger than $2H^*$,

$$M(H)^+ - M(H)^- = J_c b \left(1 - \frac{b}{3a}\right) \text{.......... (2.31)}$$

(C) Calculation of J_c from M-H loops

Magnetization hysteresis loops representing magnetization (M) as a function of applied magnetic field (H) were recorded on the samples at various cryogenic temperatures using a Physical Property Measurement System (PPMS) of Quantum design make. The specimens used for the measurements were of size approximately 2 mm x 2 mm x 5 mm, which were cut such that their long dimension was normal to the pressed surface of the samples. The samples were exposed to magnetic fields in the range 9 - 13 Tesla generated by superconducting magnet in order to record the field dependences of magnetization. A typical M-H loop obtained for a superconductor is shown in Fig. 2.16.
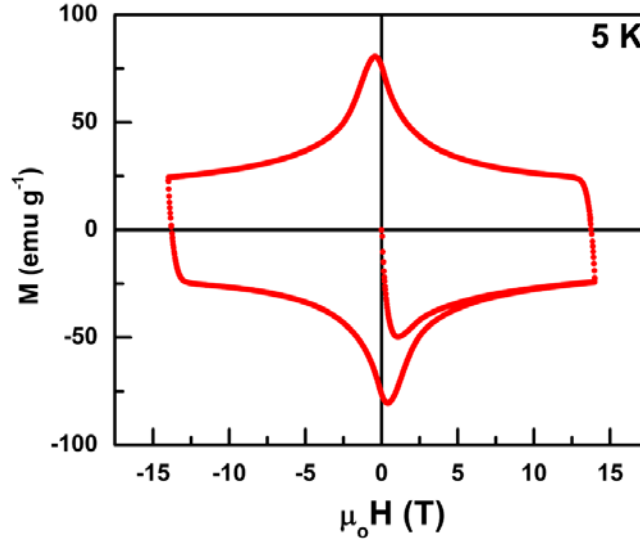
Fig. 2.16. A typical magnetic hysteresis (M-H) loop obtained from a IG processed YBCO superconductor at 5 K.

The critical current densities (J_c) of the samples were determined following extended Bean's Critical State model [25 -27] as described below:

$$J_c = \frac{20\,\Delta M}{d} \dotsb \textbf{(2.32)}$$

where $\Delta M = M^+ - M^-$ (in emu/cc), $d = b\left(1 - \dfrac{b}{3a}\right)$; $a > b$ and a, b are broad and narrow dimensions of the sample (in cm).

2.7 Microstructural characterization

Different microscopy techniques like Optical Microscopy, Scanning Electron Microscopy (SEM), SEM with Electron Back Scattered Diffraction (EBSD) attachment and Transmission Electron Microscopy (TEM) techniques were used.

In order to prepare samples for microstructural characterization, the samples were sliced in to thin sections using a low speed saw (model Isomet 1000, Buehler make). The sliced samples were mounted in bakelite and were polished using an auto polisher (Buehler make). High temperature bulk YBCO superconductors because of their ceramic and brittle nature are quite difficult to prepare for microstructural studies.

The specimen preparation technique adopted in the present study is as follows: The sections extracted from the samples were mounted using a hot setting bakelite compound to a size 1" (2.54 cm) dia and 1.5 - 2 cm height. The mounted pieces were initially ground on a SiC paper (600, 800, 1000 and 1200 grits) to a flat surface and was further polished on a polishing cloth using a rotating wheel of the Buehler make polishing machine, using different grades (6, 3, 1, 0.25 μm) of diamond paste as grinding media. The surface was cleaned after every stage of polishing. Kerosene was used as the lubricant during polishing as these materials are highly reactive with water. Polishing time at each stage ranged from 2 to 30 minutes with SiC paper and 0.5-2 hours with diamond paste depending on the nature of heat treatment given to the sample. The polished surface of the sample was then finally cleaned with methanol and dried in a hot air. In the present study, no etching was done to the polished surface of the samples. The micrographs thus obtained were characterized for various microstructural parameters using quantitative metallographic methods as explained below.

2.7.1 Optical Microscopy

The microstructure of a solid is defined by a variety of features like grains, inclusions, grain boundaries, platelets, defects like pores, voids, macro cracks, platelet cracks, twins, stacking faults etc. The polished surface of the sample when observed under an optical microscope reveals large amount of microstructural information. Features like grains, pores, phase distribution, cracks, twins, platelets etc. up to a magnification of 1000 X can be obtained. Since an optical microscope uses the visible or near visible portion of the electromagnetic spectrum, the resolution is limited to 0.2 μm (with white light). Hence the features of order less than 0.3 μm cannot be viewed employing optical microscope. Basically the information on morphology, color, opacity and optical properties are studied under an optical microscope, and this helps characterizing the material.

Optical metallography technique depends on the variations in the contrast of the features, due to the inherent difference in the absorption characteristics of the phases present in the polished surface of the sample. In general, the phases in REBCO systems show poor contrast when examined by incident light since the densities of the phases are quite close to each other. Hence in order to enhance the surface contrast, a polarized light is employed. By introducing a polarizer in to the condenser lens system, the different phases in the polished surface can now easily be identified since the incident light is plane polarized, thus giving a direct measurement of the phase change at the reflecting surface. Another advantage in using the polarized light is the ease in recognizing the surface anisotropy. This is possible since different planes of a grain have different reflectivities. Since the depth of the imaging in the light microscopy is practically nil, the specimens with highly polished surfaces with very high levels of reflectivity are required. For samples having no substantial change in the anisotropy, the volume fraction (V_f) is same as the area fraction (A_f) i.e. $V_f = A_f$

2.7.2 Field Emission Scanning Electron Microscopy

The Scanning Electron Microscope (SEM) employs a high-energy (in keV) electron beam and helps in imaging the topography of the sample surface by operating in a raster scan mode. In the case of a Field Emission Scanning Electron Microscope (FE-SEM), a field-emission cathode in the electron gun of a SEM provides narrower probing beams at low as well as high electron energy, resulting in both improved spatial resolution and minimized sample charging and damage. The electrons when interact with the atoms of the sample produce secondary electrons, back-scattered electrons, transmitted electrons, characteristic X-rays etc. Separate detectors are present to pick up the information about each of these resultants. A typical schematic sketch representing the above mentioned process is shown in Fig. 2.17.

The secondary electron imaging can produce very high-resolution images of a sample surface, revealing details even in the size range 10 - 100 nm. Due to the very narrow electron beam, SEM micrographs have a large depth of field yielding a characteristic three-dimensional appearance useful for understanding the surface structure of a sample. Back-scattered electrons (BSE) are beam electrons that are reflected from the sample by elastic scattering. BSE are often used along with the spectra made from the characteristic X-rays. Since the intensity of the BSE signal is strongly related to the atomic number (Z) of the specimen, BSE images can provide information about the distribution of different elements in the sample. It also provides information about different phases present in the sample based on the variation in reflectivity content.
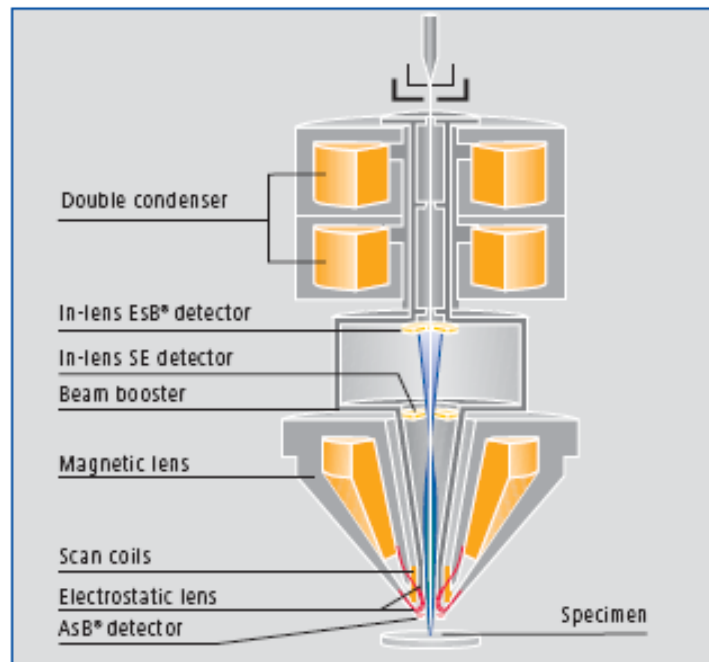
Fig. 2.17. A schematic picture showing emission of electron beam in a Scanning Electron Microscope (SEM).

Electron beam of very high energies are employed in order to visualize the sub-surface structures while low energy BSE detection is quite useful for high resolution investigation of critical / charging specimens. This is met through a new In-lens BSE detection system. In order to reduce aberrations and sensitivity to

interfering stray-fields the electron optical column is equipped with a positively biased booster that shifts the energy of the primary electrons. The incident beam is focused by a combination of a magnetic lens with an axial gap that avoids field leakage to the specimen and an electrostatic retarding together with the grounded pole piece cap. Shortly before the electrons hit the specimen they are decelerated down to the desired primary energy. A suitable explanation for the reduction of spherical and chromatic aberrations is that the electron beam is focused by the objective lens at higher energies and smaller electron beam diameters. Another advantageous effect of this arrangement is the collection of secondary electrons emerging from the sample surface attracted and accelerated by the positively biased electrode of the beam booster and finally projected onto the In-lens detector.

Characteristic X-rays are emitted when the electron beam removes an inner shell electron from the sample, causing a higher energy electron to fill the shell and release energy. These characteristic X-rays are used to identify the composition and measure the abundance of elements in the sample.

In the Present work, a Field Emission Scanning Electron Microscope (model Ultra 55, Carl Zeiss make) was employed for obtaining the micrographs. The working distance for most of the cases was in the range 4 - 10 mm. The charging effects of the electron beam on the sample were bypassed by either gold coatings or by creating a silver paint / strip channel from the holder to the sample. FE-SEM with Energy Dispersive Spectrometry (EDS) and Wavelength Dispersive Spectrometry (WDS) attachments was employed in the present study. WDS can detect the presence of elements to a greater accuracy compared to EDS. A typical sketch of WDS is shown in Fig. 2.18.

Fig. 2.18. A photograph of the Wavelength Dispersive Spectrometer used with Field Emission Scanning Electron Microscope (FE-SEM).

2.7.3 Electron Back Scattered Diffraction

Electron Back Scattered Diffraction (EBSD) studies were carried out using a Hitachi-make scanning electron microscope (model S-4300 SE/N) equipped with a hot Schottky filament; the EBSD unit attached to the microscope was supplied by EDAX-TSL. A typical schematic sketch representing the principle of operation is shown in Fig. 2.19.
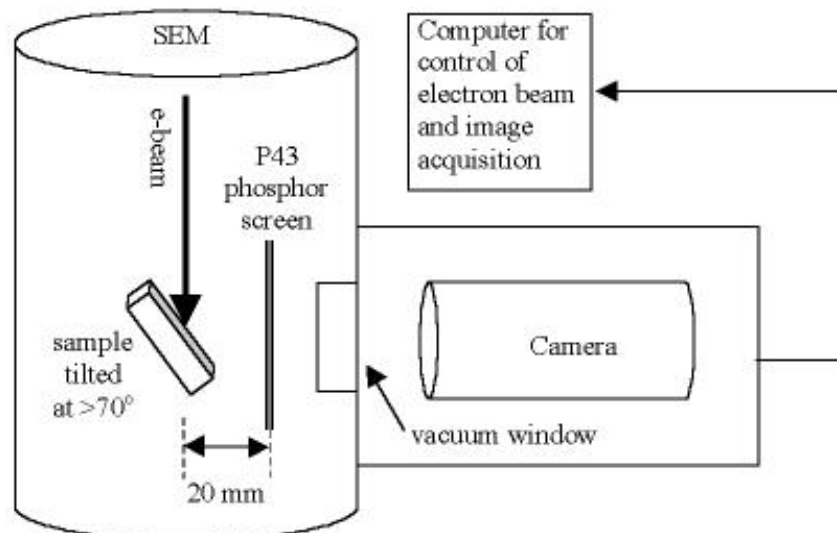

Fig. 2.19. A schematic picture representing the principle of working of Electron Back Scattered Diffraction (EBSD).

For the investigations, the specimens which were polished down to 0.25 μm as described in Chapter 2.7 were further polished using colloidal silica (particle size 50 nm) for approximately 20 minutes. To generate crystal orientation maps, the electron beam was scanned over different areas and the resulting EBSD patterns were indexed and analyzed. A step size of 50 nm was used in the data scans. Data cleanup was carried out using standard procedures in the EDAX-TSL software. Grain Confidence Index (CI) standardization was first carried out, followed by neighbour confidence correlation with CI of 0.1. Further, a partition was created to choose only those data points with CI $\geq$ 0.1. This ensures that only data points with a high quality are used in the analysis. Color-coded pictures were generated which map the crystallographic orientations in the matrix.

2.7.4 Transmission Electron Microscopy

The Transmission Electron Microscope (TEM) is used to characterize the microstructure of materials with very high spatial resolution. Information about the morphology, crystal structure and defects, crystal phases and composition and magnetic microstructure can be obtained by a combination of electron-optical imaging (2.5 Å point resolution in the Tecnai), electron diffraction, and small probe capabilities. The trade-off for this diverse range of structural information and high resolution is the challenge of producing very thin samples for electron transmission. The schematic representation of a TEM is shown in Fig. 2.20
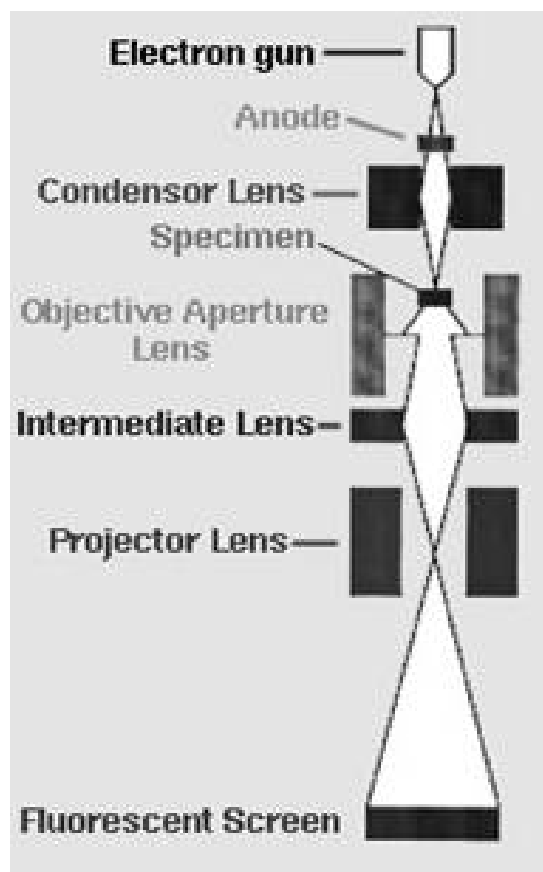
Fig. 2.20. Schematic representation of the emission of electron beam in a Transmission Electron Microscope.

The defect structure on a very fine scale in the optimized POIGP sample was studied using a TEM. A thin section of the sample was sliced using a low speed saw and was dimple ground followed by ion milling in argon atmosphere. The usual method of picking up thin samples from the ion-beam milled specimens was not possible due to the brittle nature of the samples. An FEI-Quanta 3D dual beam system with an Omni Probe was used for the sample preparation. A focused ion beam was employed to extract a thin layer from the milled sample for observation under TEM. The procedure by which the electron transparent specimens are made is shown in Fig. 2.21.
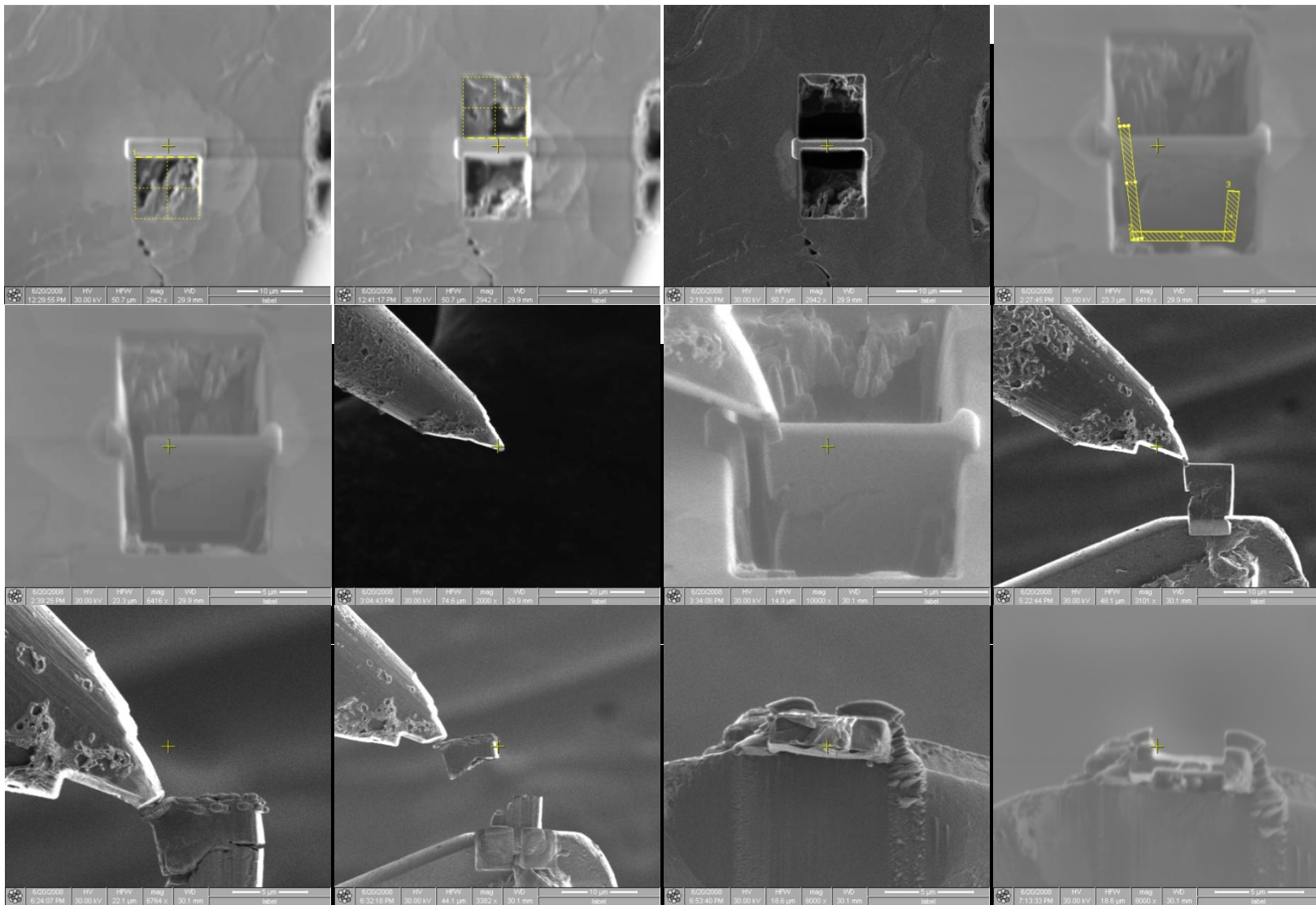
Fig. 2.21. Images obtained at different stages of making YBCO ceramic sample for observation under TEM

References

[1]   Manthiram A and Good enough J B 1987 *Nature* **329** 908

[2]   Bahadur D, Banerjee A, Das A, Gupta K P, Mathews T, Mitra A, Tewari M and Majumdar A K 1988 *Rev. Solid State Science* **2** 77

        Shieh S H and Thomson W J 1992 *Physica C* **204** 135

[3]   Kordas G, Wu K, Brahme U S, Friedmann T A and Ginsberg D M 1987 *Mater. Lett.* **5** 417

[4]   Pathak L C and Mishra S K 2005 *Supercond. Sci. Technol.* **18** R67

[5]   Sudhakar Reddy E and Rajasekharan T 1998 *Supercond. Sci. Technol* **11** 523

[6]   Cloots R, Koutzarova T, Mathieu J-P and Ausloos M 2005 *Supercond. Sci. Technol.* **18** R9

[7]   Jiao Y L, Xiao L, Ren H T, Zheng M H and Chen Y X 2003 *Physica C* **386** 266

[8]   Chow J C L, Leung H T, Lo Wai and Cardwell D A 1998 *J. Mater. Sci.* **33** 1083

[9]   Iida K, Hari Babu N, Shi Y and Cardwell D A 2005 *Supercond. Sci. Technol*. **18** 1421

[10]   Chen S-Y, Hsiao Y-S, Chen C-L, Yan D-C, Chen I-G and Wu M-K 2008 *Mater. Sci. Eng. B* **151** 31

[11]   Hari Babu N, Shi Y, Iida K and Cardwell D A 2005 *Nature Mater.* **4** 476

[12]   Mendoza E, Puig T, Varesi E, Carrillo A E, Plain J and Obradors X 2000 *Physica C* **334** 7

[13]   Diko P, Krabbes G and Wende C 2001 *Supercond. Sci. Technol.* **14** 486

[14]   Maeda J, Izumi T and Shiohara Y 1999 *Supercond. Sci. Technol.* **12** 232

[15]   Iida K, Hari Babu N and Cardwell D A 2007 *Supercond. Sci. Technol.* **20** 1065

[16] Hari Babu N, Iida K, Briffa A, Shi Y-H, Matthews L S and Cardwell D A 2007 *IEEE Trans. Appl. Supercond.* **17** 2953

[17] Foerster C E, Lima E, Rodrigues Jr P, Serbena F C, Lepienski C M, Cantão M P, Jurelo A R and Obradors X 2008 *Braz. J. Phys.* **38** 341

[18] Fujimoto H 2009 *IEEE Trans. Appl. Supercond.* **19** 2933

[19] Izumi T, Nakamura Y and Shiohara Y 1991 *Adv. Supercond.* **5** 429

[20] Meng R L, Kinalidis C, Sun Y Y, Gao L, Tao Y K, Hor P H and Chu C W 1990 *Nature* **345** 326

[21] Parish M V and Chandler D B 1992 *HTS Materials, Bulk Processing and Bulk Applications* (World Scientific, Singapore)

[22] Selvamanickam V, Partsinevelops C, Mc Guire A V and Salama K 1992 *Appl. Phys. lett.* **60** 3313

[23] Couach M and Khoder A F *Magnetic Susceptibility of Superconductors and other Spin Systems* edited by Hein R A, Francavilla T L and Liebenberg D H 1992 (Plenum, Newyork)

[24] Murphy S D, Renouard K, Crittenden R and Bhagat S M 1989 *Solid State Commun.* **69** 367

[25] Bean C P 1962 *Phys. Rev. Lett.* **8** 250

[26] Chen D X and Goldfarb R B 1989 *J. Appl. Phys.* **66** 2489

[27] Murakami M, Morita M, Doi K and Miyamoto K 1989 *Jpn. J. Appl. Phys.* **28** 1189

CHAPTER III

DEVELOPMENT OF
PREFORM OPTIMISED INFILTRATION AND GROWTH PROCESS (POIGP)

3.1   Introduction

As discussed in Chapter I, the Infiltration Growth (IG) process [1-12] offers several advantages over the conventional Melt Growth (MG) process [13-18] in the fabrication of bulk $REBa_2Cu_3O_{7-\delta}$ (RE-123) (RE = Y, Nd, Sm, Gd, Dy etc.) superconductors supporting high current densities (J_c). Unlike the MG process which creates a variety of flaws in the final product due to large shrinkage and liquid phase outflow [7, 19], the IG process allows near net shape fabrication of complex-shaped products with negligible shrinkage and distortions [2, 3]. Fabrication of hollow cylinders [2], superconducting foams [20] and fabrics [21, 22] using this process has been reported. The importance of a uniform distribution of small-sized spherical inclusions of RE-211 in the RE-123 matrix in order to enhance the critical current density (J_c) and its magnetic field dependence $J_c(H)$ has been recognized [23-25]. One of the major advantages of the IG process relative to the MG process is the ability of the former to provide fine-sized spherical RE-211 precipitates in the RE-123 matrix, even without addition of compounds such as PtO_2 and CeO_2 [8, 10, 12]. The above advantages make the IG process very attractive. There are, however, many reports of inhomogeneities in the microstructure and J_c over the volume of MG [26, 27] and IG [9, 10] processed samples. The wide range in the spatial distribution of Y-211 particles reported in literature in single domain Y-123 has been attributed to pushing effects [28, 29]. A spatial variation of critical temperature (T_c) over the volume of IG processed samples has also been reported [9, 10].

Mahmood et al. [30] have studied the effect of temperature at which the RE-211 preforms are sintered, on the microstructure and J_c of IG processed samples.

They have reported a systematic densification of the RE-211 preforms with increasing sintering temperature which resulted in a decrease of the pore volume in the preform, and an associated increase in J_c after IG processing. Their results show the importance of monitoring and optimizing the preform fabrication process for enhancing the current carrying capacity of IG processed samples.

Iida et al. [10] have reported a comparative study of MG and IG processed samples paying particular attention to the spatial variation of microstructure and the associated J_c. They have observed in their study that Y_2BaCuO_5 (Y-211) content in the IG processed samples varied from 5% to 30%, with the J_c varying from 5 kAcm^{-2} to 30 kAcm^{-2}, from a region away from the seed to a region just below the seed crystal.

Both Mahmood et al. and Iida et al. [30, 10] have reported a considerable amount of residual porosity in the IG processed samples. In the context of applications, though IG process offers advantages of near net shape fabrication without shrinkage and distortions, uncertainties in the uniformity of microstructure and J_c as discussed above is a matter of serious concern.

In the present work, we have addressed the above mentioned problems by optimizing the fabrication of the Y-211 preform. Submicron-sized Y-211 precursor powders prepared by citrate synthesis were used. Y-211 powder samples were fabricated using compaction pressures in the range 300 to 540 MPa in a square die of side 16 mm. A higher compaction pressure was expected to lower overall volume fraction of the pores into which the liquid phases would be infiltrated, an effect like the one obtained by Mahmood et al. [30] by using higher temperatures for sintering. In addition, to avoid the associated grain growth, we limited the sintering temperature of the Y-211 preform to 950°C. The above modifications generated samples with a uniform distribution of fine Y-211 in the Y-123 matrix. The samples thus prepared supported high current densities up to high magnetic fields.

The initial part of the chapter will discuss the wide differences in properties that result from varying the conditions under which the preform is fabricated prior to the infiltration of liquid phases. The efforts made towards optimizing the preform fabrication are then discussed. The effect of preform compaction pressure on the final microstructures and current densities of the IG processed samples thus prepared is then discussed. The optimized samples show a highly uniform microstructure and $J_c(H)$, with high current density retained to high magnetic fields. An attempt is made to understand the improved performance of the samples in terms of the microstructure.

3.1.1   Effect of sintering temperature and durations

In Fig. 3.1, we compare the microstructures of two IG processed samples fabricated using preforms compacted under a uniaxial pressure of 380 MPa: one of them in which the Y-211 preform was not pre-sintered at all before the infiltration of liquid phases, and the other in which the preform was pre-sintered for 4 hours at 950°C.
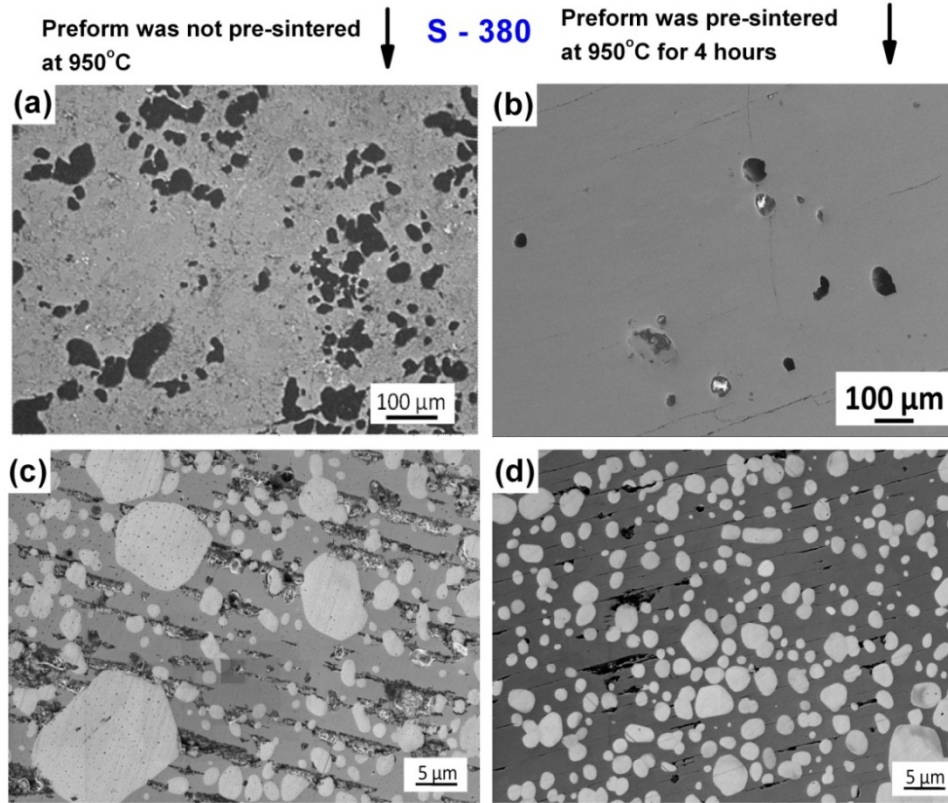
Fig. 3.1. The final microstructures of two IG processed samples fabricated using preforms compacted under a pressure of 380 MPa: one in which the Y-211 preform was not pre-sintered and the other in which the preform was pre-sintered at 950°C for 4 hours are shown. It can be observed when the preform was not sintered before infiltration, considerable porosity resulted in the end product as in (a). On the other hand, the final microstructure of the sample whose preform was sintered at 950°C for 4 hours showed nearly no porosity as in (b). The micrographs provided in (c) and (d) are the images obtained at higher magnifications of the samples mentioned.

The absence of pre-sintering led to considerable porosity in the end product as can be seen in Fig. 3.1(a). The sample pre-sintered for 4 hours at 950°C, on the other hand, showed minimal porosity as seen from Fig. 3.1(b). The reduction in porosity can be attributed to mechanical rigidity of the pre-sintered preform during the infiltration of liquid phases. Fig. 3.1(c) shows presence of larger Y-211 grains when the preform was not pre-sintered while their growth was minimal as shown in Fig. 3.1(d), when the preform was pre-sintered. It can also be seen that pre-sintering has minimized the macro-cracks.

Fig. 3.2 compares the microstructures of two IG processed samples fabricated from Y-211 preforms compacted at 540 MPa, and pre-sintered at 950°C for 24 hours and 4 hours respectively.
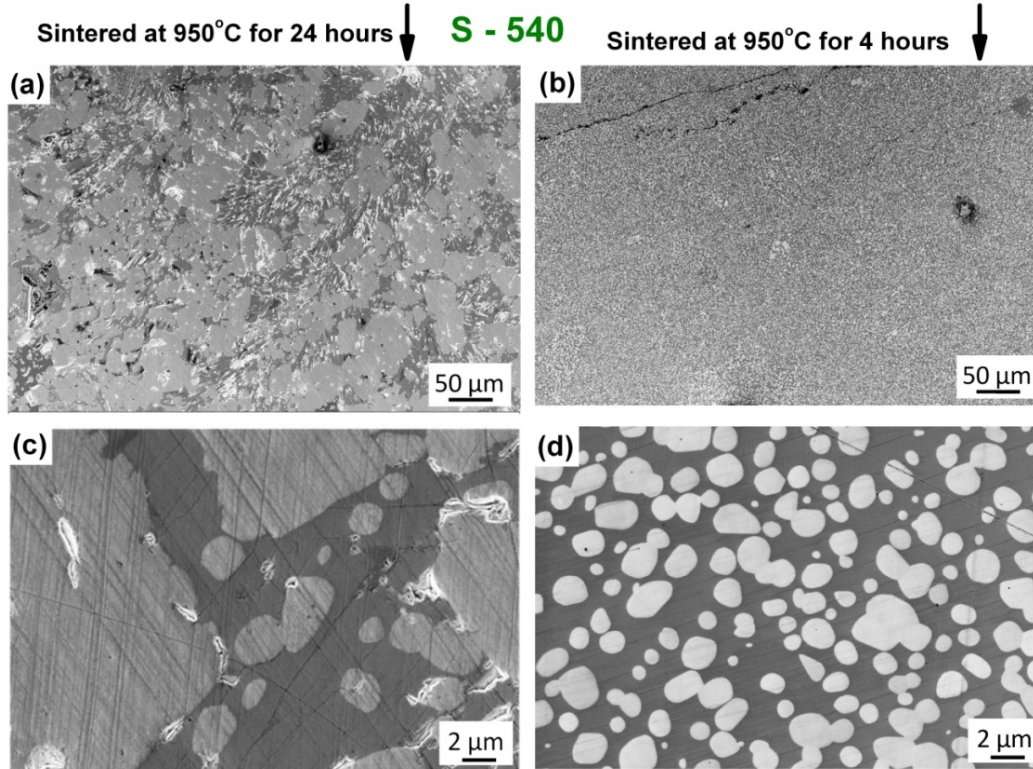

Fig. 3.2. The effects of over-sintering the preforms on the final microstructures are shown. Two samples whose preforms were sintered at 540 MPa were chosen for this study. Both the samples were free from porosity possibly due to the high compaction pressures used. In (a), the final microstructure of a sample is shown whose preform was sintered for 24 hours. It can be seen that there is considerable Y-211 grain growth in this sample. In (b), the microstructure of a sample whose preform was sintered at 950°C for only 4 hours is shown; it shows a uniform distribution of spherical Y-211 particles with fine size and morphology.

There was no porosity in both the samples as seen from Figs. 3.2(a) and (b) possibly due to the high preform compaction pressures used. However, considerable Y-211 grain growth can be seen in Fig. 3.2(c) due to long duration of preform sintering, unlike in Fig. 3.2(d) with preform sintered for 4 hours.

The microstructural study discussed above shows that Y-211 preforms when sintered for 4 hours at 950°C prior to infiltration results in a uniform distribution of

69

fine sized Y-211 particles in the matrix of Y-123. Magnetic field dependence of J_c at 77 K was studied in the above samples, and are shown in Figs. 3.3(a) and (b). It can be seen that the samples when pre-sintered for the optimized duration of 4 hours at 950°C exhibited higher current densities. Following the above observations, further work was carried out using Y-211 preforms sintered for 4 hours at 950°C.
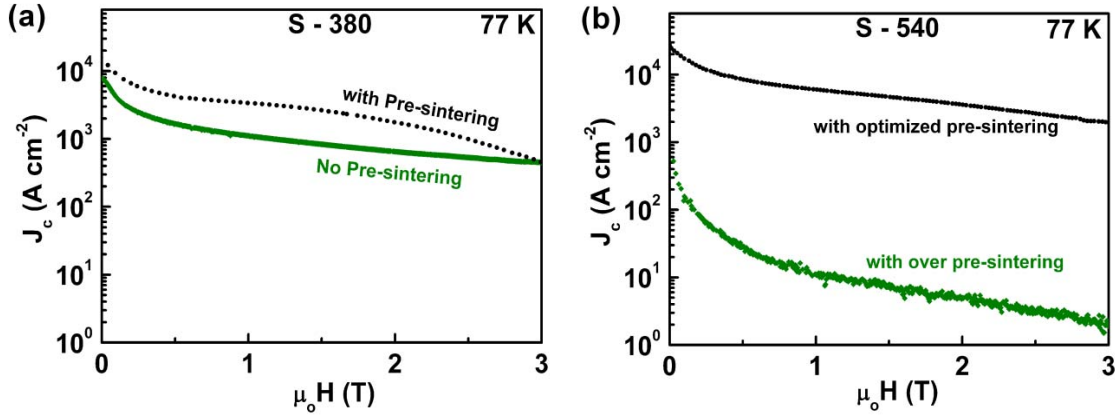
Fig. 3.3. (a) The field dependence of J_c at 77 K of two IG processed samples fabricated using preforms compacted under a pressure of 380 MPa. In one case, the Y-211 preform was not pre-sintered and in the other case, the preform was pre-sintered at 950°C for 4 hours. (b) The J_c(H) at 77 K of two IGP samples fabricated under preform compaction pressure of 540 MPa. The durations for which the preforms were pre-sintered are marked in the figure.

3.2   Preform Optimized Infiltration and Growth Process (POIGP)

3.2.1 Effect of preform compaction pressure

In order to study the effect of compaction pressure on final microstructures and current densities, pellets of Y-211, with 16 mm x 16 mm square cross section and 8-10 mm height, were prepared in a steel die under an applied uniaxial pressure in the range 300 to 540 MPa. Y-123 pellets of 16 mm x 16 mm cross sectional area were used as liquid phase ($BaCuO_2$ and CuO) sources. In each of the experiment, the ratio Y-123 : Y-211 was maintained as 2:1 by weight.

The details of the sample assembly used in the IG process and the heat treatment schedules employed have been discussed in detail in Chapter 2 in Section 2.2.2. $NdBa_2Cu_3O_7$ (Nd-123) seeds were used to promote textured growth of Y-123

as discussed in the chapter. No Y-211 grain-refining compounds like Pt, PtO_2 or CeO_2 were used. The IG processed samples thus obtained were oxygenated in a tubular furnace at 460°C in flowing oxygen for 100 hours. Samples were prepared from preforms compacted at pressures of 300 MPa, 380 MPa, 460 MPa and 560 MPa, and those samples are referred to hereafter as S-300, S-380, S-460 and S-540 respectively.

3.3 Preliminary characterization

Fig. 3.4 shows the photograph the sample S-460 obtained after IG process, as a typical example. Polished specimens from the samples when observed under polarized optical microscope showed uniform illumination showing the single domain nature of the samples.
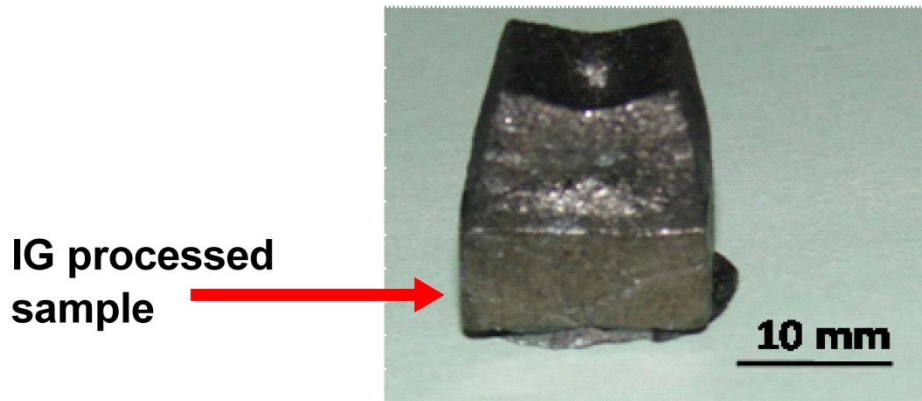
Fig. 3.4. A photograph of the as-made IG processed sample (S-460).

3.3.1 Electrical resistivity and ac susceptibility

For the samples S-300, S-380, S-460 and S-540, the temperature dependences of dc electrical resistivity (ρ) and of in-phase component of ac susceptibility (χ') are shown in Figs. 3.5(a) and (b) respectively. It is evident from the figures that all the samples showed sharp superconducting transitions. The narrow transition widths seen in the temperature dependences of χ' (Fig. 3.5(b)) of all the present samples establish the absence of oxygen-deficient low T_c phases. T_c and ΔT_c values for each of the sample are provided in table 3.1.
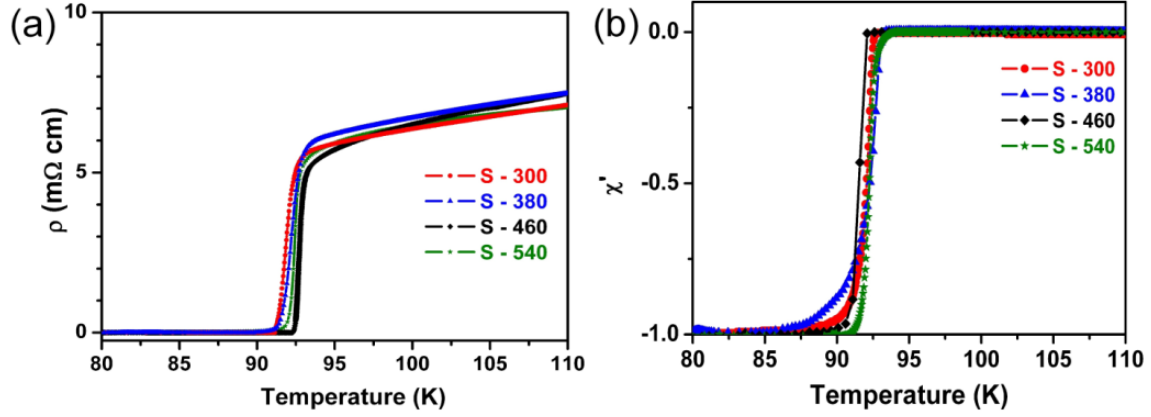
Fig. 3.5. (a) Temperature dependence of electrical resistivity of the samples S-300, S 380, S-460 and S-540 are shown. The high quality of the samples is evident from the sharp superconducting transitions with transition widths (ΔT_c) < 1 K achieved for all the specimens. (b) Variation of the normalized ac susceptibility with temperature in the S-300, S 380, S-460 and S-540 are shown. The sharp superconducting transitions observed, and the absence of secondary peaks, confirm the homogeneity of oxygen content and rule out the presence of oxygen deficient low T_c phases in the samples.

Table 3.1. Comparison of transition temperatures and transition widths of the YBCO samples fabricated by POIGP

Sample	S - 300	S - 380	S - 460	S - 540
Onset of the critical temperature T_c^{onset} (K)				
From resistivity measurements	92.4 K	92.8 K	93 K	92.7 K
From ac susceptibility measurements	92.6 K	93.2 K	92.1 K	93.5 K
Transition width, ΔT_c (K) from ac susceptibility measurements	1.2 K	1.6 K	0.7 K	1.1 K

3.4 Microstructural characterization

Specimens were sectioned from the samples S-300 to S-540 using a low speed saw. The obtained sections were mounted in Bakelite and polished for microstructural studies. The details of sectioning and polishing are discussed in section 2.7 in Chapter II. The polished specimens are observed under Field Emission Scanning Electron Microscope (FE-SEM).

3.4.1 Effect of preform compaction pressure on the final microstructures of Y-Ba-Cu-O samples fabricated by POIGP

FE-SEM images obtained from the samples S-300, S-380, S-460 and S-540 at low magnification (500 x) using the Secondary Electron (SE) detector are shown in Figs. 3.6(a) to (d) respectively.

It is observed that porosity and macro-crack density have decreased with increasing compaction pressure. The porosity levels, obtained through image analysis using the Axio-vision software, of ~ 2.2% and ~ 1.2% observed in the samples S-300 and S-380 reduced to ~ 0.2% in the samples S-460 and S-540. The average pore diameter of ~ 30 μm observed in the sample S-300 reduced to ~ 5 μm in the sample S-540. The quantum of porosity, pore sizes and macro-crack density were estimated in the samples, and those quantities are listed in table 3.2. These parameters are significantly smaller than those reported in MG processed REBCO samples [16, 19, 31, 32].

FE-SEM images obtained from the samples S-300, S-380, S-460 and S-540 using an in-lens detector at a magnification of 5000x, are shown in Figs. 3.6(e) to (h) respectively. The corresponding histograms showing particle size distributions are shown in Figs. 3.6(i) to (l) respectively. The Y-211 particle size is observed to become finer as the compaction pressure in enhanced. Also, the uniformity of Y-211 distribution improves with increasing compaction pressure. The Y-211 particles are found to be in the size range 200 nm – 4 μm. The minimum size of such particles is ~ 200 nm, and the number of submicron particles is maximum in the samples S-460 and S-540. In the sample S-460, the volume fraction of Y-211 particles of size above 1 μm is about 27%, while the total Y-211 content is ~ 46% including submicron particles. It might be recalled that no grain-refining compounds like Pt, PtO_2, CeO_2 were used in the present experiments.
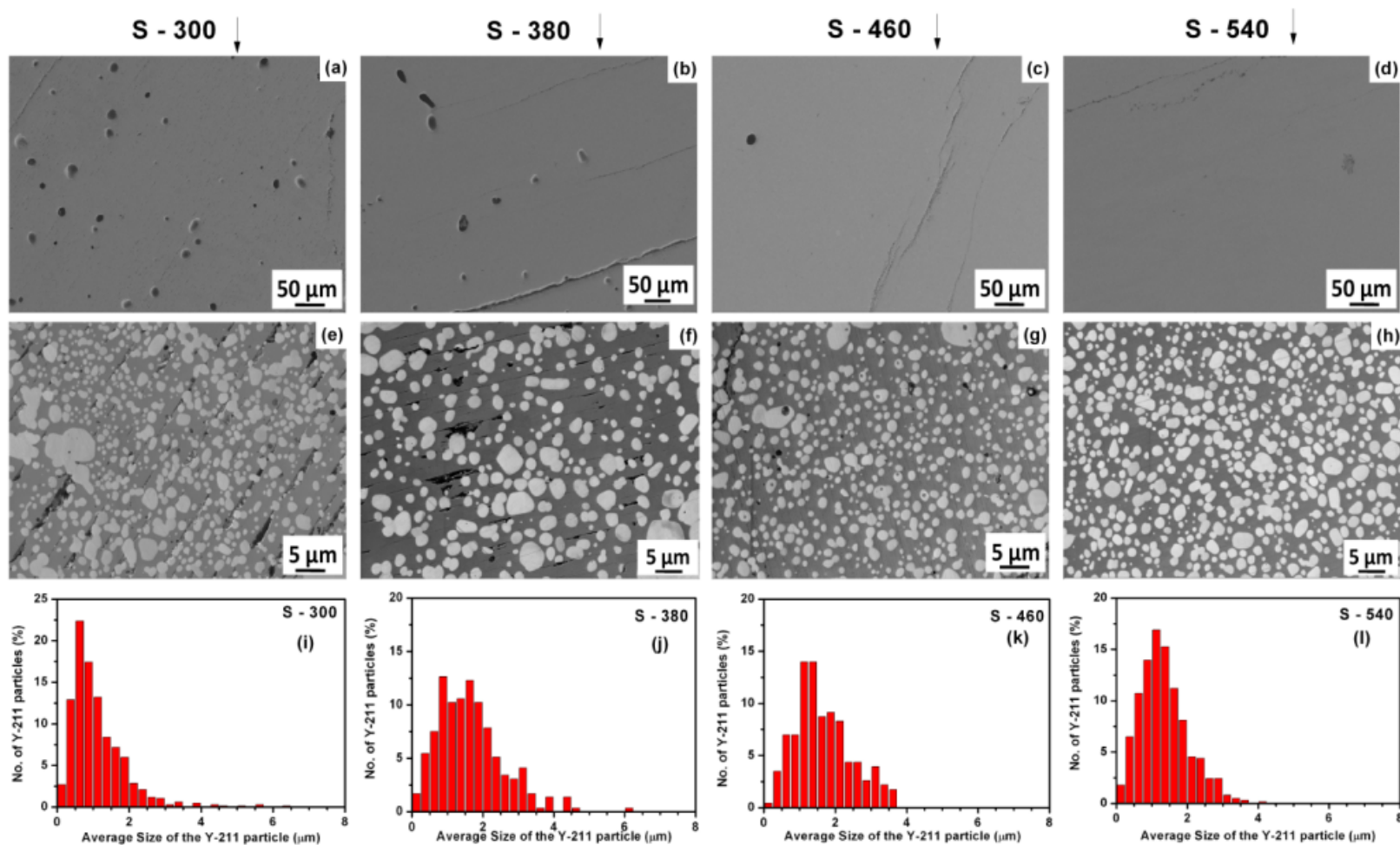
Fig. 3.6. FE-SEM images obtained from the samples S-300, S-380, S-460 and S-540 at low magnification (500 x) using SE detector are shown in (a), (b), (c) and (d) respectively. The images obtained from the samples S-300 to S-540 at a magnification of 5000 x using in-lens detector are shown in (e) to (h) respectively. The particle size histograms obtained for the images (e) to (h) are shown in (i) to (*l*) respectively.

3.4.2 Effect of preform compaction pressure on the spatial homogeneity in the distribution of Y-211 particles in Y-123 matrix.

In order to assess the spatial uniformity in the distribution of Y-211 particles in Y-123, specimens were collected from each sample from four different locations *A, B, C* and *D; A* is close to the seed crystal, and *D* is far away from the seed crystal, as marked in Fig. 3.7.
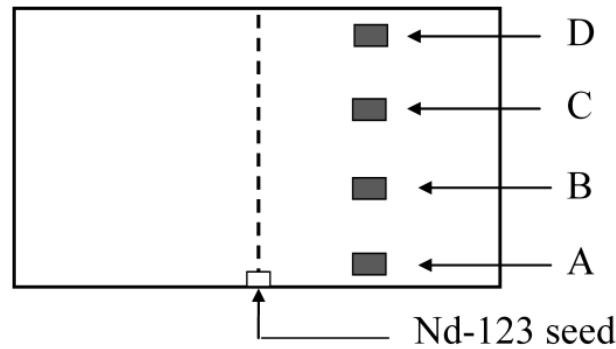
Fig. 3.7. A schematic diagram showing the positions *A*, *B*, *C* and *D*, at different distances from the Nd-123 seed crystal, from where specimens to study microstructure were collected.

FE-SEM micrographs obtained at 5000x in samples S-300 to S-540 are shown in Figs. 3.8(a) to (d) respectively. Each horizontal panel consists of micrographs recorded from a single sample in the regions *A* to *D*, as shown in the figures. The Y-211 particles can be observed to be uniformly distributed in the volume of the Y-123 matrix.
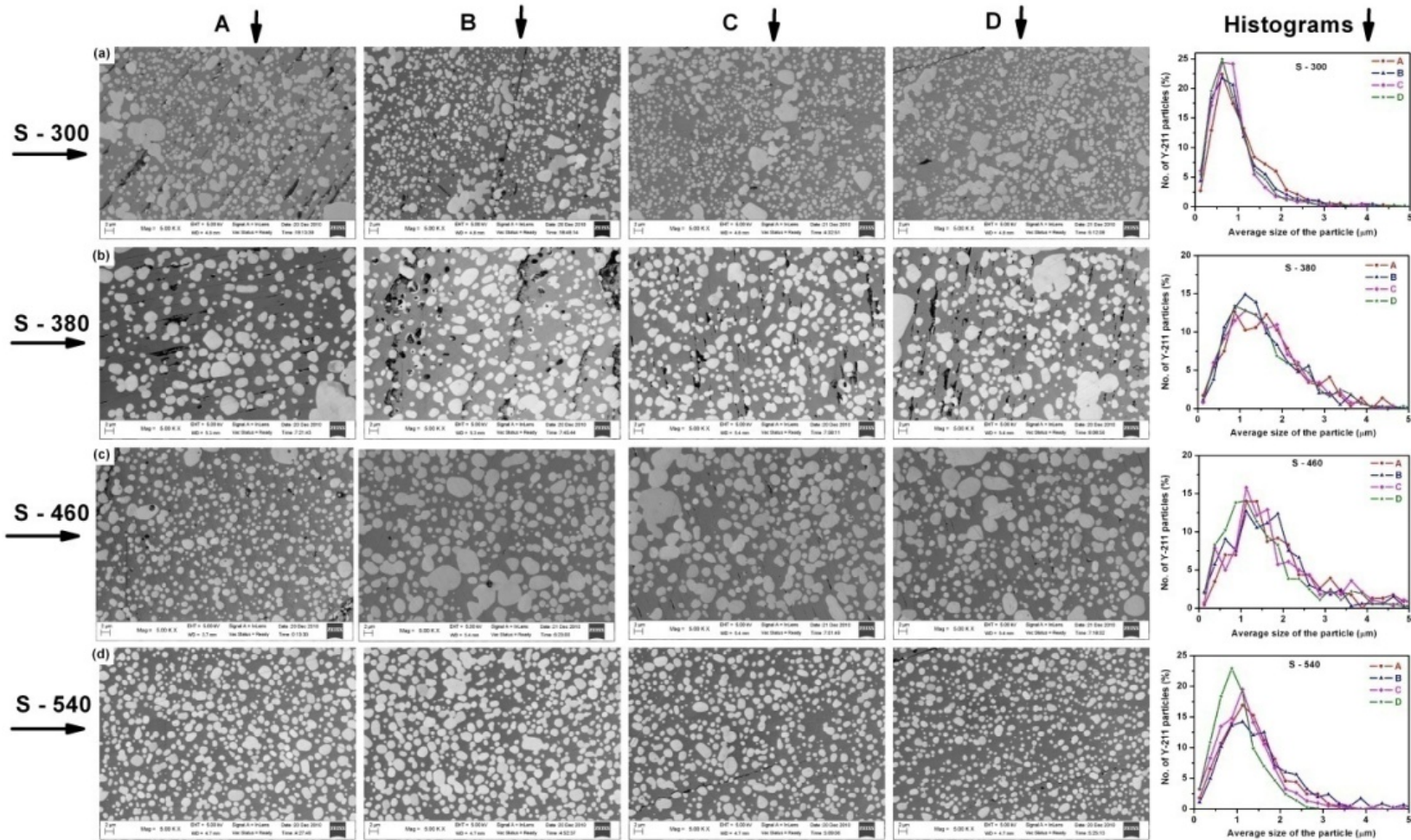
Fig. 3.8. Rows (a) to (d) show FE-SEM images obtained at a magnification of 5000 x from the samples S-300 to S-540 respectively. In each row, from left to right, are micrographs obtained from specimens extracted from areas *A*, *B*, *C* and *D* respectively, i.e. from regions close to the seed crystal to regions away from the seed crystal. We note that the samples have similar uniform microstructures independent of from where the specimens were extracted. The particle size histograms obtained for each of the samples are shown in the last column of the figure.

76

The Y-211 content in different regions of the samples was quantitatively estimated using Carl Zeiss Axio-Vision software and is given in table 3.2.

Table 3.2.   Comparison of various microstructural properties of YBCO superconductors fabricated by POIGP

Sample	S - 300	S - 380	S - 460	S - 540
Size of pores /voids (μm)	2 – 20 μm	5 – 30 μm	2 - 10 μm	2 - 5 μm
Porosity (%)	2.2 %	1.2 %	0.2 %	0.2 %
Size range of macro-crack widths (μm)	< 6 μm	< 6 μm	< 6 μm	< 6 μm
Macro-crack fraction (%)	0.6 %	4 %	0.8 %	0.9 %
Size range of Platelet width (μm)	0.7 – 2.3 μm	0.6 – 2 μm	0.8 - 2 μm	0.8 – 1.2 μm
Avg. Platelet width	1.2 μm	1.3 μm	1.3 μm	1 μm
Size range of Platelet gap (μm)	20 - 40 nm	20 – 50 nm	20 – 40 nm	30 – 50 nm
Avg. Platelet gap	30 nm	30 nm	30 nm	40 nm
Distribution of Y-211 particles	Uniform	Uniform	Uniform	Uniform
Size range of Y-211 particles (μm)	Sub-micron – 4 μm	Sub-micron – 4 μm	Sub-micron – 4 μm	Sub-micron – 4 μm
Size range in which the majority of the Y-211 particles were present	0.5 – 1 μm	0.5 - 2 μm	1 – 1.5 μm	0.5 – 2 μm
Vol. fraction of Y-211 (%) (Range as estimated from four different regions *A, B, C* and *D*)	40.3 – 43.1	34.2 – 38.1	45.6 – 46.9	47.1 – 48.5
Average content of the Y-211 particles	42 %	36.8 %	46.3 %	47.8 %

The Y-211 content varied only in a narrow range of ∼ 1 - 4 % at different distances from the seed crystal in the present samples, which is a significant improvement over variations of ∼2 - 40 % reported in literature [10, 27]. This drastic variation in the content of Y-211 reported in literature is common to both MG [26, 27] and IG [9, 10] processed samples. The number of Y-211 particles in different diameter ranges (200 nm to 8 microns) was measured from the FE-SEM micrographs, divided by the total number of Y-211 particles in the field of view; and the corresponding percentages are plotted as function of size of the particles for the samples S-300 to S-540, in Fig. 3.8. One can observe from the histograms that the distribution of Y-211 particles in the Y-123 matrix is quite similar in all the four regions of the samples and they peak in the size range ∼ 0.5 - 2 microns for all the samples.

It is evident from Fig. 3.8 and table 3.2 that the IGP samples of the present work showed spatial uniformity in the distribution of Y-211 particles when compared to MG and IG processed samples reported in literature [9, 10, 26, 27].

3.5   Magnetic hysteresis loops and critical current densities

Magnetization hysteresis (*M-H*) loops were recorded on all the samples from S-300 to S-540 at temperatures of 50 K and 77 K using a Physical Property Measurement System (PPMS) of Quantum Design-make. J_c was calculated following extended Bean's critical state model [33, 34] as discussed in Section 2.6.2 of Chapter II.

3.5.1   Field dependence of current densities at different temperatures

The field dependence of current density obtained in samples S-300, S-380, S-460 and S-540 at 50 K is shown in Fig. 3.9(a). It is evident that all the samples show nearly flat $J_c(H)$ response to fields as high as 13 Tesla. Fig. 3.9(b) shows $J_c(H)$ of the samples at 77 K. The samples S-460 and S-540 showed a $J_c(0)$ of 19.2 kAcm^{-2} and 27.4 kAcm^{-2} respectively at 77 K. On application of magnetic field, S-460 maintained

J_c better than 10^3 Acm^{-2} up to applied fields of 6.5 Tesla at 77 K and better than 25 kAcm^{-2} up to 13 Tesla at 50 K. It can be seen that the samples made under higher preform compaction pressures (S-460 and S-540) are able to retain the improved J_c to high fields unlike the samples S-300 and S-380 made under lower preform compaction pressures. The field dependences of J_c of the present samples are superior to those without nano-dopants / grain refiners etc. reported in MG and IG processed samples in literature [2-27].
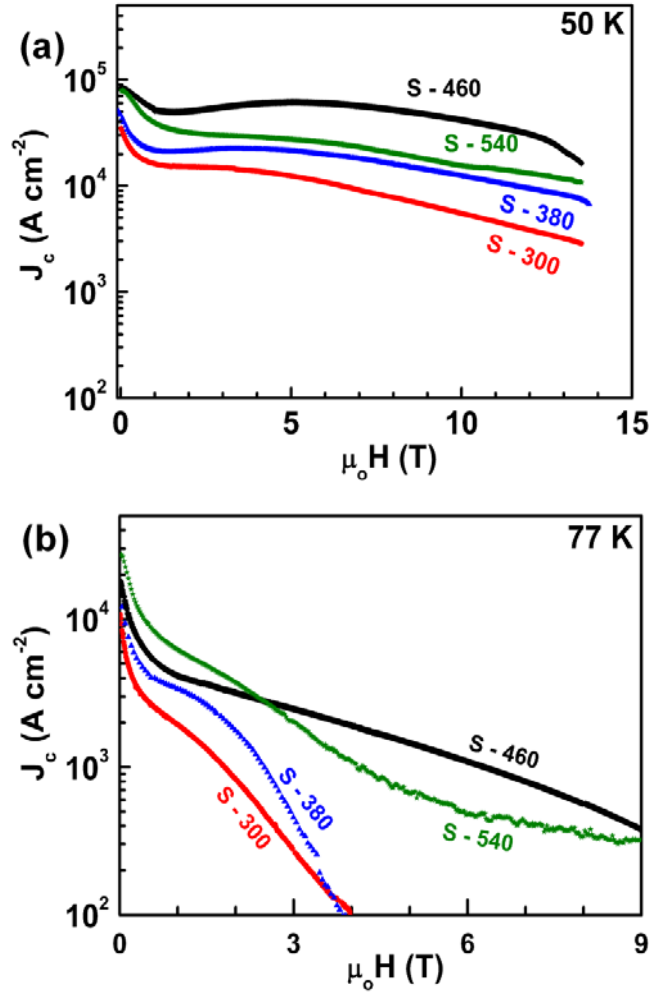
Fig. 3.9. $J_c(H)$ at (a) 50 K and (b) 77 K of samples whose Y-211 preforms were fabricated at different pressures between 300 MPa and 540 MPa are shown. It can be observed that the all the samples (S-300 to S-540) show significantly high *J_c* up to high applied magnetic fields. Among the samples under study, $J_c(H)$ for the sample S-460 is seen to be superior.

The parameters derived from J_c versus H plots at 50 K and 77 K are provided in table 3.3

Table 3.3. Comparison of various parameters obtained from the field dependences of J_c obtained for samples studied.

Sample	Temperature	S - 300	S - 380	S - 460	S - 540
Zero field J_c $J_c(0)$ (kAcm^{-2})	77 K	10	12.8	19.2	27.5
	50 K	34.9	46.3	83.8	78.4
Field *H* by which J_c drops to 10^3 Acm^{-2} (T)	77 K	1.8 T	2.5 T	6.5 T	4.1 T
Field *H* by which J_c drops to 20 kAcm^{-2} (T)	50 K	0.4 T	5.8 T	13.2 T	8.3 T

A comparison of the results on the present sample (S-460) to the ones reported in literature is presented in table 3.4. The field dependence of current densities obtained in the sample S-460 is observed to be the best among those reported for YBCO superconductors with no added grain refiners / nano-dopants etc. The high field current densities of the optimized sample (S-460) maintained high current densities to large applied fields. The sample showed J_c better than 10^3 Acm^{-2} to fields of ~ 6.5 Tesla at 77 K. This value for J_c at such high fields is superior compared to many of the REBCO samples with added grain refiners and nano-dopants as can be seen in table 3.4.

Table 3.4. Zero field J_c and $J_c(H)$ of samples fabricated by MG and IG processing techniques from the literature, in comparison with the results from the present work.						
Sample	**Process**	**T_c and ΔT_c (K)**	**Performance at 77K**		**Remarks[$]**	**Ref.**
			J_c (0) kAcm^{-2}	**H*(J_c=10^3 Acm^{-2})**		
Nd-123 + 20% Nd-422	IGP	93 K 1 - 2 K	40	0.25 T		4
YBCO + 0.8 wt% PtO$_2$	IGP	90K - 91.5K 1.5 K	95	3 T	a, b	9
Y-123 + 28 vol.% Y-211 + 0.8 wt.% PtO$_2$	IGP	89.5K – 91K 1 K	80	2.5 T	a, b	10
Y-123 + Y-211 + 0.5 wt.% CeO$_2$	IGP	86K - 90K 4 K	15	4 T	b, c	11
Y-123 + Y-211 + 0.5 wt.% CeO$_2$ +0.1 mol% nm Sm-211	IGP	No info.	22	4 T		11
Y-123 + Y-211 + Pt	MGP	No info.	45	1 T		14
Y-123 + Y-211 + 0.2 wt% Pt	MGP	86K – 90K 5 K	22.5	1.9 T	b, c	26
Y-123 + Y-211	IGP	No info.	12	5 T		30
Y-123 + 30 mol.% Y$_2$O$_3$ + 0.1 wt.% DU + 0.1 wt.% Pt	TSMG	No info.	70	3.75 T	a	39
(NSG)BCO + 10 mol% NSG-211 + 0.5 mol% Pt + 1 mol% CeO$_2$	MGP	93 K 1 K	40	5 T	PE observed	40
Y-123 + nano Y-211 + 1 wt% CeO$_2$	MGP	No info.	100	3.5 T	PE observed	41
Y-123 with Y-211 + 1 wt.% CeO$_2$	MGP	No info.	40	3.25 T	PE observed	41
Y-123 + 30% nano Y-211 + 0.3 % Pt	MGP	No info.	20	2.0 T	Nano Y-211	42
Y-123 + 20mol% Y-211 +10 mol% Y-2411 +0.05% Pt	MGP	No info.	80	5.5 T		43
Y-123	MGP	No info.	5	3 T		43
Y-123 with Y-211	MGP	No info.	35	3.5 T		43
Y-123 + Y-211 + Pt	MGP	90.5 K	21	5 T		44
YBa2(Cu0.$_{95}$Al0.$_{05}$)$_3$O$_7$	MGP	90 K	23	3 T		45
YBCO + 42 vol.% Y-211	**IGP**	**92.1 K 0.6 K**	**19.2**	**6.5 T**	**Present Work (sample S-460)**	

[$] **a** represents inhomogeneity in the distribution of RE-211, **b** represents non-uniformity in $J_c(H)$ and **c** represents distribution in T_c across the volume of the bulk

* **H*** represents the field by which J_c reaches 10^3 Acm^{-2}; PE stands for Peak Effect

3.5.2 Uniformity of current densities in Y-Ba-Cu-O superconductors fabricated by POIGP

It is known from literature that the inhomogeneity in the distributions of Y-211 is often the cause for observing non-uniformity in the superconducting properties in MG / IG processed samples. This was attributed to the pushing effects of fine sized particles during the growth of Y-123 from Y-211 and the liquid phases [28, 29]. This variation was illustrated through the field dependences of J_c obtained from different regions of the samples containing different amounts of Y-211 [10]. Since we have obtained a homogenous distribution of Y-211 particles across the volume of the YBCO samples fabricated by POIGP, it becomes interesting to investigate the uniformity in superconducting properties in the present samples.

For this purpose, two specimens were chosen from the sample S-460, which showed superior $J_c(H)$: one close to seed crystal, marked as **A** and the other away from the seed crystal, marked as **D**, in Fig. 3.7. The specimens are referred as S-460-A and S-460-D corresponding to the regions from where they are collected. *M-H* loops were recorded in the specimen S-460-A and S-460-D at 77 K by varying *H* up to 10 Tesla. $J_c(H)$ obtained for these specimens is shown in Fig. 3.10.
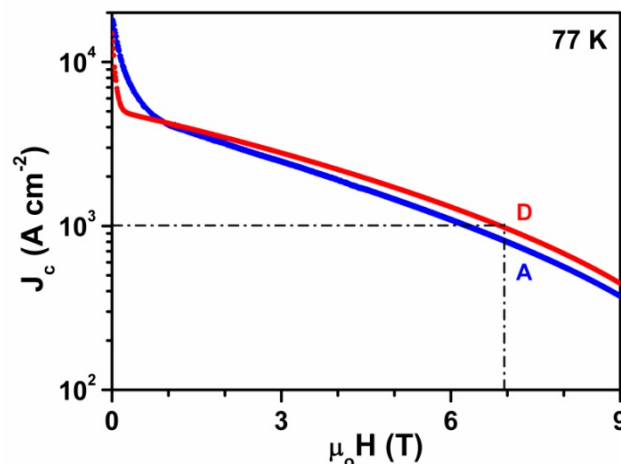
Fig. 3.10. The magnetic field dependence of J_c at 77 K for two specimens collected from regions **A** and **D** of the POIGP sample. Though the regions **A** and **D** are quite far from one another in the POIGP sample with one region close to the seed, and the other far, the close proximity of the two $J_c(H)$ curves is important: it shows the excellent microstructural uniformity in the volume of the POIGP sample.

82

It is evident from the figure that the variation of J_c with H in the region D almost overlaps with that in the region A for the sample S-460. This convincingly establishes the spatial uniformity of J_c in the samples synthesized by the POIGP.

3.5.3 Flux pinning force and its field dependence in Y-Ba-Cu-O superconductors fabricated by POIGP

The effective flux pinning observed in different field regimes of the samples S-300, S-380, S-460 and S-540 is investigated. The flux pinning force F_p is given as

$$F_p = J_c \times \mu_o H \quad ....(3.1)$$

where J_c is the critical current density and H is the applied field.

The field dependences of the flux pinning force obtained for the samples S-300 to S-540 are shown in Fig. 3.11(a). It is evident from the figure that the flux pinning force is high for samples S-460 and S-540 which were made from Y-211 preforms fabricated under higher compaction pressures of 460 MPa and 540 MPa respectively. The samples which were made from preforms fabricated under lower compaction pressure showed smaller flux pinning forces. The flux pinning force in each case is normalized with respect to the maximum pinning force ($F_{p\,max.}$) and the normalized flux pinning force ($F_p / F_{p\,max.}$) is plotted as a function of applied field for all the samples in Fig. 3.11(b).
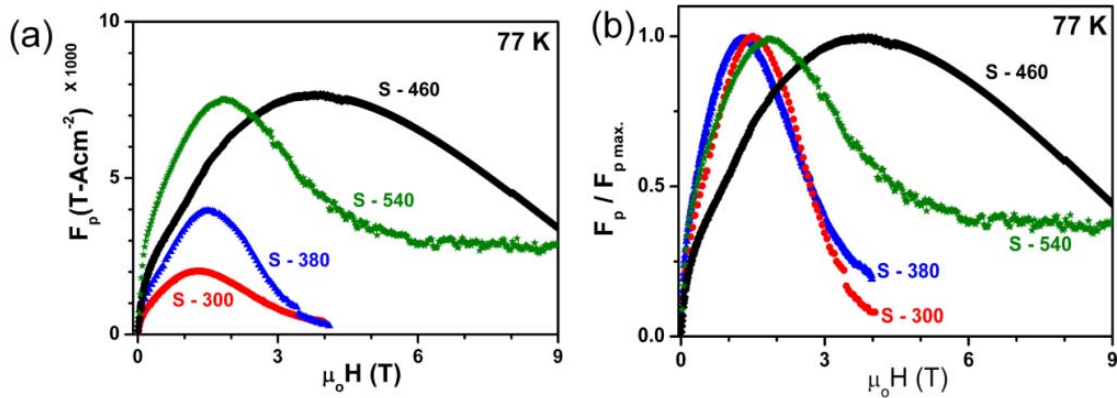
Fig. 3.11. The field dependence of (a) the flux pinning force F_p and (b) the normalized flux pinning force $F_p / F_{p\,max}$ for the samples S-300 to S-540 at 77 K are shown. The curve for sample S-460 peaks at the maximum field of 4 T.

It can be observed from the figure that $F_p / F_{p\ max.}$ shows peak at 1.4 T in samples S-300 and S-380, at 1.8 T for sample S-540 and at a much higher field of 4 T for the sample S-460. The flux pinning is significantly enhanced at high fields for the sample S-460 while it is moderately improved for the sample S-540.

3.5.4 Normalized critical current densities and exponential model

The field dependence of current density is reported to follow exponential variation in melt processed YBCO superconductors with high J_c [35, 36]. In order to investigate the origin of enhanced flux pinning in the present samples in different field regimes at 77 K, we have normalized the field dependences of J_c to the respective zero-field J_c as $J_c(H) / J_c(0)$, and it is plotted as a function of applied field and is shown in Fig. 3.12 (a).
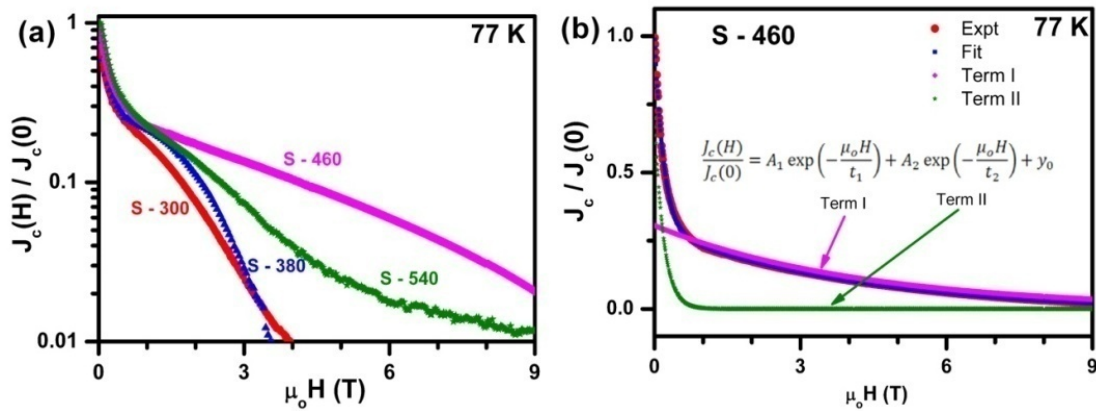
Fig. 3.12. (a) The variations of normalized current density $J_c(H) / J_c(0)$ at 77 K with applied field for the samples S-300 to S-540 are shown. It can be seen that the sample S-460 shows superior J_c to high fields. (b) For the S-460 sample at 77K, the normalized J_c is fitted to a function in H with two exponential terms as discussed in the text. An excellent fit with regression factor 99.99 is obtained. One of the terms fits the low field region and the other, the high field region.

It is evident from the figure that while the field dependence is similar for all the samples at low fields (< 1.8 T), it deviates in samples S-460 and S-540 above 1.8 T, suggesting an additional pinning mechanism operative at higher fields.

We investigated if the observed field dependence of the present samples can be associated with different pinning mechanisms operative at low and high fields, each exhibiting an exponential dependence on applied field. Exponential fits were made to the field dependences of J_c normalized to their zero field value at 77 K, for all the samples. It is observed that the $\frac{J_c(H)}{J_c(0)}$ fits very well to exponential decay containing two terms as shown below:

$$\frac{J_c(H)}{J_c(0)} = A_1 \exp\left(-\frac{\mu_o H}{t_1}\right) + A_2 \exp\left(-\frac{\mu_o H}{t_2}\right) + y_0 \quad \dots\dots\dots\dots(3.2)$$

where A_1, t_1, A_2, t_2 and y_0 are the fit parameters. The fit for sample S-460 is shown as a typical example in Fig. 3.12(b). In the figure, we have also plotted the contribution from the individual terms in the equation. One observes that Term-1 (with A_1 and t_1) is operative at high magnetic fields whereas Term-2 (with A_2 and t_2) is operative at low fields. The regression factors of the fits were close to 1 for all samples. The fit parameters are given in table 3.5.

Table 3.5. Fit parameters for the POIGP samples S-300 to S-540

Sample	Fit Parameters					Regression factor
	y_0	A_1	t_1	A_2	t_2	
S-300	-0.022	0.392	1.453	0.680	0.082	0.999
S-380	-0.044	0.425	1.906	0.629	0.093	0.993
S-460	-0.015	0.306	4.202	0.722	0.185	0.999
S-540	0.008	0.397	1.693	0.763	0.162	0.999

It is clear from the above observations that effectively two different mechanisms can account for the enhanced flux pinning observed to very high fields particularly in the S-460 and S-540 samples. It is known from literature [37] that the

85

size of the defects can influence J_c giving rise to observation of a peak in J_c at a particular field, defined as peak field. The peak field is related to the vortex lattice spacing as:

$$H_p = \frac{2\emptyset_o}{\sqrt{3}(a_f)^2} \quad \text{...............(3.3)}$$

where ϕ_o is the flux quantum, a_f is the vortex lattice spacing [37]. Eq. **3.3** suggests that flux pinning at fields less than 1 T can be caused by defects of size more than 50 nm. It is established that the Y-123/Y-211 interfacial defects would give rise to flux pinning at such low fields [23, 24, 38]. Fig. 3.13(a) shows that the fit parameter **A₂** of the exponential decay at low fields, increases with increasing Y-211 content. It is also observed that $J_c(0)$ varies with Y-211 content as shown in Fig. 3.13(b). The correlations observed support the view that the flux pinning at low fields depends on the Y-211 content and possibly originates in defects at the Y-211/Y-123 interfaces.
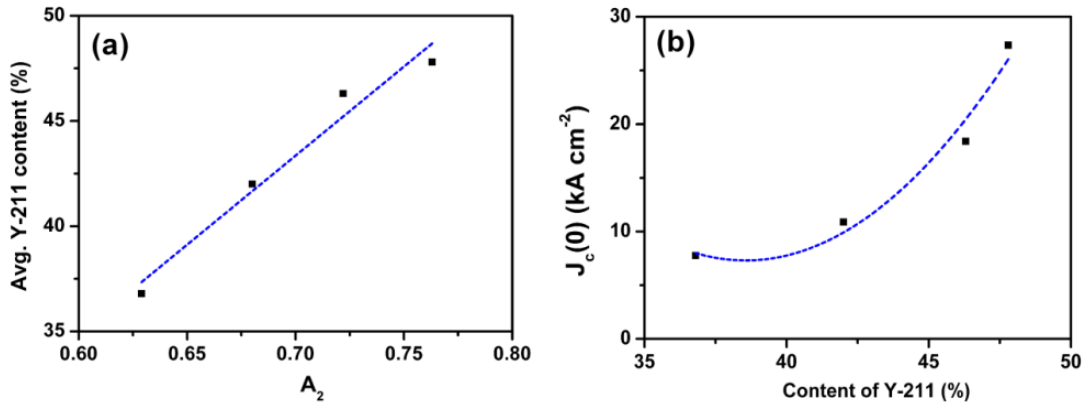
Fig. 3.13. (a) The fit parameter A_2 (obtained from the exponential decay equation fitted in the low field regions for all the samples and presented in table 3.2) is plotted against the Y-211 content estimated from the FE-SEM micrographs using axio-vision software. A linear increase of **A₂** with Y-211 content is seen. In (b), we show the variation of $J_c(0)$ of the samples as a function of their Y-211 content. $J_c(0)$ is found to increase with the Y-211 content. The correlations seen in (a) and (b) support the possibility that the low-field J_c is governed by interfacial defect densities through the Y-211 content.

We thus conclude that the low field J_c is controlled by the Y-211 content. Hence it is quite crucial to control the content of fine sized Y-211 particles in the matrix of Y-123 since the surface area of these non-superconducting inclusions in the matrix of Y-123 plays an important role in enhancing the flux pinning at low fields.

There is no clear understanding in literature regarding the factors that would contribute to high J_c at high applied fields. As the sample S-460 showed superior $J_c(H)$ compared to all other POIGP samples, further investigations have been carried out in detail using various microscopic techniques like Field Emission Electron Microscopy (to higher magnifications), Electron Back Scattered Diffraction studies and Transmission Electron Microscopy. The details obtained from these studies are presented in chapter VI.

References

[1]   Rajasekharan T, Sudhakar Reddy E, Viswanath N V N, Hari Babu N and Seshu Bai V 1996 *Proceedings of ASMCCD symposium* Mumbai India

[2]   Sudhakar Reddy E and Rajasekharan T 1998 *Supercond. Sci. Technol* **11** 523

[3]   Sudhakar Reddy E and Rajasekharan T 1998 *J. Mater. Res.* **13** 2472

[4]   Hari Babu N, Rajasekharan T, Latika Menon and Malik S K 1999 *J. Am. Ceram. Soc.* **82** 2978

[5]   Viswanath N V N, Rajasekharan T, Harish Kumar N, Menon L and Malik S K 1998 *Supercond. Sci. Technol.* **11** 420

[6]   Chen Y L, Chan H M, Harmer M P, Todt V R, Sengupta S and Shi D 1994 *Physica C* **234** 232

[7]   Cloots R, Koutzarova T, Mathieu J-P and Ausloos M 2005 *Supercond. Sci. Technol.* **18** R9

[8]   Meslin S, Iida K, Hari Babu N, Cardwell D A and Noudem J G 2006 *Supercond. Sci. Technol*. **19** 711

[9]   Iida K, Hari Babu N, Withnell T D, Shi Y, Haindl S, Weber H W and Cardwell D A 2006 *Physica C* **445–448** 277

[10]   Iida K, Hari Babu N, Shi Y and Cardwell D A 2005 *Supercond. Sci. Technol*. **18** 1421

[11]   Chen S-Y, Hsiao Y-S, Chen C-L, Yan D-C, Chen I-G and Wu M-K 2008 *Mater. Sci. Eng. B* **151** 31

[12]   Meslin S and Noudem J G 2004 *Supercond. Sci. Technol*. **17** 1324

[13]   Jin S, Tiefel T H, Sherwood R C, Davis M E, van Dover R B, Kammlott G W, Fastnacht R A and Keith H D 1988 *Appl. Phys. Lett.* **52** 2074

[14] Murakami M, Morita M, Doi K and Miyamoto K 1989 *Jpn. J. Appl. Phys.* **28** 1189

[15] Sudhakar Reddy E, Sastry T V R K and Rajasekharan T 1999 *Mater. Lett.* **38** 62

[16] Gopalan R, Rajasekharan T, Roy T and Rangarajan G 1996 *J. Mater. Sci.* **31** 2557

[17] Hari Babu N, Rajasekharan T and Seshu Bai V 2000 *Physica C* **330** 203

[18] Hari Babu N, Rajasekharan T and Seshu Bai V 1998 *Eur. Phys. J. B* **4** 55

[19] Sudhakar Reddy E and Rajasekharan T 1998 *Supercond. Sci. Technol.* **11** 183

[20] Sudhakar Reddy E and Schmitz G J 2002 *Supercond. Sci. Technol.* **15** L21

[21] Sudhakar Reddy E, Noudem J G, Tarka M and Schmitz G J 2000 *Supercond. Sci. Technol.* **13** 716

[22] Sudhakar Reddy E and Schmitz G J 2002 *Supercond. Sci. Technol.* **15** 727

[23] Salama K and Lee F Dominic 1994 *Supercond. Sci. Technol.* **7** 177

[24] Lee D F, Selvamanickam V and Salama K 1992 *Physica C* **202** 83

[25] Leblond C, Monot I, Provost J and Desgardin G 1999 *Physica C* **311** 211

[26] Jiao Y L, Xiao L, Ren H T, Zheng M H and Chen Y X 2003 *Physica C* **386** 266

[27] Chow J C L, Leung H T, Lo W and Cardwell D A 1998 *J. Mater. Sci.* **33** 1083

[28] Diko P, Zmorayova K, Granados X, Sandiumenge F and Obradors X 2003 *Physica C* **384** 125

[29] Diko P, Zmorayova K, Hari Babu N and Cardwell D A 2003 *Physica C* **398** 1

[30] Mahmood A, Jun B H, Park H W and Kim C J 2008 *Physica C* **468** 1350

[31] Sudhakar Reddy E and Rajasekharan T 1998 *Phys. Rev. B* **57** 5079

[32] Diko P and Krabbes G 2003 *Supercond. Sci. Technol.* **16** 90

[33] Bean C P 1962 *Phys. Rev. Lett.* **8** 250

[34] Chen D X and Goldfarb R B 1989 *J. Appl. Phys.* **66** 2489

[35] Ganesan V, Srinivasan R, Gopalan R and Rajasekharan T 1993 *Pramana J. Phys.* **41**, 61

[36] Yang T, Wang Z H, Zhang H, Nie Y and Qiu L 2003 *Physica C* **386** 69

[37] Nakamura M, Hirayama T, Yamada Y, Ikuhara Y and Shiohara Y 1996 *Jpn. J. Appl. Phys.* **35** 3882

[38] Kim C-J and Hong G-W 1999 *Supercond. Sci. Technol.* **12** R27

[39] Hari Babu N, Kambara M, Shi Y-H, Cardwell D A, Tarrant C D and Schneider K R 2002 *Supercond. Sci. Technol.* **15** 104

[40] Muralidhar M, Jisra M, Sakai N and Murakami M 2003 *Supercond. Sci. Technol.* **16** R1

[41] Yeoh W K, Pathak S K, Shi Y-H, Dennis A R, Cardwell D A, Hari Babu N, Iida K and Strasik M 2009 *Supercond. Sci. Technol.* **22** 065011

[42] Li F, Vipulanandan C, Zhou Y X and Salama K 2006 *Supercond. Sci. Technol.* **19** 589

[43] Hari Babu N, Iida K, Shi Y, Withnell T D and Cardwell D A 2006 *Supercond. Sci. Technol.* **19** S461

[44] Wei C D, Liu Z X, Ren H T and Xiao L 1996 *Physica C* **260** 130

[45] Diko P, Antal V, Kaňuchová M, Šefčiková M and Kováč J 2009 *Supercond. Sci. Technol.* **22** 065005

CHAPTER IV

YBCO/Ag SUPERCONDUCTING COMPOSITES FABRICATED USING POIGP

4.1   Introduction

4.1.1   Addition of Ag into REBCO superconductors: A literature survey

Over the years, efforts have been made by several groups to introduce Ag into the REBCO superconductors to modify the microstructures [1-4] and improve the mechanical properties [5, 6] without reducing their critical current densities [7, 8]. Considerable work has been done on MG processed REBCO/Ag composites by adding Ag_2O to the bulk precursor pellet [1-3, 5, 6]. Whether the addition of Ag itself enhances the J_c in REBCO superconductors is still controversial [7-11]. Some groups have introduced Ag_2O as a source of silver [1-6] while some others have used metallic silver to fabricate RE-123/Ag superconductors [4, 7, 9-16]. A detailed study of various reports on Ag doped RE-123 superconductors reveals that the addition of silver reduces the gaps between platelets [1, 10, 15] and causes refinement of RE-211 precipitates in the RE-123 matrix [15, 17]. However, a close examination shows that distribution of Ag and RE-211 are spatially non-uniform in the matrix and that the degree of porosity is substantial (2-30 %) [1-17].

Mendoza et al. [1] observed that J_c enhanced with an addition of 20 wt.% Ag_2O into melt textured YBCO superconductors and have attributed it to the reduction in the density of micro-cracks. Diko et al. [2] studied the effect of Ag_2O on the microstructures of melt grown YBCO/Ag superconductors and have observed that a high growth rate causes elongation of Ag particles in the growth direction. They reported that the size and morphology of Ag particles differ appreciably in each of the distinct growth regions of YBCO/Ag superconductor.

Only a few reports are available on the addition of Ag to YBCO through IG process and its effect on the field dependence of critical current densities '$J_c(H)$' [4,

12-14]. Iida et al. [4] recently discussed various arrangements for introducing Ag_2O into YBCO bulk superconductors fabricated by the IG process. Their arrangement comprised of Y-211 preform supported on a liquid phase source pellet (Y-123 + $Ba_3Cu_5O_8$) with the infiltration process capillary-aided. They observed that homogeneity in the distribution of Ag was best when Ag_2O was added to both Y-211 preform and liquid phase source in equal proportions. They also reported that the porosity which remained in the end products reduced substantially by employing metallic Ag instead of Ag_2O. The porosity in the Ag_2O added samples was attributed to evolution of oxygen during IG processing. However, the Y-211 distribution in their samples remained inhomogeneous even with Ag addition. The Ag particles in the end product were acicular and large-sized (20 -150 microns).

4.1.2. Need for addition of Ag into YBCO superconductors fabricated by POIGP

We have reported in Chapter III that the current densities supported by IG processed YBCO can be enhanced by optimizing the pressure under which the required preforms are prepared and by optimizing the sintering temperature. The current density and its field dependence obtained in the YBCO samples fabricated by POIGP was found to be much better in comparison with those in samples prepared by both MG and IG processes without nano-dopants, Y-211 grain refiners or solid solution formers. The samples thus obtained by POIGP have shown a homogeneous distribution of fine particles of Y-211 in Y-123 matrix as seen from Fig. 4.1(a). The J_c and its dependence on magnetic field (H) remained the same in different regions as discussed in the previous chapter. Porosity could be minimized by the process. However, macro-cracking and platelet gaps were not completely eliminated in the samples as can be seen from Figs. 4.1(b) and (c).
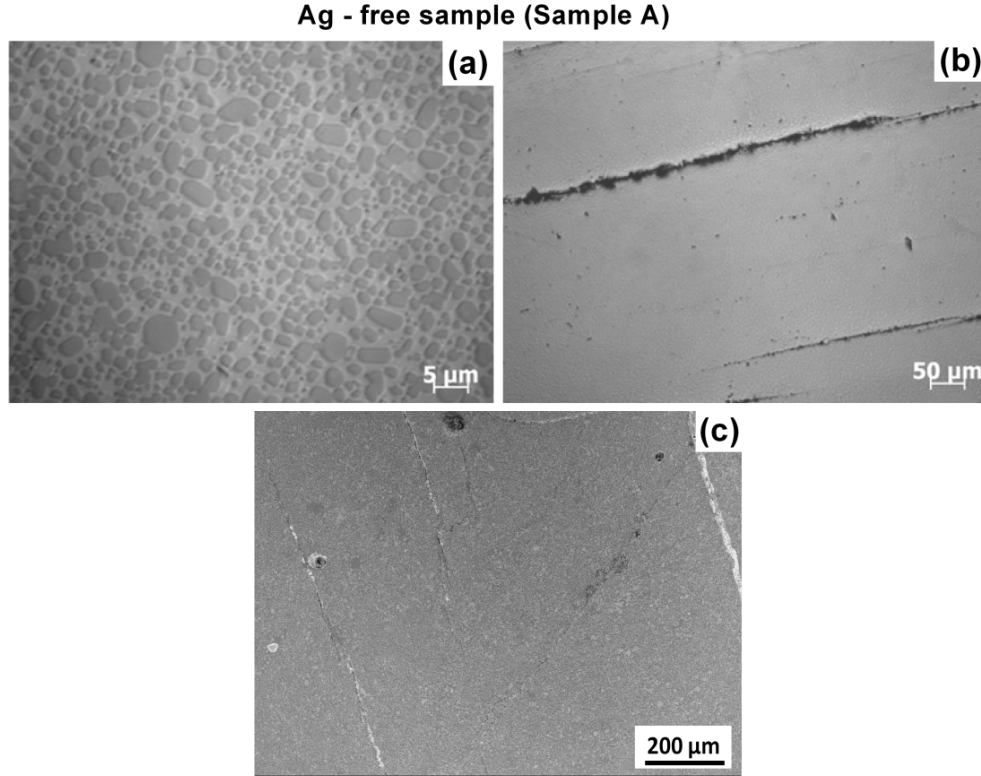
Fig. 4.1. Optical micrographs obtained from the sample without Ag addition (i. e. Sample A): (a) at 1000x and (b) at 200x. In (c), an FESEM image at 100x of the same sample is shown. Though the sample showed no macroscopic defects at high magnification as seen from (a), the micrographs at lower magnifications, (b) and (c), show the presence of cracks which was sought to be closed by the addition of Ag in this work.

The aim of the present work was to study the effect of introduction of silver into the POIGP samples. The interest was in investigating whether the favorable microstructural characteristics and high current densities observed up to high fields in the silver-free samples could be reproduced in the Ag containing samples. We used two different arrangements to introduce silver into the YBCO matrix and the outcomes of both are compared in the present work.

4.2 Fabrication of YBCO/Ag superconducting composites

Precursor powders of Y-123 and Y-211 were prepared by chemical route as discussed in Chapter 2. The sintered powders were found to contain particles with size ranging from sub-micron to 2 microns with the peak in the distribution around

1 µm. Preforms of Y-211 were fabricated out of the above powder in a steel die under a compaction pressure of 460 MPa, the pressure found to be optimal for best performance in our earlier work (please see the results reported in Chapter 3).

One set of preforms were fabricated with 10 wt.% of ~ 1 µm sized metallic silver powder mixed into the Y-211 powder uniformly in an agate mortar. Another set was made without the silver addition. For yet another experiment, the Ag powder was mixed in two different amounts (10 wt.% and 20 wt.% w.r.t. to the Y-211 preform) to the liquid phase source pellet (Y-123).   The experimental arrangement used in the work is shown in Fig. 4.2.
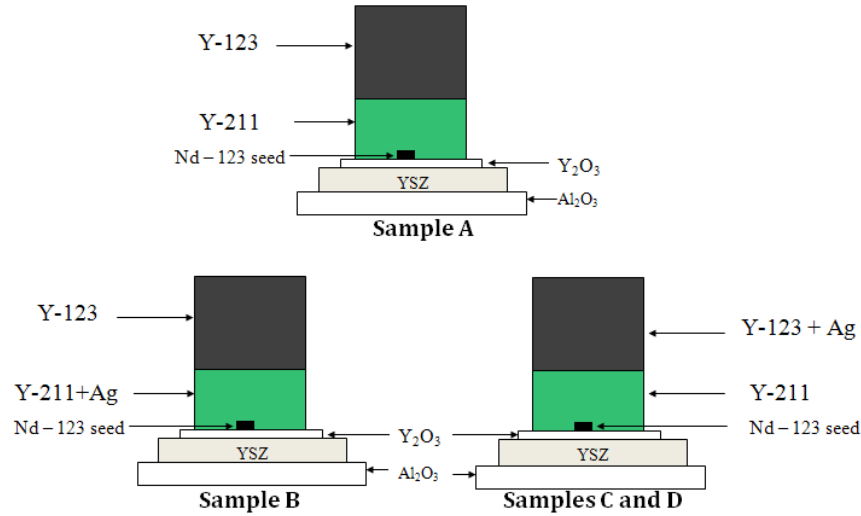
Fig. 4.2. The experimental arrangement used in the present study for fabricating YBCO/Ag composites employing POIGP. Sample *A* was fabricated without any Ag addition, Sample *B* was prepared by adding Ag directly to the Y-211 preform, and samples *C* and *D* were fabricated by adding Ag to the liquid phase source (Y-123) at the top.

The source for the liquid phases ($BaCuO_2$ and CuO) was Y-123, in pellet form, placed above the Y-211 preform. The assembly was supported with layers of Y_2O_3, Yttria-Stabilized Zirconia (YSZ) and alumina to minimize the outflow of liquid phases during heat treatment. The presence of Y_2O_3 and YSZ layers helps avoid contamination of the sample with alumina at elevated temperatures. $NdBa_2Cu_3O_7$ (Nd-123) seed was used to promote the textured growth of the Y-123/Ag superconductor during the POIGP. The sample assembly in each case was heat

treated in a tubular furnace as per the schedule shown in Chapter II in Fig. 2.10. The YBCO/Ag samples thus obtained were oxygenated in a tubular furnace at 460°C in flowing oxygen for 100 hours.

The product obtained with no silver added to either the preform or the liquid phase source is referred to hereafter in this chapter as Sample *A*. Sample *B* was obtained in an experiment with 10 wt.% of silver (w. r. t. to the weight of the Y-211 preform) added to the preform only. Samples *C* and *D* were obtained in experiments where 10 and 20 wt.% of silver (w. r. t. to the weight of the Y-211 preform) respectively were added to the liquid phase source and none to the preform. No Y-211 grain refiners like Pt, PtO_2 and CeO_2 etc. were added to any of the samples in the present study. The details of the Ag-containing samples are tabulated in table 4.1.

Table 4.1. Details of the YBCO and YBCO/Ag samples studied in the present work		
	Liquid Source Pellet	**Preform Pellet**
Sample *A*	Y-123	Y-211
Sample *B*	Y-123	Y-211 + 10 wt.% Ag
Sample *C*	Y-123 + 10 wt.% Ag	Y-211
Sample *D*	Y-123 + 20 wt.% Ag	Y-211

4.3 Microstructures of Ag-containing POIGP samples

Specimens were sliced from the samples *A, B, C* and *D* using a low speed saw for magnetic and microstructural studies. Thin sections from samples *B, C* and *D* drawn from regions marked schematically as P, Q, R and S in Fig. 4.3(a), were mounted in bakelite and polished on an auto-polisher under kerosene using diamond paste down to 0.25 μm size. The polished specimens were observed under an optical microscope with polarizer (Carl Zeiss, Axiovert) and a Field-Emission Scanning Electron Microscope (FE-SEM; Zeiss Ultra 55). The optical micrographs obtained at low magnification (50x) in samples *B, C* and *D* are shown in Figs. 4.3(b), (c) and (d) respectively.

Fig. 4.3. (a) A schematic diagram showing the positions from where specimens to study microstructure were collected. P, Q, R and S are at increasing distances from the Nd-123 seed crystal. Row (b), which corresponds to Sample B in which Ag was added to the preform, shows optical micrographs at 50x from the four regions P, Q, R and S. We observe that in all the regions, the microstructure is highly porous. Row (c) for Sample C with 10wt.% Ag added along with the liquid phase, has less porosity in all regions and show some amount of macro-cracks. Row (d) for Sample D with 20wt.% Ag added along with the liquid phase, has minimal porosity in all regions and show fewer cracks. In (b), large Ag particles can be seen (white in the figure) and the size of silver particles in (c) and (d) are below the resolution limit in the micrographs.

Each horizontal panel consists of micrographs recorded from four different regions starting from an area close to seed crystal {P in Fig. 4.3(a)} to an area away from the seed crystal {S in Fig. 4.3(a)}. The micrographs obtained from Sample *B* showed considerable porosity of 6 - 13.3 % and macro crack density, defined as the area occupied by the cracks relative to the area of the chosen frame, of ∼ 2.2 - 4 %, over different frames chosen across the thickness of the sample. Sample *C*, where 10 wt.% Ag was introduced along with the liquid phases, showed substantial reduction in porosity and macro-crack density relative to sample *B* as can be observed from Fig. 4.3(c). A porosity of 3.5 - 5% and a macro-crack density of 2 – 3% were measured in sample *C.* Sample *D*, in which 20 wt. % Ag was added to liquid phase source, showed negligible porosity in specimens drawn from all the regions P, Q, R and S, as can be seen from Fig. 4.3(d). Compared to the Ag-free sample whose microstructure is shown in Fig. 4.1(c), a systematic reduction in porosity and macro-crack density were observed with increasing Ag content when Ag was introduced through the liquid phase source. On the other hand, the microstructure was observed to deteriorate considerably when Ag was introduced directly into the Y-211 preform.

4.3.1 Effect of Ag on the size of Y-211 particles

The distribution of Y-211 particles in the POIGP samples '*A'* to '*D'* are shown in Figs. 4.4 (a) to (d) respectively.
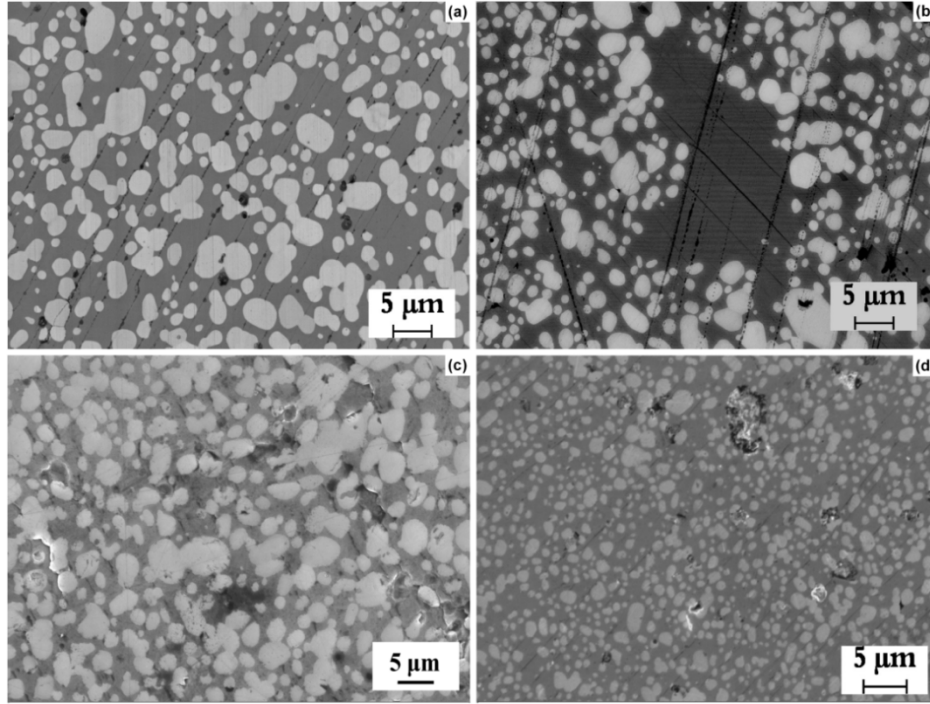
Fig. 4.4. Images from the POIGP samples *A*, *B*, *C* and *D* obtained using the in-lens detection mode of the Zeiss-make FE-SEM. A uniform distribution of Y-211 particles is observed in the micrographs (a), (c) and (d) from samples *A*, *C* and *D;* Sample A had no Ag and in Samples C and D, Ag was added along with the liquid phase. (b) In Sample *B* which was fabricated with Ag added to the Y-211 preform, the Y-211 distribution is not uniform. When Ag is introduced through the liquid phase source, the Y-211 particle size is refined, with the refinement becoming a maximum with sample *D*.

We observe from Figs. 4.4(a)-(d) that the Y-211 particles are fine, spherical and distributed uniformly in the samples *A*, *C* and *D* whereas in the case of sample *B* where Ag was introduced through the preform, the distribution of the particles is non-uniform. We also observe that the Y-211 size refines with increasing silver content, when silver is introduced through the liquid phase source. In histograms of the Figs. 4.5(a)-(b), we compare the distribution of Y-211 size in the samples *A*, *B*, *C* and *D* respectively. We observe that Y-211 particle size distribution remains narrow (< 3 μm) in the case of sample *A* without Ag and also in samples *C* and *D* where Ag is introduced through the liquid phases. The size distribution of Y-211 is broader (in the range 1 - 8 μm) when Ag is introduced directly into the preform as can be seen from Fig. 4.5(b).
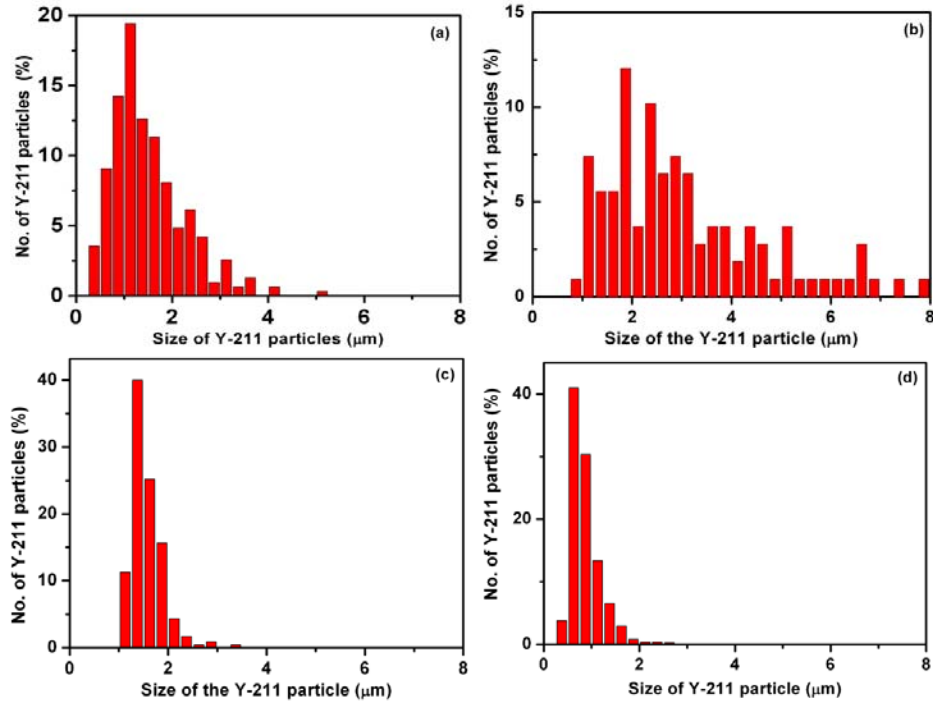
98

Fig. 4.5   Histograms are constructed showing the number of Y-211 particles in different size ranges versus the average size of such particles in each range. The histograms were constructed using the micrographs in Fig. 4.4. Figs. (a), (b), (c) and (d) are for the Samples A, B, C and D respectively.

4.3.2   Effect of Ag on the macro-defects

In Fig. 4.6, the effect of introducing Ag along with the liquid phases is compared with the case where Ag is introduced into the preform directly. In Figs. 4.6(a), (b) and (c), we compare relatively low magnification micrographs from samples *B*, *C* and *D*. We note that the Ag particles are coarse (10 to 100 μm) in Sample *B* where Ag is introduced in the preform, and refined in Samples *C* (2 to 25 μm) and *D* (2 to 5 μm), where Ag is introduced through the liquid phases. The silver particles are very fine, large in number and uniformly distributed in Sample *D*, and have the effect of closing macro-cracks by filling them up. This is unlike in sample *B* where the Ag particles are large and far apart and has not much effect in closing the cracks.
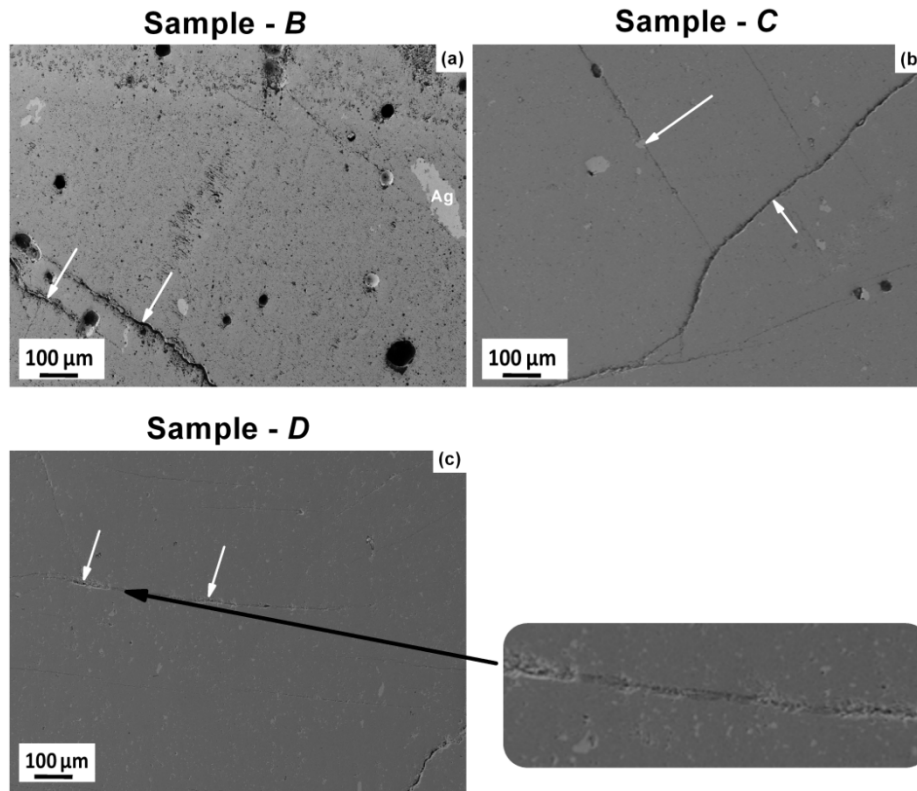
Fig. 4.6. Macro-cracks observed in the samples *B C* and *D* are shown; (a) in Sample *B* with large and non-uniformly distributed Ag particles, the cracks remain open. (b) We observe that the cracks are closed to some extent in Sample *C* with 10% Ag introduced through the liquid phase source. (c) In Sample *D*, the cracks are closed by fine and uniformly distributed Ag particles which enter the cracks. The entry of Ag particles into cracks was confirmed by EDS/WDS. Arrows marked in the figure indicate the positions in the samples where Ag was detected. A magnified image comprising of a macrocrack region in Sample D is shown as an inset which clearly shows the entry of Ag particles into the cracks aiding the fusing of the cracks.

Energy Dispersive spectrometry (EDS) and Wavelength Dispersive spectrometry (WDS) were employed to examine the presence of Ag particles in the macro-crack regions of samples *B* and *D.* No trace of Ag particles was found in the cracks in sample *B* whereas Ag particles were seen in the cracks in samples *C* and *D* as detected by EDS. Figs. 4.6(b) and (c) show that the refinement of Ag particles and the closure of the cracks improve gradually with Ag content. This confirms that Ag when added along with the liquid phases aids in fusing the macro-cracks significantly.

4.3.3 Spatial homogeneity in the distribution of Y-211 and Ag particles in YBCO/Ag composites

In order to investigate the homogeneity in the microstructures across the sample, we show the FE-SEM images obtained from sample *D* in Fig. 4.7 from a region near the seed crystal (P) and from a region far from the seed crystal (S). The locations of the regions P and S are provided in Fig. 4.3(a)
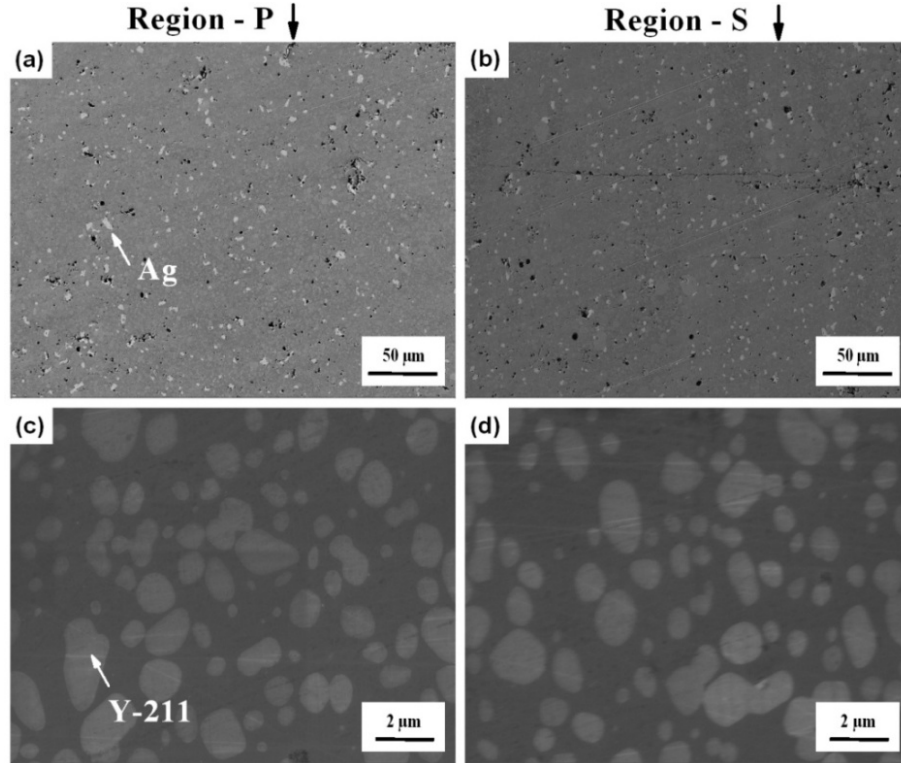
Fig. 4.7. (a) and (b) show FE-SEM secondary electron images obtained from regions P and S (see figure 3(a)) respectively of sample *D* with 20 wt.% Ag added with the liquid phases. (c) and (d) show high magnification images from the same regions using the in-lens detection mode. The micrographs demonstrate the homogeneity in the distribution of Ag and Y-211 particles over the volume of the sample.

Figs. 4.7(a) and (b) show the secondary electron images, in the regions P and S, in which all the silver particles are seen to be less than 5 microns in size and their distribution are similar and uniform. In Figs. 4.7(c) and (d), we show the 'in-lens' images from sample *D*, from the regions P and S, showing the size and distribution

of Y-211 particles to be similar in both the regions. The maximum variation in volume fraction of Y-211, over the sample volume, is ~ 3 %. The size of the Y-211 particles remained uniformly the same (in the range ~ 0.25 – 2 μm) across the volume of the sample.

4.4 Field dependence of critical current densities

The field dependence of current density, $J_c(H)$, for samples *A, B, C* and *D* obtained at 50 K and 77 K are shown in Figs. 4.8(a) and (b) respectively.
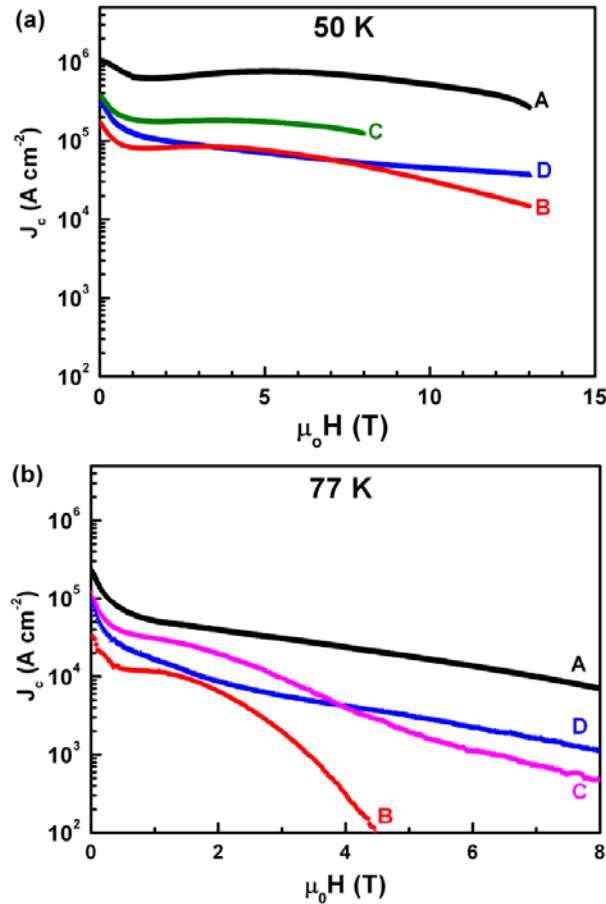
Fig. 4.8. Magnetic field dependence of critical current density (J_c) in samples *A, B, C* and D at (a) 50 K and at (b) 77 K. The POIGP samples are observed to exhibit a nearly flat response in their J_c versus H curves up to 13 Tesla at 50 K; the response for sample C is shown only up to 8 Tesla. At 77 K, sample B with Ag introduced through the preform, shows rapid reduction in J_c beyond 2 T while the deterioration in J_c of samples A, C and D is relatively small up to 8 T. Samples A, C and D exhibit zero field J_c of 19.2 kAcm^{-2}, 10 kAcm^{-2} and 7.1 kAcm^{-2} respectively at 77 K.

It is evident from Fig. 4.8(a) that all the POIGP samples show nearly flat $J_c(H)$ response to 13 Tesla at 50 K. At 77 K, as observed from Fig. 4.8(b), sample B shows a rapid reduction in J_c beyond 2 T while the deterioration in J_c of samples C and D is relatively small up to 8 T. Samples C and D exhibit zero field J_c of 10 kAcm^{-2} and 7.1 kAcm^{-2} respectively at 77 K. These samples maintained J_c in excess of 10^3 Acm^{-2} up to fields of 2.7 T at 77 K, exceeding the performance reported for YBCO/Ag composites with no nano-dopants or refiners in the literature so far [18-25]. The fact that the J_c remained better than 100 Acm^{-2} to high fields indicates that irreversibility fields are more than 7 T at 77 K for the samples A and D. This suggests that the magnetic flux pinning is operative in the YBCO and YBCO/Ag samples even at such high fields.

It is noteworthy that though the performance of the Ag-containing POIGP samples (B, C and D) is superior to silver containing samples with no added refiners / dopants reported in literature, their $J_c(H)$ is low in comparison with the Ag-free sample (A). We note that J_c of all the samples, including sample B with inferior microstructure, is nearly independent of magnetic field up to very high fields at 50 K. This suggests that a field independent flux pinning mechanism, such as from structural defects, is operative.

The possible reasons for obtaining high current densities to high applied fields are explored and the possible sources are discussed in Chapter VI.

References

[1]   Mendoza E, Puig T, Varesi E, Carrillo A E, Plain J and Obradors X 2000 *Physica C* **334** 7

[2]   Diko P, Krabbes G and Wende C 2001 *Supercond. Sci. Technol.* **14** 486

[3]   Maeda J, Izumi T and Shiohara Y 1999 *Supercond. Sci. Technol.* **12** 232

[4]   Iida K, Hari Babu N and Cardwell D A 2007 *Supercond. Sci. Technol.* **20** 1065

[5]   Foerster C E, Lima E, Rodrigues Jr P, Serbena F C, Lepienski C M, Cantão M P, Jurelo A R and Obradors X 2008 *Braz. J. Phys.* **38** 341

[6]   Fujimoto H 2009 *IEEE Trans. Appl. Supercond.* **19** 2933

[7]   Joo J, Kim J-G and Nah W 1998 *Supercond. Sci. Technol.* **11** 645

[8]   Hari Babu N, Iida K, Briffa A, Shi Y-H, Matthews L S and Cardwell D A 2007 *IEEE Trans. Appl. Supercond.* **17** 2953

[9]   Gopalan R, Roy T, Rajasekharan T, Rangarajan G and Hari Babu N 1995 *Physica C* **244** 106

[10]   Lee D F, Chaud X and Salama K 1991 *Physica C* **181** 81

[11]   Hsu S-H, Chen I-G and Wu M-K 2002 *Supercond. Sci. Technol.* **15** 653

[12]   Mori N, Dateki K, Hirao T and Ogi K 2006 *Physica C* **445–448** 308

[13]   Iida K, Hari Babu N, Shi Y-H, Miyazaki T, Sakai N, Murakami M and Cardwell D A 2008 *J. Phys.* **97** 012105

[14]   Iida K, Hari Babu N, Shi Y, Pathak S K, Yeoh W K, Miyazaki T, Sakai N, Murakami M and Cardwell D A 2008 *Physica C* **468** 1387

[15]   Sudhakar Reddy E, Sastry T V R K and Rajasekharan T 1999 *Mater. Lett.* **38** 62

[16]   Goyal A, Funkenbusch P D, Kroeger D M and Burns S J 1991 *Physica C* **182** 203

[17]   Sudhakar Reddy E and Rajasekharan T 1999 *J. Mater. Sci.* **34** 3755

[18] Deng Z, Zheng J, Li J, Ma G, Lu Y, Zhang Y, Wang S and Wang J 2008 *Mater. Sci. Eng. B* **151** 117

[19] Chu W K, Ma K B, McMichael C K and Lamb M A 1993 *Appl. Supercond.* **1** 1259

[20] Sudhakar Reddy E and Rajasekharan T 1998 *Supercond. Sci. Technol.* **11** 523

[21] Viswanath N V N, Rajasekharan T, Harish Kumar N, Menon L and Malik S K 1998 *Supercond. Sci. Technol.* **11** 420

[22] Sudhakar Reddy E and Rajasekharan T 1998 *J. Mater. Res.* **13** 2472

[23] Hari Babu N, Rajasekharan T, Latika Menon and Malik S K 1999 *J. Am. Ceram. Soc.* **82** 2978

[24] Hari Babu N, Kambara M, Smith P J, Cardwell D A and Shi Y 2000 *J. Mater. Res.* **15** 1235

[25] Meslin S, Iida K, Hari Babu N, Cardwell D A and Noudem J G 2006 *Supercond. Sci. Technol.* **19** 711

CHAPTER V

MICROSTRUCTURAL AND MAGNETIC PROPERTIES OF Y-Ba-Cu-O SUPERCONDUCTORS FABRICATED BY INTEGRATION OF DIRECTIONAL SOLIDIFICATION WITH POIGP

5.1. Advantages of Directional Solidification (DS) and its combination with POIGP

5.1.1 Directional Solidification

Directional Solidification (DS) is a process that promotes single crystalline / textured growth in materials. This process has been adapted [1-3] to fabricate textured REBCO products and it has an additional advantage of enabling fabrication in relatively short time durations. Bridgman growth involves heating a material (Y-123, in the present case) above its melting point and its consequent solidification at a defined growth rate in a temperature gradient. Directional solidification, if optimized, is attractive for the fabrication of high temperature superconducting REBCO wires [4]. Hence attempts to optimize this technique to obtain suitable microstructures that can support large currents at 77 K is important from applications point of view.

5.1.2 Directional Solidification with MG process

The Melt Growth (MG) process and its various derivatives which led to high critical current densities (J_c), and the fact that the process is usually accompanied by macro-defects in the samples prepared by them have been discussed in detail in Chapter I. To retain the advantages of directional solidification [1-3] that enables the fabrication of textured REBCO products in relatively short time durations, combining DS with MG process was attempted by many groups [5-13]. Bridgman growth of Y-123 was widely investigated and it was shown that the maximum growth rate allowing single-domain samples to be reached is about 3 mmh^{-1} [10]. Nakamura et al. [5] reported that the crystal gets textured along the growth

direction in the DS-MG method. They studied the effect of pulling rate on the texture and on the Y-211 content left over in the Y-123 matrix. Nd-123 superconductors prepared in air by Bridgman method [11] were shown to exhibit T_c of 95 K. However, the presence of major macro-defects (8 - 14 %) occurring in MG processed samples and its modified forms in combination with Directional Solidification (DS-MGP) remain a serious concern.

5.1.3 Directional Solidification with IG process

IG process yields refined Y-211 precipitates in the matrix of Y-123 [14-22] and additionally shows the ability to produce near-net shaped samples [14, 15] without the need for the addition of grain refining compounds like Pt, PtO_2 CeO_2 etc. [23-25]. However, it is also essential to optimize the distribution of fine sized Y-211 particles to achieve significant density of fine-sized defects that can cause flux pinning and thus enhance J_c up to high fields [26, 27]. Hao et al. [28, 29] have reported the fabrication of YBCO superconductors through directional solidification combined with IG process (DSIG). They have studied the effect of temperature gradient applied during IG process on the microstructural properties of the end products. Their samples showed both coarse and fine sized Y-211 particles. They also showed presence of considerable amount of macroscopic defects like porosity (∼ 7 - 13 %) and macro-cracks (∼ 15 %) in the end products. The magnitude of J_c was not reported in the work.

5.1.4. Importance of integrating POIGP with directional solidification

Our work on Preform Optimized IG process (POIGP) [30, 31] reported in Chapter III has shown that achieving mechanical stability of the Y-211 preforms prior to liquid phase infiltration is very important in the IG process to achieve minimal macro-defects in the end products. It is also shown that the preform compaction pressure need be optimized to achieve uniform distribution of Y-211 particles in Y-123 matrix. A compaction pressure of 460 MPa applied to Y-211

preform had yielded uniform microstructures with minimal macro defects (porosity < 0.2 %). In addition, the sample fabricated by POIGP showed critical current densities in excess of 25 kA cm^{-2} to 13 T at 50 K and to 1 kAcm^{-2} to magnetic fields of 6.5 T at 77K.

In this context, it appears that the presence of considerable macro-defects reported in the products made by DSIG [28, 29] could be due to the absence of using an optimal preform fabrication method prior to IG process. It is hence interesting to investigate the microstructures and the resultant current densities of DSIG samples fabricated after optimizing the preform fabrication process, and we refer to this as DS-POIG process.

5.2 Directionally Solidified Preform Optimized IG Process

We report, in this section, the details of the method developed by integrating POIGP with directional solidification. The effect of compaction pressure applied to the Y-211 preform prior to infiltration is investigated on the end microstructures. The resultant magnetic properties of the bulk YBCO samples fabricated by DS-POIGP are discussed. The field dependence of current densities, $J_c(H)$, are correlated to the microstructural features in various YBCO samples fabricated by DS-POIGP.

In order to fabricate samples by DS-POIGP, a vertical tubular muffle furnace, having a uniform hot-zone of ∼ 60 mm, was employed. The temperature of the furnace was monitored and regulated using a Eurotherm-make temperature controller (model 2404) and thyristor (model TE10A).

The sample assembly, used for POIGP and discussed in Section 2.1.1 of Chapter 2, is suspended in the vertical furnace using a platinum wire. A provision was made to move the sample assembly in a controlled manner through the hot zone of the furnace using a gear assembly driven by a dc motor. A schematic representation of the vertical furnace used for the fabrication of YBCO samples by

DS-POIGP is shown in Fig. 5.1(a). The temperature profile of the vertical furnace is provided in Fig. 5.1(b). The translation rate of the sample assembly in the furnace was ∼ 4 mm hr $^{-1}$.
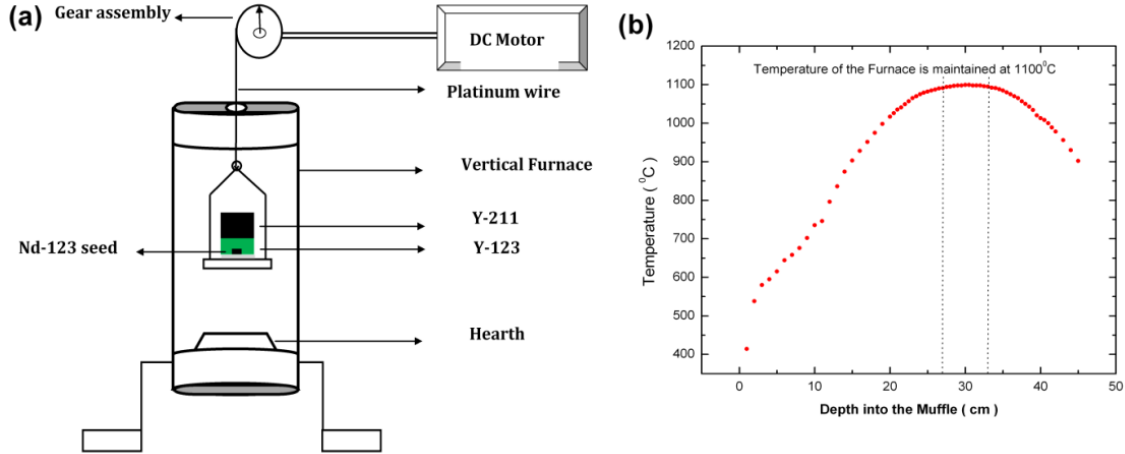
Fig. 5.1. (a) Schematic diagram of the vertical furnace employed for fabricating YBCO samples by DS-POIGP. (b) Temperature profile obtained in the vertical furnace.

Following the procedure discussed in Chapter III, in each of the present experiments, the sample assembly was pre-sintered at 950ºC for 4 hours prior to infiltration to improve the mechanical rigidity of the Y-211 preform. The temperature of the furnace was then ramped to 1100ºC and maintained there for 1 hour to ensure complete infiltration of the liquid phases (BaCuO$_2$ and CuO) into the pre-sintered Y-211 preform. The assembly was then lowered at the rate of 4 mm hr^{-1} through the hot zone. This process enabled fabrication of samples in a time duration of ∼ 30 hours. The samples thus obtained were oxygenated in a tubular furnace at 460ºC in flowing oxygen for 100 hours. These samples fabricated by DS-POIGP are, hereafter, referred to as DS-380, DS-460 and DS-540 with the numbers representing the preform compaction pressure (in MPa).

5.3 Effect of compaction pressure on the properties of DS-POIG processed samples

5.3.1 ac susceptibility

The temperature dependences of the in-phase component of ac susceptibility (χ') obtained for the YBCO samples fabricated by DS-POIGP are shown in Fig. 5.2.
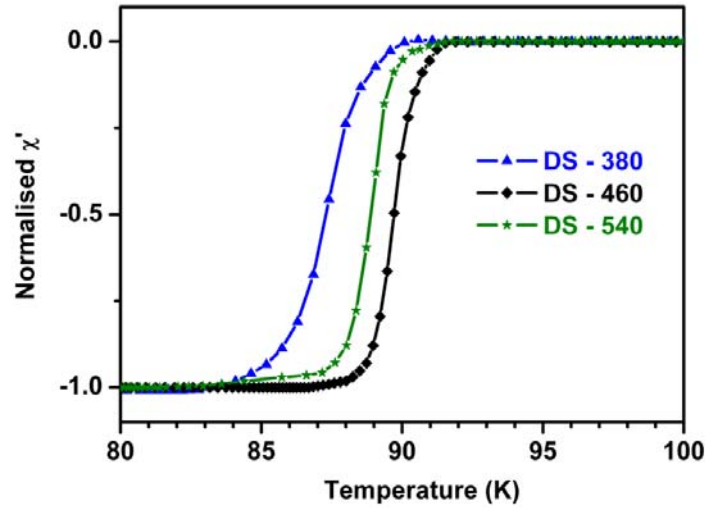
Fig. 5.2. Temperature dependence of in-phase component of ac susceptibility of the YBCO samples (DS-380, DS-460 and DS-540) fabricated by DS-POIGP.

It is evident from the figure that the samples DS-460 and DS-540 show sharp superconducting transitions indicating that there are no major low T_c phases in the sample. However, a relatively broad transition (with width $\sim$ 4°C) was observed in sample DS-380. The broadness of the transition indicates the presence of some oxygen-deficient regions in DS-380. FE-SEM images obtained from all the DS-POIGP samples under low magnification (250 x) using a secondary electron (SE) detector are shown in Fig. 5.3
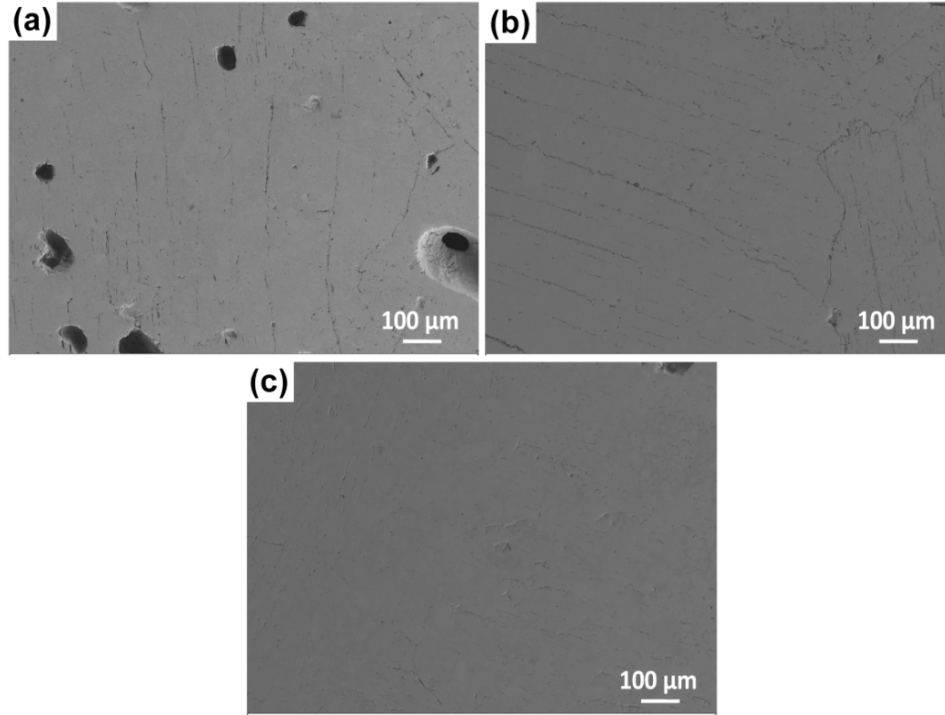
Fig. 5.3. FE-SEM images obtained under low magnification of 250 x from the samples DS-380, DS-460 and DS-540 fabricated by DS-POIGP are shown in (a), (b) and (c) respectively

The micrographs shown as (a), (b) and (c) in Fig. 5.3 correspond to the samples DS-380, DS-460 and DS-540 respectively. It is found that with an increase in the compaction pressure, the pore size and the porosity have reduced significantly. The macro-crack fraction and crack widths are also found to decrease with increasing preform compaction pressure. The data is summarized in table 5.1.

FE-SEM images obtained from the samples DS-380, DS-460 and DS-540, under a magnification of 1000 x using in-lens detector, are shown in Figs. 5.4(a), (b) and (c) respectively and the corresponding histograms indicating the contribution of Y-211 particles to the effective surface area are shown in Figs. 5(d), (e) and (f). The percentage fraction of number of Y-211 particles with size less than 2 μm is found to be maximum (>75%) for the sample DS-460. In the other two samples DS-380 and DS-540, many coarse (> 6 μm) Y-211 particles are found to exist accounting for the larger content of Y-211 content seen in table 5.1.

112
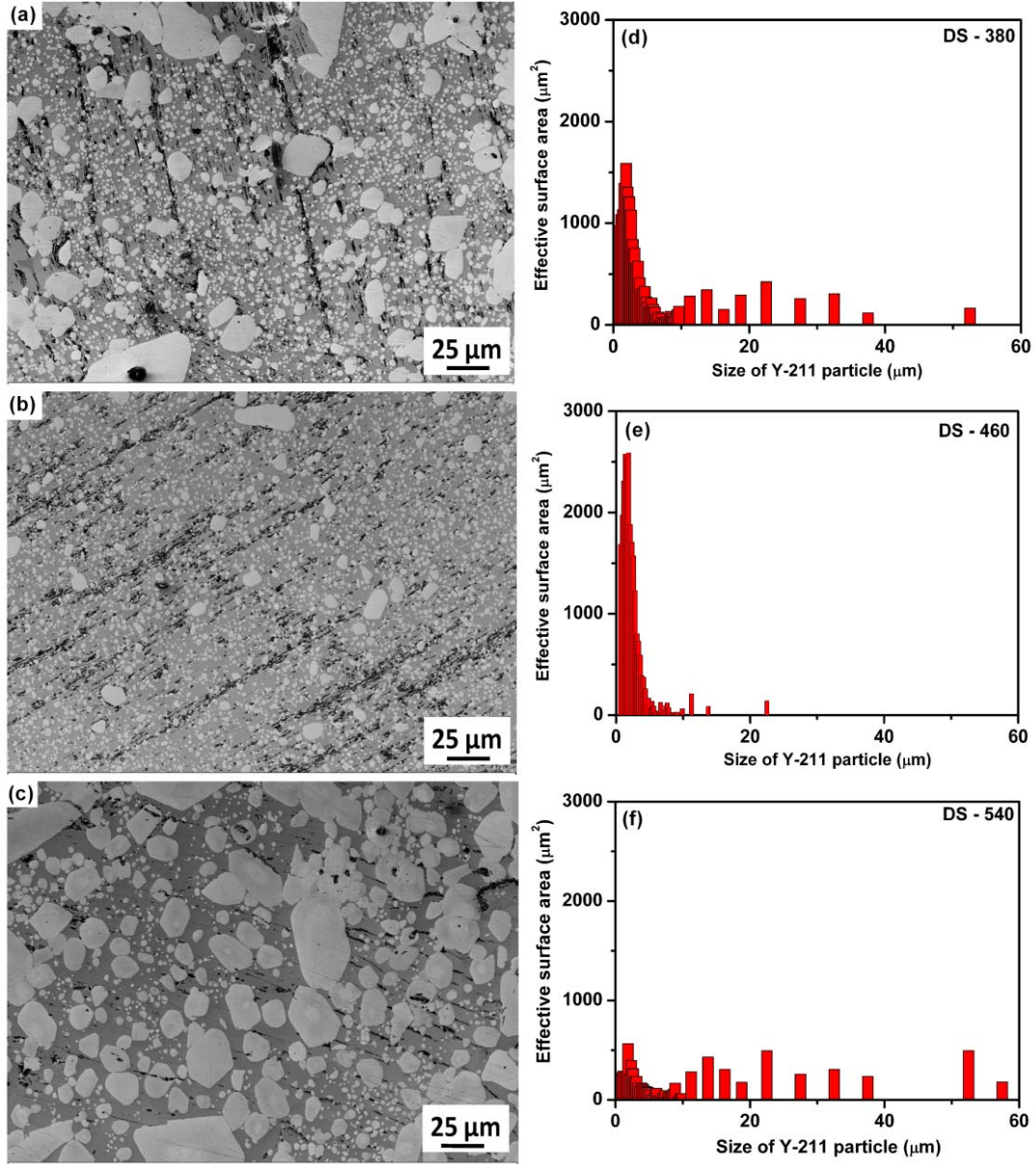
Fig. 5.4. (a), (b) and (c) show FE-SEM images obtained under a magnification of 1000 x from the samples DS-380, DS-460 and DS-540 respectively. (d) – (f) The histograms represent the contribution of different sized Y-211 particles to the effective surface area.

The total surface area of Y-211 particles is a measure of interface area and of the structural defects that cause flux pinning originating from the Y-211/Y-123 interfaces [32, 33]. Figs. 5.4(d)–(f) show the variation in the surface area of the Y-211 particles of different sizes from which it is evident that most of the surface area

contribution in sample DS-460 arises from very fine Y-211 particles. In contrast to this, the effective surface area contributed by the particles of very large size (>6 μm) is comparable to that contributed by the small sized Y-211 particles in samples DS-380 and DS-540.

Table 5.1. Comparison of various microstructural properties of YBCO superconductors fabricated by DS-POIGP

Sample	DS - 380	DS - 460	DS - 540
Compaction pressure used during the fabrication of Y-211 preforms	380 MPa	460 MPa	540 MPa
Size of pores /voids (μm)	10 – 50 μm	1 - 4 μm	1 - 4 μm
Porosity (%)	5.2 %	0.6 %	0.2 %
Size range of macro-crack widths (μm)	< 6 μm	< 6 μm	< 6 μm
Macro-crack fraction (%)	4 %	0.8 %	0.9 %
Distribution of Y-211 particles	Non-Uniform	Uniform	Non-Uniform
Size range of Y-211 particles (μm)	Sub-micron – 40 μm	Sub-micron – 15 μm	Sub-micron – 60 μm
Size range of the majority of the Y-211 particles	1 - 4 μm	0.5 – 2 μm	0.5 – 4 μm
Average content of the Y-211 particles	37.4 %	31.6 %	41.9 %

5.4. Critical current densities and their field dependence

The field dependence of current density, $J_c(H)$ obtained in the samples DS-380, DS-460 and DS-540 at 50 K and 77 K are shown in Figs. 5.5(a) and (b) respectively. It is evident from Fig. 5.5(a) that DS-460 shows the best performance with nearly flat $J_c(H)$ of about 10 kA cm^{-2} to 12 Tesla at 50 K and a zero field J_c of 10 kAcm^{-2} at 77K. The irreversibility field (at which J_c is in excess of 100 Acm^{-2} [34]) is

higher than 6 Tesla even at 77 K and is better than the ones reported in literature [17, 21, 35, 36] for YBCO superconductors fabricated, following long heat treatments of ~ 120 hours duration with no added nano-dopants / grain refiners. The $J_c(H)$ and the irreversibility field of DS-380 and DS-540 samples are comparable to the reported values. It is interesting to observe that the J_c is high to very high fields for samples compacted at 460 MPa in DS-POIGP, just as for the samples processed through long heat treatments without Ag (discussed in Chapter III) and with Ag (discussed in Chapter IV).
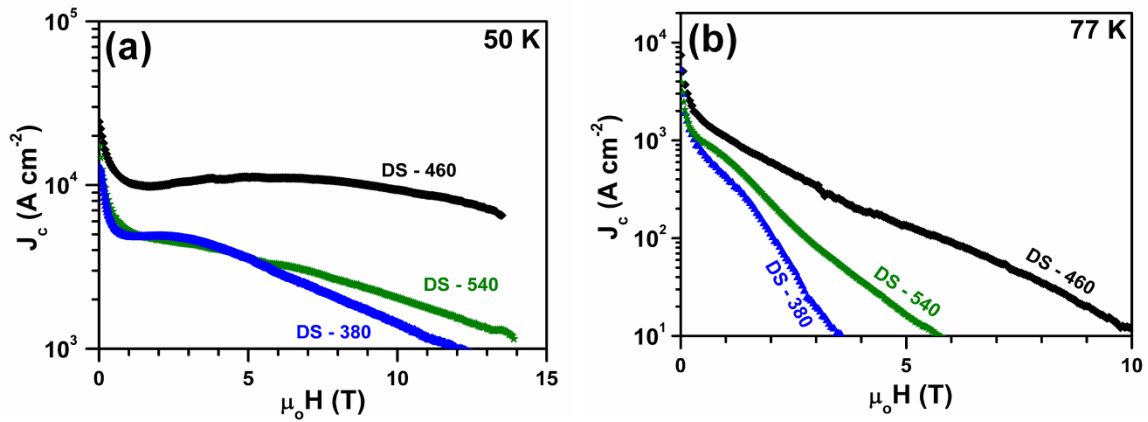
Fig. 5.5. $J_c(H)$ at (a) 50 K and (b) 77 K of samples whose Y-211 preforms were fabricated at different pressures between 380 MPa and 540 MPa are shown. It can be observed that the all the samples (DS-380 to DS-540) show significantly high J_c up to high applied magnetic fields at 50 K. Among the samples under study, the $J_c(H)$ for the sample DS-460 is seen to be superior with magnitude of J_c better than 10^2 Acm^{-2} up to 6 Tesla at 77 K.

In order to investigate the nature of pinning in the DS-POIGP samples, the flux pinning force (F_p) defined as

$$F_p = J_c \times \mu_0 H \ldots\ldots\ldots\ldots(3)$$

is computed for each of the samples both at 50 K and 77 K. F_p is normalized to the corresponding maximum value for each of the samples and is denoted as $F_p / F_{p.max.}$. The normalized flux pinning force is plotted as a function of applied field for all the samples at 50 K and 77 K, which are shown in Figs. 5.6(a) and (b) respectively.
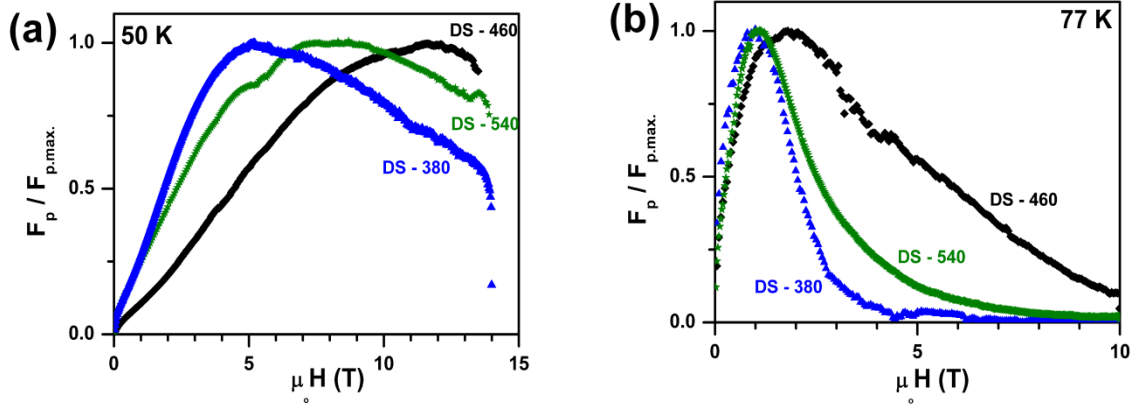
Fig. 5.6. The field dependences of the normalized flux pinning force F_p / $F_{p.max.}$ for the samples DS-380, DS-460 and DS-540 at (a) 50 K and (b) 77 K are shown. The curve for sample DS-460 showed a peak at a field of 12 T at 50 K and 1.9 T at 77 K indicating the superior pinning ability.

It can be observed from the figure that among the present samples, DS-460 sample exhibits the largest flux pinning to higher fields peaking at 1.9 T at 77 K and at ~ 12 T at 50 K. It is thus evident that the Y-211 preforms made under optimum compaction pressure (460 MPa) when processed by DS-POIGP is capable of providing uniform distribution of Y-211 particles in the matrix of Y-123 and facilitating large irreversibility fields of 6 T at 77 K.

5.5. Addition of Ag in YBCO sample fabricated by DS-POIGP

5.5.1 Necessity for addition of Ag

A comparison of microstructural features observed in DS-460 {Fig. 5.4(b)} with those of S-460 {Fig. 3.6(g) of Chapter III} fabricated by long heat treatment reveals the following aspects. We observe that the distribution of Y-211 particles is centered around 1 μm in S-460 while it is around 2 μm in DS-460 with conspicuous absence of Y-211 particles of less than 500 nm size. The porosity levels were smaller (~ 0.2%) in S-460 compared to those (~ 0.6%) in DS-460. The average distance between the macro-cracks is more (~260 μm) in S-460 compared to that (~ 70 μm) in DS-460. With an aim to improve the microstructural features observed in DS-460 which are inferior to those of S-460, the effect of Ag addition to DS-460 has been investigated.

The earlier investigations on YBCO/Ag composites through long heat treatments presented in Chapter IV showed that 20 wt.% of Ag introduced along with the liquid phases yields the best results in terms of generating microstructures supporting enhanced $J_c(H)$. Hence we added 20 wt.% Ag along with liquid phases while fabricating of YBCO/Ag sample by DS-POIGP.

5.5.2 Fabrication of YBCO/Ag sample by DS-POIGP

In order to fabricate YBCO/Ag sample by DS-POIGP, a Y-123 pellet containing 20 wt. % of Ag (compared to the weight of Y-211 preform) was prepared and was used as a source of liquid phases. The arrangement of pellets and the heat treatment followed are similar to that followed for DS-POIGP as discussed in Section 5.2. The resulting sample was oxygenated by heating the sample at 460°C in flowing oxygen for about 100 hours. This sample is hereafter referred to as DS-460-Ag20.

5.5.3 Microstructures of DS-460-Ag20 composite

The secondary electron and in-lens FE-SEM images obtained from the sample DS-460-Ag20 are shown in Figs. 5.7(a) and (b) respectively.
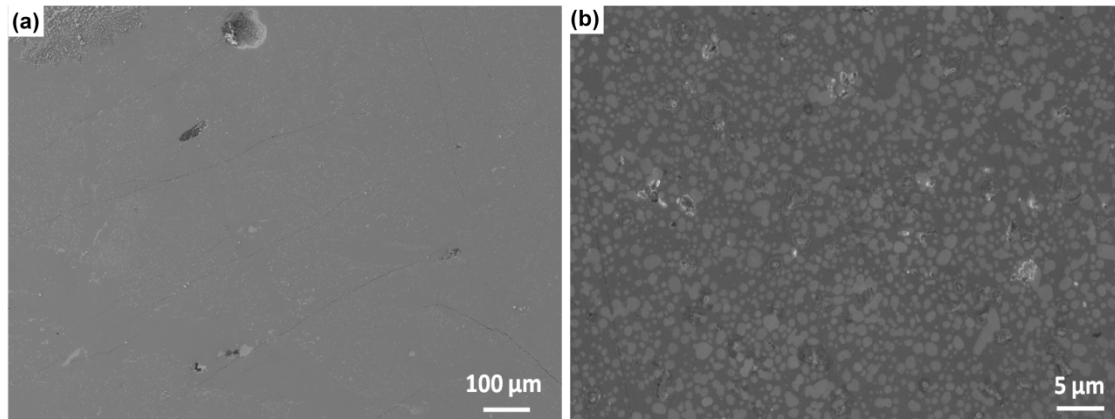
Fig. 5.7. (a) The Secondary electron and (b) in-lens image obtained from YBCO/Ag sample fabricated by DS-POIGP are shown. In (a), it can be seen that the sample is largely free macro-pores; Ag has fused the macro-cracks. In (b), we see that Ag also aided in refining the Y-211 particles in comparison with Ag-free samples prepared under similar conditions {see Fig. 5.4(b)}.

It is evident from Fig. 5.7(a), that the macro-cracks that formed in the Ag-free sample (DS-460) were successfully fused with addition of Ag increasing the average distance between the macro-cracks to 170 μm. The sample was also found to be free from porosity (< 0.2%). The uniform distribution of fine-sized Y-211 particles in the matrix of Y-123 can be seen in Fig. 5.7(b). The histogram made for the YBCO/Ag sample (DS-460-Ag20), showing the distribution of Y-211 particles, is shown in comparison with that of the Ag-free sample in Fig. 5.8.
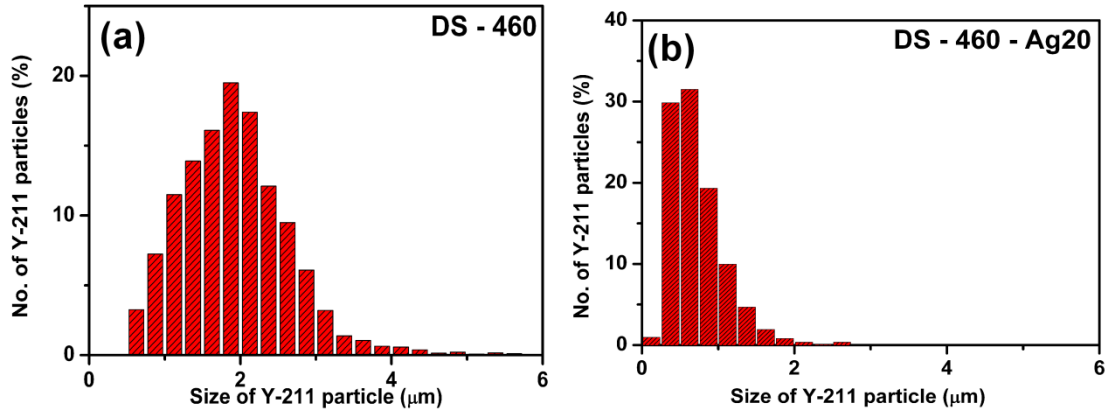
Fig. 5.8. Histograms showing the size distribution of Y-211 particles in (a) Ag-free YBCO sample 'DS-460' and (b) Ag-added YBCO sample 'DS-460-Ag20'

The addition of Ag has refined the size of Y-211 particles with its distribution centered around 0.75 μm in comparison with 2 μm sized particles present in the Ag-free samples fabricated by DS-POIGP. Additionally, very fine particles, < 0.5 μm, are also seen in the Ag-added sample.

Fig. 5.9 shows the secondary electron micrograph obtained from the sample DS-460-Ag20. The figure shows that the Ag particles are uniformly distributed in the end product and are in the size range 1 – 4 μm.
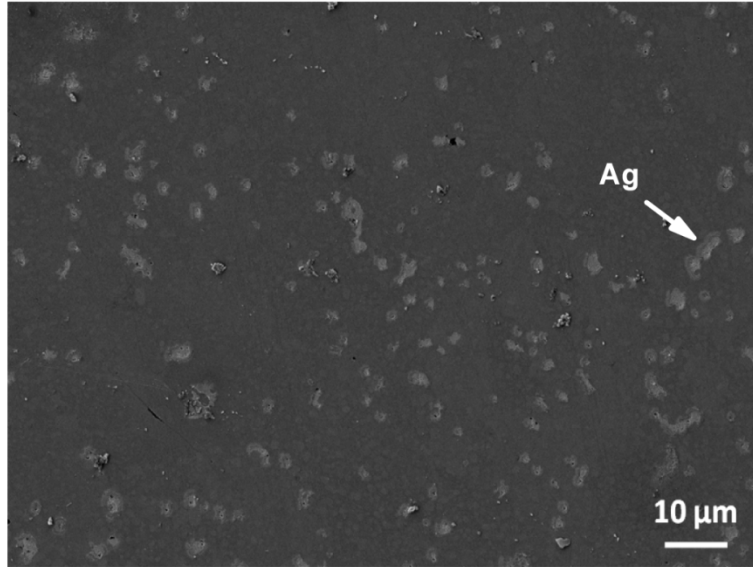
Fig. 5.9. Secondary electron micrograph obtained from the YBCO/Ag composite (DS-460-Ag20) indicating the distribution of Ag particles in the matrix of Y-123.

5.5.4 Field dependence of J_c of the YBCO/Ag composite (DS-460-Ag20)

The field dependence of current densities obtained in the DS-460-Ag20 sample at 77 K is compared in Fig. 5.10 with that of Ag-free sample (DS-460).
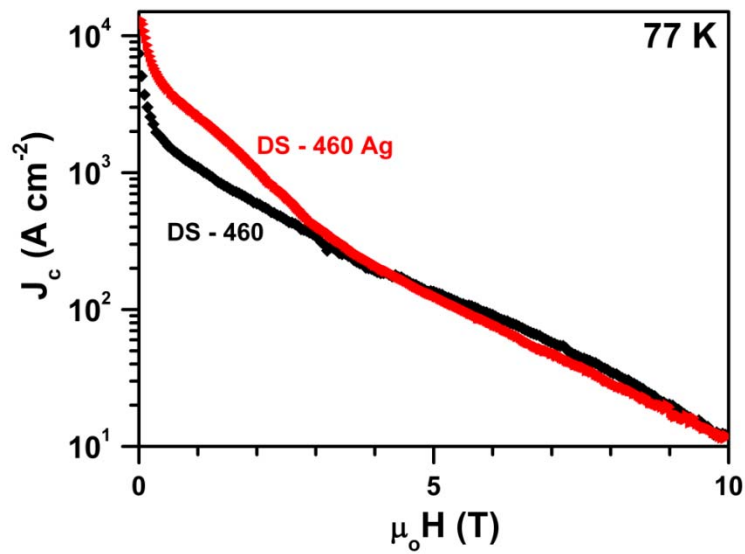
Fig. 5.10. Field dependence of J_c at 77 K for YBCO/Ag sample (DS-460-Ag20) in comparison with Ag-free sample (DS-460)

It can be observed from Fig. 5.10 that $J_c(H)$ of the YBCO/Ag composite showed a visible improvement over the Ag-free sample in the low-field region (< 3 Tesla). The performance of both the samples is nearly the same at high field region (> 3 Tesla). We attribute the enhancement in $J_c(H)$ at low fields to the improved microstructural features discussed above and the associated rise in surface area of Y-211 particles which cause an effective increase in the interfacial defect density.

References

[1]   Izumi T, Nakamura Y and Shiohara Y 1991 *Adv. Supercond.* **5** 429

[2]   Cima M J, Flemmings M C, Figueredo A M, Nakade M, Ishii H, Brody H D and Haggerty J S 1992 *J. Appl. Phys.* **71** 1868

[3]   Selvamanickam V, Goyal A and Kroeger D M 1994 J. Electronic Materials. **23** 1169

[4]   Mcginn P J, Chen W and Black M A 1989 *Physica C* **161** 198

[5]   Nakamura Y, Ooishi Y, Kato K, Inada R and Oota A 2007 *IEEE Trans. Appl. Supercond.* **17** 2988

[6]   Salama K and Selvamanickam V 1992 *Supercond. Sci. Technol.* **5** S85

[7]   Monot I, Lepropre M, Provost J, Desgardin G, Raveau B, Bourgault D, Barbut J M, Braithwaite D and Tournier R 1992 *Ibid.* **5** 712

[8]   No K, Yoon D, Shin W S, Kim W and Shim G 1994 *J. Mater. Sci.* **29** 2345

[9]   Lapin J, Dierickx D, Rosseel K and Ryelandt L 1998 *J. Mater. Sci. Lett.* **18** 611

[10]   Selvamanickam V, Partsinevelos C, Mc Guire A V and Salama K 1992 *Appl. Phys. Lett.* **60** 3313

[11]   Salama K, Parikh A S and Woolf L 1996 *Appl. Phys. Lett.* **68** 1993

[12]   Sumida M, Nakamura Y, Shiohara Y and Umeda T 1997 *J. Mater. Res.* **12** 1979

[13]   Obradors X, Yu R, Sandiumenge F, Martinez B, Vilalta N, Gomis V, Puig T and Piňol S 1997 *Supercond. Sci. Technol.* **10** 884

[14]   Sudhakar Reddy E and Rajasekharan T 1998 *Supercond. Sci. Technol.* **11** 523

[15]   Sudhakar Reddy E and Rajasekharan T 1998 *J. Mater. Res.* **13** 2472

[16]   Hari Babu N, Rajasekharan T, Latika Menon and Malik S K 1999 *J. Am. Ceram. Soc.* **82** 2978

[17] Viswanath N V N, Rajasekharan T, Harish Kumar N, Menon L and Malik S K 1998 *Supercond. Sci. Technol.* **11** 420

[18] Chen Y L, Chan H M, Harmer M P, Todt V R, Sengupta S and Shi D 1994 *Physica C* **234** 232

[19] Meslin S, Iida K, Hari Babu N, Cardwell D A and Noudem J G 2006 *Supercond. Sci. Technol.* **19** 711

[20] Iida K, Hari Babu N, Withnell T D, Shi Y, Haindl S, Weber H W and Cardwell D A 2006 *Physica C* **445–448** 277

[21] Chen S-Y, Hsiao Y-S, Chen C-L, Yan D-C, Chen I-G and Wu M-K 2008 *Mater. Sci. Eng. B* **151** 31

[22] Meslin S and Noudem J G 2004 *Supercond. Sci. Technol.* **17** 1324

[23] Muralidhar M, Jisra M, Nariki S and Murakami M 2001 *Supercond. Sci. Technol.* **14** 832

[24] Diko P, ˇSefčíková M, Kaňuchová M and Zmorayová K 2008 *Mater. Sci. Eng. B* **151** 7

[25] Vilalta N, Sandiumenge F, Piňol S and Obradors X 1997 *J. Mater. Res.* **12** 38

[26] Cloots R, Koutzarova T, Mathieu J-P and Ausloos M 2005 *Supercond. Sci. Technol.* **18** R9

[27] Leblond C, Monot I, Provost J and Desgardin G 1999 *Physica C* **311** 211

[28] Hao D, Rui H, Jinshan L, Hongchao K, Xiangyi X, Hui C, Haitao C and Lian Z 2008 *Trans. Nonferrous Met. Soc. China* **18** 1139

[29] Rui H, Hao D, Jinshan L, Hongchao K, Xiangyi X, Hui C, Haitao C and Lian Z 2008 *Rare Metal Materials and Engineering* **37** 0854

[30] Devendra Kumar N, Rajasekharan T, Muraleedharan K, Banerjee A and Seshubai V 2010 *Supercond. Sci. Technol.* **23** 105020

[31] Devendra Kumar N, Rajasekharan T and Seshubai V 2011 *Supercond. Sci. Technol.* **24** 085005

[32] Salama K and Lee F Dominic 1994 *Supercond. Sci. Technol.* **7** 177

[33] Lee D F, Selvamanickam V and Salama K 1992 *Physica C* **202** 83

[34] Kobayashi S, Kaneko T, Kato T, Fujikami J and Sato K 1996 *Physica C* **258** 336

[35] Kim D-J and Kroeger D M 1993 *J. Mater. Sci.* **28** 4744

[36] Yeoh W K, Pathak S K, Shi Y-H, Dennis A R, Cardwell D A, Hari Babu N, Iida K and Strasik M 2009 *Supercond. Sci. Technol.* **22** 065011

[37] Hari Babu N, Iida K, Shi Y, Withnell T D and Cardwell D A 2006 *Supercond. Sci. Technol.* **19** S461

CHAPTER VI

ORIGIN OF FLUX PINNING LEADING TO ENHANCED CURRENT DENSITIES TO HIGH FIELDS: FURTHER INVESTIGATIONS

6.1.   Introduction

As discussed in Chapter III, preform optimization in IG process led to fabrication of YBCO samples with high critical current densities retained to very high applied fields even at 77 K. In samples fabricated from Y-211 preforms compacted under a uniaxial pressure of 460 MPa, a uniform distribution of fine sized Y-211 inclusions was obtained in the Y-123 matrix, with superior field dependence of J_c. The current densities were as high as 10^3 A cm^{-2} up to applied fields of 6.5 Tesla at 77 K. The fact that the improved performance was obtained through simple process modifications and that no additives are used to modify microstructures, provides a unique opportunity to identify the microstructural features responsible for enhanced flux pinning to very high magnetic fields. In this chapter, further investigations on the microstructural features of the optimized sample (S-460) using different techniques like TEM, EBSD and FE-SEM are reported. Correlations have been drawn between the microstructural features and field dependences of J_c from a comparative study of samples fabricated from preforms prepared under different compaction pressures. Possible mechanisms responsible for enhanced flux pining in the POIGP samples at high magnetic fields are discussed.

6.2. Field dependence of J_c at several temperatures

In Chapter III, we had pointed out that the best performance in the samples prepared by the Preform–Optimized IG process was obtained in the sample whose preform was fabricated under a uniaxial pressure of 460 MPa (the S-460 sample). *M-H* loops recorded in the optimized sample at 50 K and 65 K (up to magnetic fields of 14 Tesla), and at 77 K (up to 10 Tesla) are shown in Fig. 6.1
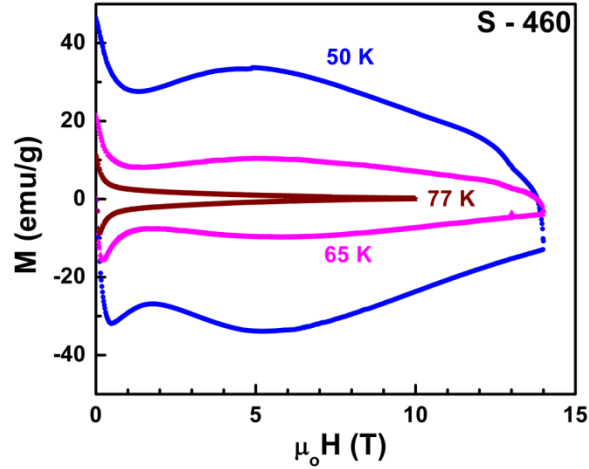
Fig. 6.1. Magnetic Hysteresis loops recorded at temperatures 50 K, 65 K and 77 K on a specimen from the sample S-460.

As discussed in Chapter 2.2.2., J_c was calculated following extended Bean's critical state model [1-3] using the formula

$$J_c = 20 \, \frac{\Delta M}{d} \ldots\ldots\ldots (6.1)$$

Here ΔM (in emu/cc) is the difference in the hysteretic magnetization between the curves obtained while increasing and decreasing the magnetic fields ($\Delta M = M^+ - M^-$) and $d \left[= b\left(1 - \dfrac{b}{3a}\right) \right]$ is the reduced dimension, where 'a' and 'b' are the planar dimensions (in cm) of the sample with a > b.
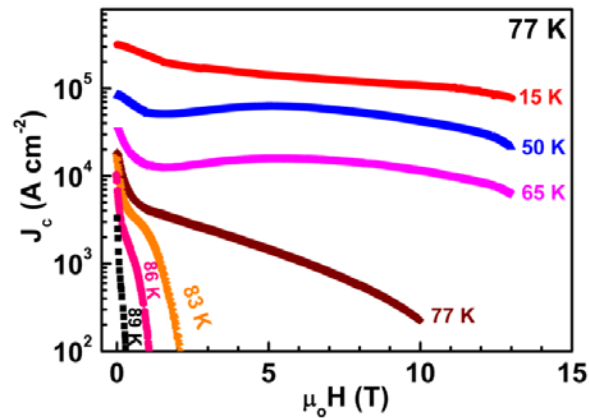
Fig. 6.2. J_c(H) for the sample S-460 in the temperature range 15 – 89 K. It can be seen that the sample shows irreversibility fields better than 10 T even at 77 K.

126

J_c obtained in the sample S-460 as function of magnetic field at several temperatures in the range 15 – 89 K, are shown in Fig. 6.2. It is evident from the figure that the sample shows a reasonably high value of zero field J_c of 19.2 kAcm^{-2} at 77 K and that it retains magnitudes of J_c in excess of 10^3 Acm^{-2} up to applied magnetic fields of 6.5 Tesla. The performance of the sample at 50 K and 65 K is also remarkable as the J_c remains well above 25 kAcm^{-2} up to magnetic fields of 13 Tesla, showing significant flux pinning active to high fields. From Figs. 6.1 and 6.2, one can observe a significant peak effect in the field dependence of J_c for the sample at 50 K and 65 K.

6.3. Temperature independent Peak field

The peak field H_p is defined as the field at which a second maximum [4, 5] occurs in the J_c versus H curve, or as the field at which a slope change [6] occurs in the J_c versus H curves. We have determined the peak fields in the sample S-460 as the field at which the J_c versus H curves exhibit a change of slope at different temperatures. An example demonstrating how the peak field was estimated is given in Fig. 6.3.
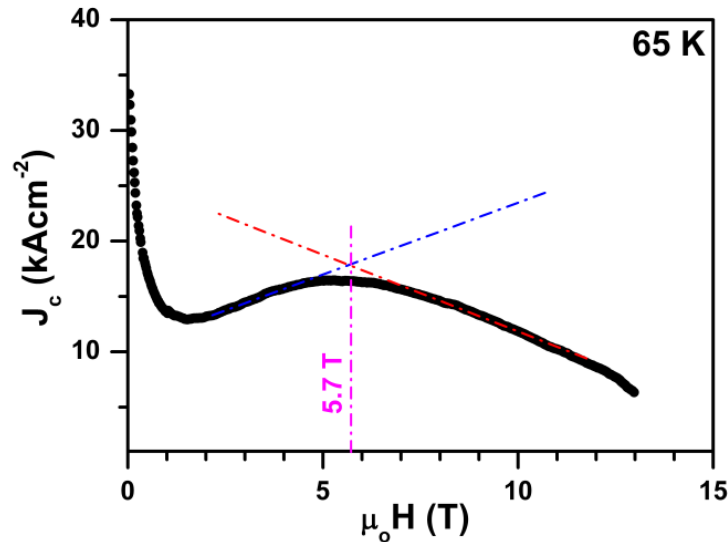
Fig. 6.3. Method of determining the peak field from J_c versus H curve is shown. The peak field H_p is determined as the field at which the slope change occurs in the J_c-H curve. A peak field of 5.7 Tesla is obtained for the sample S-460 at 65 K.

127

The variation in the peak field (H_p) as a function of temperature in the range 15 K to 89 K for the S-460 sample, is shown in Fig. 6.4.
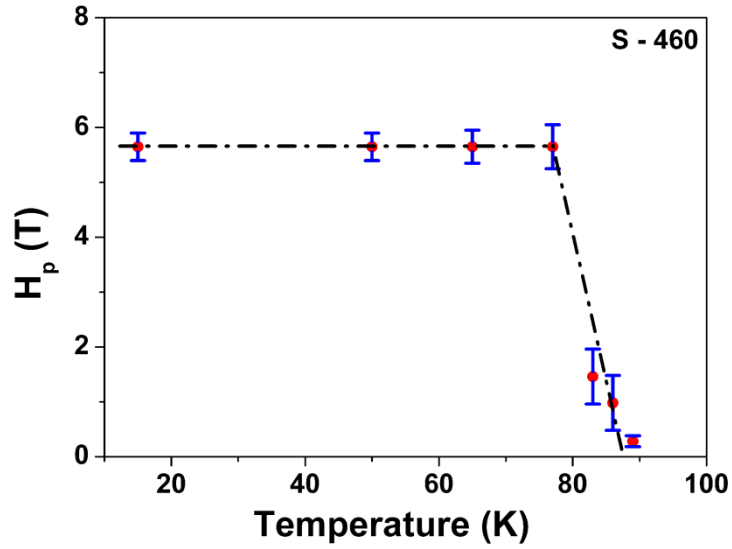
Fig. 6.4. The figure shows that the peak field H_p is temperature independent up to 77 K, and that it decreases rapidly above 77 K, close to T_c.

Fig. 6.4 shows that H_p is temperature independent in the temperature range below 77 K, and this suggests that one should look for structural defects, whose properties do not vary with temperature, as possible source of enhanced flux pinning below 77 K in the material. According to the equation [7] for peak field,

$$H_p = \frac{2\Phi_0}{\sqrt{3}a_f^2} \quad \text{.......... (6.2)}$$

where Φ_0 is the flux quantum and a_f is the vortex lattice spacing, the defect spacing in Y-123 matrix should vary in the range 50 nm to 15 nm to account for the observed enhanced flux pinning giving rise to an almost constant J_c, in a wide range (1 – 10 Tesla) of magnetic fields.

6.4 Nano-sized defects from TEM studies

The sample S-460 was studied using a Transmission Electron Microscope (TEM) to explore the possibility of finding finer defects of nanometer size in the

128

sample, as suggested by the Eq. 6.2. For this purpose, a thin section of the sample was sliced using a low speed saw and was dimple ground followed by ion milling in argon atmosphere as described in Section 2.2.2 of Chapter II. Finally, a focused ion beam was employed to extract a thin layer from the sample section for observation under TEM. An FEI-Quanta 3D dual beam system with an Omni Probe was used for the sample preparation. Bright field TEM images obtained from the sample are shown in Figs. 6.5(a) and (b). The indexed Selected Area Electron Diffraction (SAED) pattern obtained is shown in Fig. 6.6. The sample was identified as Y-123 from the diffraction pattern.
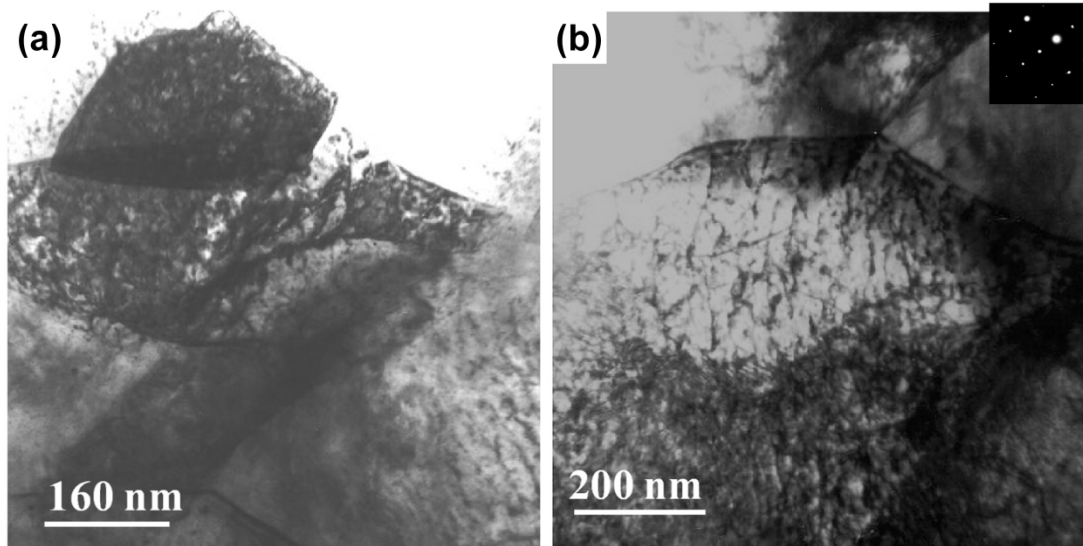
Fig. 6.5 (a), (b) Bright field images obtained by Transmission Electron Microscope in the sample S-460. TEM micrographs reveal the presence of fine defects separated by a few tens of nanometers within the domains in the Y-123 matrix. The defects within them appear to originate from the domain boundaries and to cover the complete volumes of the smaller domains. The SAED pattern obtained is shown as inset in (b)
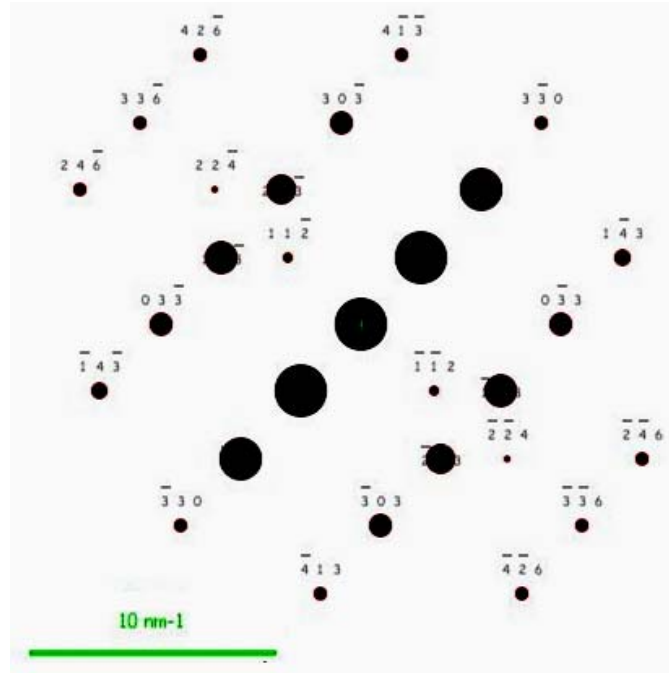
Fig. 6.6. Indexed Selected Area Electron Diffraction (SAED) pattern obtained from the sample S-460 is shown.

Fig. 6.5(a) shows presence of domain structure in the sample S-460. Domains of size ≈ 200 - 300 nm are seen within which a large number of fine defects separated by ∼ 15-50 nm are observed. The presence of these fine sized defects is shown in Fig. 6.5(b). These fine defects start at the domain boundaries, and are absent in areas away from the boundaries. Similar defects were reported in YBCO specimen processed under high oxygen pressure [8, 9], with the defect densities reaching a maximum value of 2.5×10^{10} per cm^2 within 400 nm size of the Y-211/Y-123 interface. We have chosen frames of 80 nm x 80 nm at different locations in the sample and calculated the average defect density to be 3×10^{10} per cm^2. The observed domain structure and the defects within them might have their origin in the local stresses in the Y-123 matrix caused by lattice mismatch effects arising from uniformly distributed fine Y-211 particles. Since our sample is free from low T_c phases and any added nano-sized dopants, we believe that the enhanced J_c and its improved magnetic field dependence can be attributed to the nano-sized defects present in the Y-123 matrix, as observed by TEM.

6.5. Orientation studies using EBSD

The optimized sample S-460 was further studied employing Electron Back Scattered Diffraction (EBSD) technique. Two regions from the sample were chosen such that the distribution of Y-211 particles in the matrix of Y-123 is relatively dense in one and less so in the other.
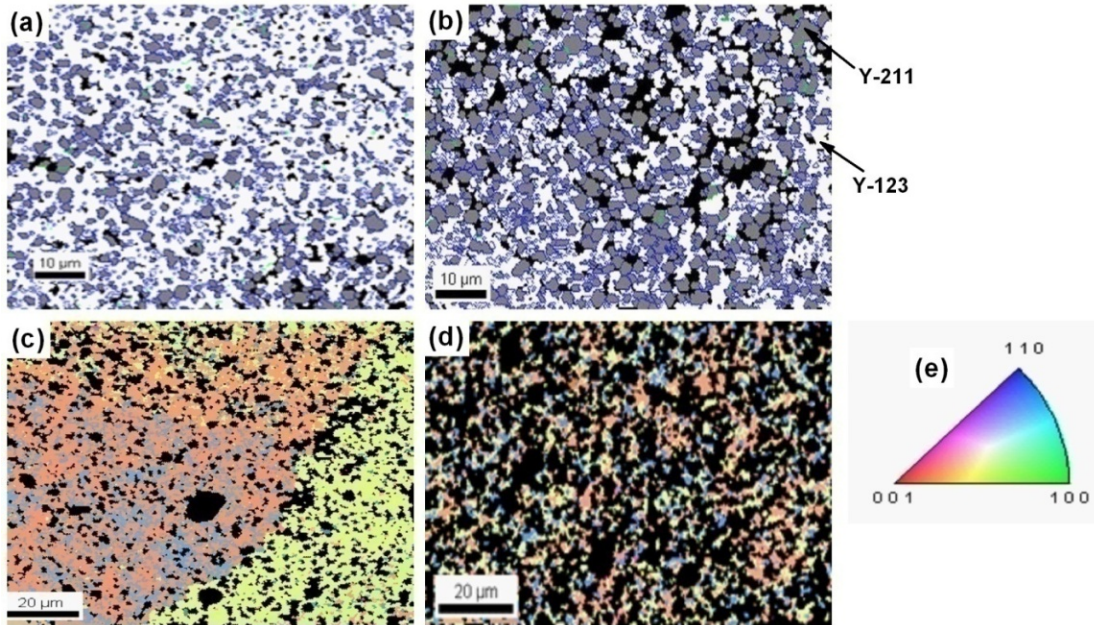
Fig. 6.7. Electron Back Scattered Diffraction (EBSD) results obtained on the S-460 sample are shown. A step size of 50 nm was used in the scans and the variation in crystallographic orientations was mapped. In (a), white areas correspond to Y-123 matrix and the gray areas to Y-211 particles. The blue lines in these figures denote high angle grain boundaries. In (b), it can be seen that such domain boundaries are abundant in areas where the Y-211 inclusions are densely distributed. Crystal orientation maps for the Y-123 phase from areas similar to those in (a) and (b) are presented in (c) and (d) respectively. It is seen from (c) that only two orientations co-exist in the region with relatively sparse population of Y-211 inclusions. This can be seen as regions colored yellow and blue in one domain and pink and blue in the other. In (d), in a region with the Y-211 inclusions are densely distributed, all the three orientations (colored yellow, blue and pink) are seen to occur together. The orientation at a point can be read from the color code of the stereographic triangle provided in (e).

Figs. 6.7(a) and (b) show the phase maps obtained from the EBSD data. The gray regions correspond to the Y-211 phase whereas the white regions are the superconducting Y-123. The blue and green lines (color) are the high- and low-angle grain boundaries respectively. Crystal orientation maps for the Y-123 phase are

131

shown in Figs. 6.7(c) and (d) covering areas with a higher fraction of the Y-123 phase (Fig. 6.7(a)) and a higher fraction of the Y-211 phase (Fig. 6.7(b)). The color coding is as shown in the inverse pole figure provided in Fig. 6.7(e).

An interesting observation was the occurrence of High Angle Domain Boundaries (HADBs), particularly in the proximity of Y-211 precipitates throughout the S-460 sample as shown by lines surrounding the Y-211 particles, (blue online) in Figs. 6.7(a) and (b). It can be observed from Fig. 6.7(a) that the density of such HADBs decreases in regions where Y-211 inclusions are not in close proximity to one another. The [001] orientations of neighboring domains were found to be directed along two mutually orthogonal directions where the density of the Y-211 inclusions is low (compare Figs. 6.7(a) and (c) from the same region). They are directed along three mutually orthogonal directions in the region where the inclusions are in close proximity. Strong influence of the density of Y-211 particles on the orientation distribution of sub-grains in the Y-123 matrix is thus seen. Since the step size used in the EBSD scans was 50 nm, features above 200-250 nm (i.e., four to five successive data points in a row) can be inferred from the present EBSD data. It may thus be deduced that the domain size is above 200 nm. The pole figure and the inverse pole figure obtained on the sample S-460 are shown in Figs. 6.8(a) and (b) respectively. It is evident from the figure that three mutually orthogonal orientations are present in the Y-123 matrix of the sample.
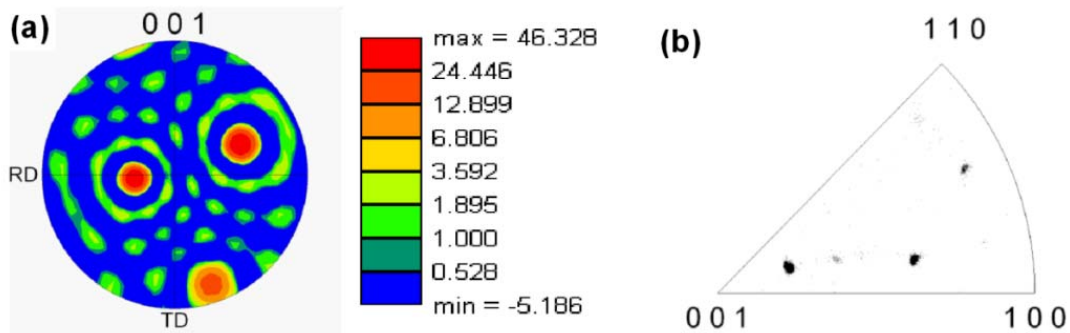
Fig. 6.8 The pole figure and the inverse pole figure obtained on the S-460 sample indicating the orientations observed are shown in (a) and (b) respectively. The extent of orientation can be seen from the color coding provided in (a). RD and TD stand for Reference Direction and Transverse Direction respectively.

The misorientation profile study was carried out in two regions of the sample S-460: one, where Y-211 particles were densely distributed and the other, where the distribution of the particles was relatively less dense. The crystal orientation map (Y-123 phase) where both these regions are present, is shown in Fig. 6.9(a).

The regions where the misorientation studies were carried out are indicated with lines (red in color) drawn on the micrograph. The misorientation profiles obtained from both the regions are shown in Figs. 6.9(b) and (c). It is observed from the figure that the majority of the misorientation is due to the presence of high angle boundaries. It is evident from Fig. 6.9(d), where the total length of the high angle boundaries is tabulated in comparison to the length of the low angle grain boundaries, that a vast majority of the grain boundaries separate neighbouring with a misorientation of 90°. Such boundaries are present in regions where the Y-211 grains are close to one another.

Fig. 6.9. (a) Crystal orientation map for the superconducting Y-123 phase in the S-460 sample is shown. The black regions in this map correspond to grains of Y-211 phase and the partition has been created to show only the Y-123 region in white. The green lines are high angle domain boundaries. The top and left region of the figure has a dense population of Y-211, and the bottom right bottom portion is relatively sparsely populated with Y-211, in the field of view. Misorientation profiles were generated within both the regions. The lines along which the profiles were recorded are shown red (color online). (b) shows the profile recorded from a region densely populated in Y-211 and (c) is from a region that is relatively sparsely populated. In (b), the presence of 90° misorientations between neighboring regions has been observed. In (c), only low angle domain boundaries (neighboring grains misoriented between 1° and 5°) are observed in a region where Y-211 particles are fewer. The width of the 90° domains is measured from (b), and is observed to vary in the range 50 nm to 180 nm. The grain boundary character distribution (GBCD) for the scan area in (a) is shown in (d). As can be seen the most number of boundaries are centered around 90° misorientation.

A study of the orientational relationships among the Y-211 particles is presented in Fig. 6.10. Y-211 particles do not show any preferred orientation as seen from Fig. 6.10(a). Orientations of different Y-211 particles can be deduced from the stereographic triangle shown in the figure. The pole figure and the inverse pole figure in Figs. 6.10(b) and (c) show the randomness in the orientations of the Y-211 particles, similar to the ones reported by others [10].
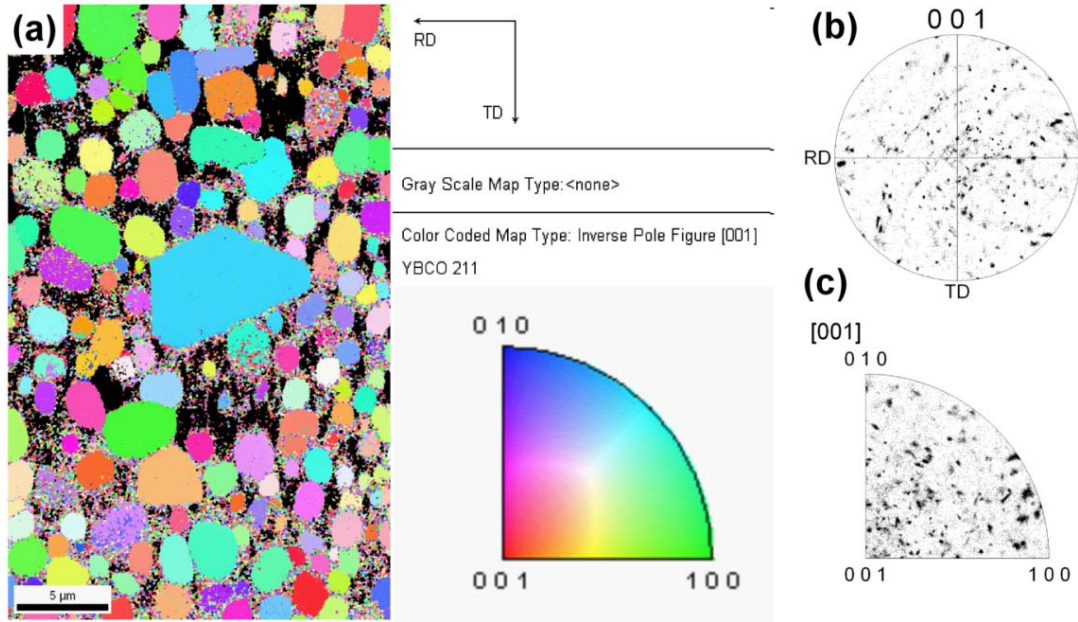
Fig. 6.10 Representative crystal orientation map for the Y-211 phase in the sample S-460 is shown. The corresponding orientations of the particles can be seen from the color coded picture provided in (a). It is evident from the figure that Y-211 particles show random orientation. This is also seen in the pole figure provided in (b) and inverse pole figure provided in (c).

6.6 Nano-twinning observed from FE-SEM in POIGP samples

We have seen in the above that the S-460 sample has a defect structure of the size needed to support enhanced current densities to high applied magnetic fields. The techniques (TEM and EBSD) used above are quite involved and it is difficult to study all the samples using those expensive and involved techniques.

In order to understand the nature of defect structure in the other POIGP samples (S-300, S-380 and S-540), we have studied them in detail using FE-SEM.

The FE-SEM images obtained under higher magnifications of 25,000 x and 50,000 x from the samples S-300 and S-380 at are shown in Fig. 6.11 and those from samples S-460 and S-540 are shown in Fig. 6.12 respectively.

We observed twinning in the Y-123 matrix in all the YBCO samples fabricated by POIGP. We examined the features observed in FE-SEM more closely. The widths of the twin variants are in the range 25 to 100 nm. It can be seen from Figs. 6.12(a) and (b) recorded in S-460 that in areas where the Y-211 grains are in close proximity, the twin orientations are affected resulting in occurrence of crossing twins. This is expected to enhance the twin boundary density considerably. There are no reports on observation of twinning in IG processed samples, to our knowledge. The observation of crossing twins and large twin density in sample S-460 and the presence of large density of fine defects associated with wide-spread twinning in the Y-123 matrix, can possibly account for the superior flux pinning and the observed enhancement of J_c to high fields.

Fig. 6.11. FE-SEM images obtained under a magnification of 25,000 x and 50,000 x from the samples S-300 and S-380 are shown. Nano-twinning is seen in both the samples. The twin widths were found to be in the range 40 nm – 100 nm.

Fig. 6.12 FE-SEM images obtained under a magnification of 25,000 x and 50,000 x from the samples S-460 and S-540 are shown. The images show extensive nano-twinning throughout the samples. The twin widths vary in the range 25 nm – 100 nm. Changes in twin directions giving rise to crossing twins can be observed in the areas where small Y-211 particles are in close vicinity. Abundance of crossing twins resulting in increased twin density is observed in the sample S-460.

6.7 Origin of enhanced flux pinning

6.7.1 Defects of different size ranges

Theoretical considerations [7, 11] show that defects even smaller than the twin boundary widths are required to account for the large flux pinning observed to very high fields in the optimized sample. We present in table 6.1, the observed defect spacings and defect densities, as estimated from FE-SEM, EBSD and TEM in S-460 sample. It can be seen that the defect spacings range from a few nanometers to several hundreds of nanometers. Using the Eq. 6.2, the peak field H_p values are computed for various observed ranges of defect spacings, and are listed in the last column in table 6.1. It can be seen that the computed H_p values range from 10 mT to 10 T. This would explain the observed large flux pinning in a broad range of magnetic fields, from very low fields up to 10 T, in the optimized POIGP sample (S-460).

Table 6.1. Range of peak fields (H_p) computed for the S-460 sample from various microstructural features observed by different techniques.

Microstructural parameter	Studied using	Figure	Range observed	Computed range of Peak fields (H_p)
Twin widths	FESEM	Fig. 6.12	100 nm to 25 nm	0.23 T to 4 T
Domain Sizes	TEM	Fig. 6.5(a)	500 nm to 100 nm	**10 mT** to 0.2 T
Spacing between nano-defects	TEM	Fig. 6.5(b)	52 nm to 15 nm	0.85 T to **10 T**
High Angle Domain Boundaries	EBSD	Fig. 6.9(b)	250 nm to 200 nm	37 mT to 58 mT

6.7.2 Twin boundary energy computations

Though POIGP led to a uniform distribution of fine sized Y-211 particles in the Y-123 matrix of all the samples studied, the field dependence of J_c observed in sample S-460 was the best. An attempt is made in further understanding the reasons for enhancement in J_c(H) observed in optimized S-460 sample.

Twin boundary (TB) energies (γ_{tw}) were computed for the samples (S-300, S-380, S-460 and S-540) fabricated by POIGP employing the twin shape method suggested by Boyko et al. [12]. According to the twin shape method, the TB energy is computed following the relation given below in Eq. 6.3.

$$\text{Twin Boundary energy } (\gamma_{tw}) = \frac{\mu\epsilon_t^2 T_w^2}{NG} \quad \text{.......... (6.3)}$$

where T_w is the inter-lamellae distance, G is the size of the crystal, μ is the in-plane shear modulus ($\sim$ 9.5 x 10^{10} Nm^{-2} for Y-123), ϵ_t is the shear-strain associated with the phase transformation and N (=4π) is a geometrical constant. Using reported values for the constants [12-17], we have computed the TB energies for our samples and plotted them in Fig. 6.13 as a function of the applied preform compaction pressure.
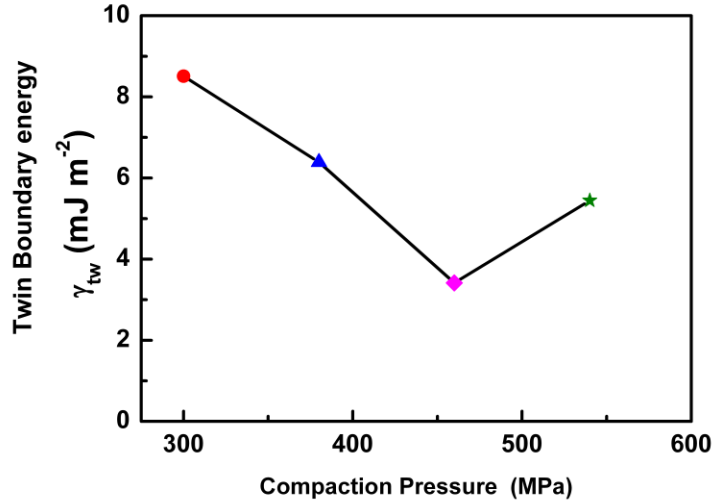
Fig. 6.13. Variation of Twin boundary energy as a function of preform compaction pressure for the samples fabricated by POIGP.

The sample S-460 shows the lowest TB energy of 3.4 mJ m^{-2}. The lower TB energy favors easy formation of twins. The observed crossing twins and large twin density in sample S-460 may be attributed to the low twin boundary energies. The presence of large density of such fine defects in the Y-123 matrix can account for the enhancement of J_c at higher fields in the sample S-460.

6.8. Twinning in YBCO/Ag composites

As discussed in Chapter IV, YBCO/Ag samples fabricated by POIGP also showed high current densities to high applied magnetic fields. To investigate the possible sources of flux pinning at high fields, the defect structure of the YBCO/Ag samples (samples *A* to *D*) is further studied employing FE-SEM operating under high magnification. In Fig. 6.14, we show images obtained at higher magnifications from the sample without Ag (sample *A*) and that from sample with 20 wt.% Ag (sample *D*).
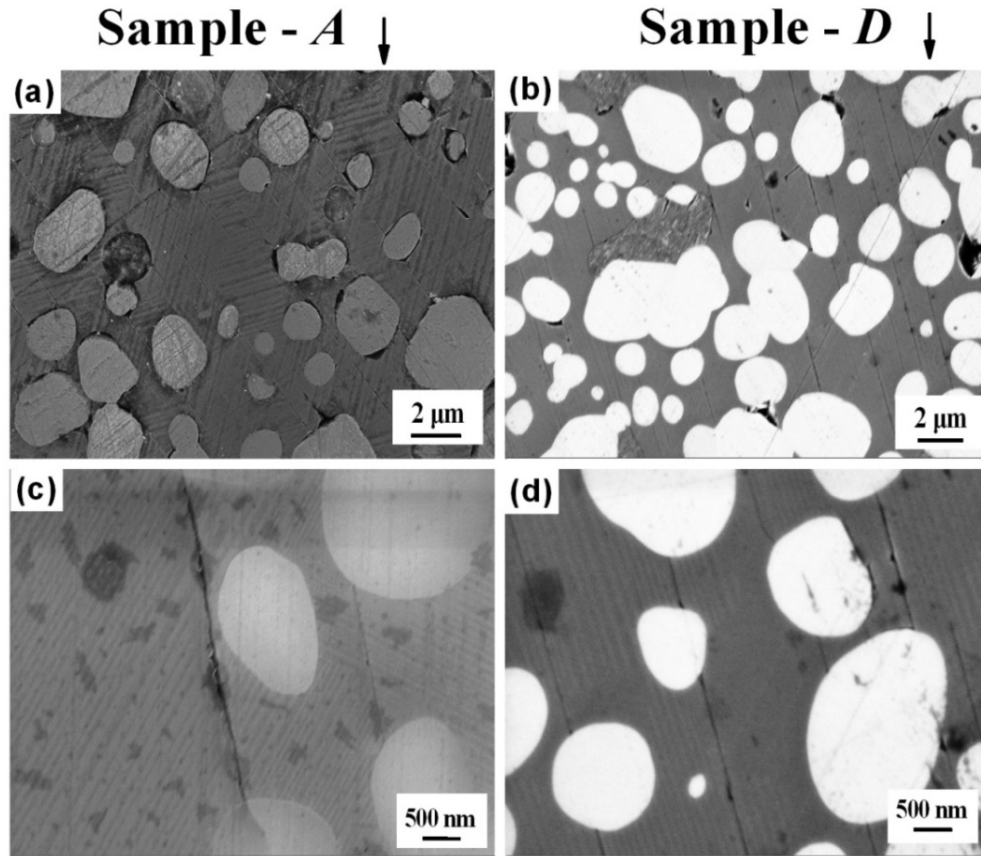
Fig.6.14. (a) and (c) show the microstructure of sample *A* (without Ag), at magnifications of 15,000 x and 50,000 x respectively. Extensive twinning, with crossing twins in regions where Y-211 grains are close to one another, can be seen. (b) and (d) show the microstructure of sample *D* (with 20 wt. % Ag introduced through liquid phase source), at magnifications of 15,000 x and 50,000 x respectively. Extensive twinning, with all the twins in a single direction and parallel to one another, can be observed. Similar twinning was observed in the microstructures of samples *B* and *C* as well. The twin-widths were observed to be in the range 25 – 100 nm.

Widespread twining can be observed in both these samples. The twin widths vary in the range 25-100 nanometers in all the Ag-free and Ag containing YBCO samples fabricated by POIGP. Twinning can influence $J_c(H)$ by the creation of additional defects, thereby increasing the effective defect density available for flux pinning. It is reported that a MG processed YBCO sample exhibiting twin density of ~ 10 per μm showed a zero field J_c of 53 kAcm^{-2} at 77 K [18]. At a higher magnification of 50,000 x, in Fig. 6.14(c) for sample *A*, we observe that the twins frequently change their directions in the vicinity of Y-211 particles and that there are crossing twins in the sample whenever Y-211 particles are in close proximity. In contrast, in all the silver containing samples (*B*, *C* and *D*), the twins occurred in a single direction and parallel to one another all over the sample; we show the twinning in sample *D*, as an example, in Fig. 6.14(d).

6.9 Nano-Twinning in YBCO superconductors fabricated by Directionally Solidified POIGP

The YBCO samples made in relatively shorter time durations (~ 30 hours) employing directionally solidified POIGP showed irreversibility fields higher than 5 T at 77K. As discussed in Chapter V, the optimized sample (DS-460) showed a uniform distribution of fine sized Y-211 particles in the matrix of Y-123. The field dependence of J_c was found to be superior for DS-460 compared to other DS-POIGP samples.

FE-SEM images obtained at a magnification of 25,000 x from the samples DS-380, DS-460 and DS-540 are shown in Fig. 6.15.
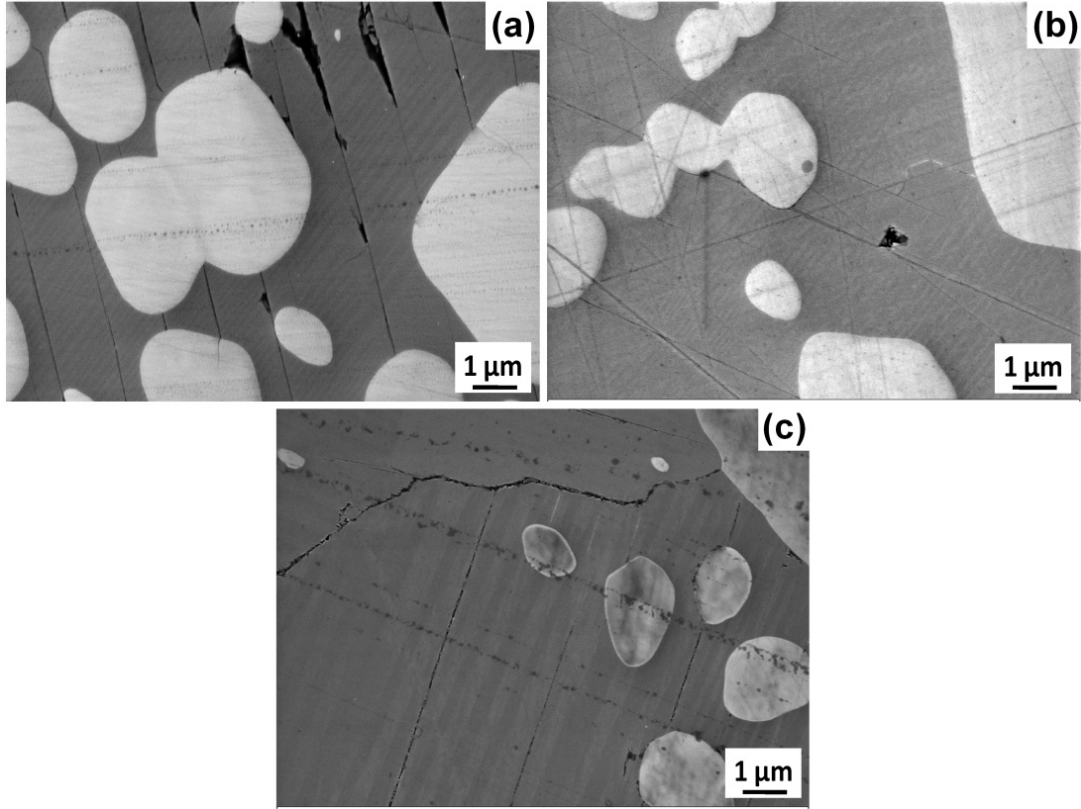
Fig. 6.15. FE-SEM images obtained under a magnification of 25,000 x and 50,000 x from the samples DS-380 DS-460 and DS-540 are shown. Extensive twinning on nano-scale is seen in all the samples. The optimized sample (DS-460) showed presence of fine twins with the twin widths in the size range 40 nm – 100 nm.

Twinning on nano-scale was observed in all the DS-POIG processed samples. The twin widths were found to be in a wider range of 40 to 650 nm in these samples, compared to POIGP samples that have been subjected to long heat-treatment schedules. The less dense distribution of Y-211 might result in lower residual stresses causing wider twins in the DS-POIGP samples. An increase in twin width leads to lower defect density and hence lower $J_c(H)$ in DS-POIGP samples compared to the POIGP samples subjected to long heat treatments.

In REBCO superconductors, twins and twin boundaries (TB) are known to appear during the transformation from the non-superconducting tetragonal (T) phase to the superconducting orthorhombic (O) phase [12-14] to accommodate the

strain involved. Twins and TBs thus formed are reported to act as pinning centers causing enhancement of $J_c(H)$ in MG processed Y-123 [12-14, 19]. However, the highest J_c reported is 10 kAcm^{-2} at 2 T and 77 K, in twinned samples [20]. Compared to these values, the POIGP samples currently studied showed larger J_c to much higher fields of 10 T even at 77 K and the field dependence of J_c observed in sample S-460 was comparatively the best.

It appears that the addition of Ag has not only refined the Y-211 particles and fused the platelet gaps but also relaxed the stresses to some extent in regions close to Y-211 particles thus eliminating crossing twins from the Ag-containing samples. Thus the spatial defect density is lower in Ag containing samples compared to that of the Ag-free YBCO sample. This can possibly account for the much higher J_c in sample *A* in comparison with the silver containing sample *D*.

6.10 Possible mechanisms of flux pinning in YBCO samples fabricated by POIGP

In chapter III, we have shown that the J_c exhibits an exponential variation with applied field and the dependence of normalized J_c fits quite well to the exponential decrease with two terms. The field dependence of J_c was found to fit to an expression shown below (Eq. 3.2 is reproduced here for convenience).

$$\frac{J_c(H)}{J_c(0)} = A_1 \exp\left(-\frac{\mu_o H}{t_1}\right) + A_2 \exp\left(-\frac{\mu_o H}{t_2}\right) + y_0 \quad \ldots\ldots\ldots(6.2)$$

where A_1, t_1, A_2, t_2 and y_0 are the fit parameters

In Chapter III, we have correlated the fit parameter A_2 of the exponential decay and also the $J_c(0)$ obtained at 77 K, with the Y-211 content in the samples. The correlations observed supported the view that the flux pinning at low fields depends on the Y-211 content and possibly originates in defects at the Y-211/Y-123 interfaces.

144

In Fig. 6.16(a), we show that H_p for the samples vary linearly with the fit parameter t_1 of the first term in Eq. 2. We recall from Chapter III, Fig. 3.12(b), that the first term fits the high field region of the J_c versus H curve. From FE-SEM micrographs shown in Figs. 6.11 and 6.12, we have computed the area fraction occupied by nano-twins by measuring the area containing twins and normalizing it to the total frame area which is expressed as a percentage, A_{tw}. We then computed the area under the F_p versus H curves, shown in Fig. 3.11(b), to estimate the total flux pinning force (ΣF_p) arising from various defects operative at different fields. The variation of ΣF_p with A_{tw} is shown in Fig. 6.16(b). The correlations shown in Figs. 6.16(a) and (b) suggest that the flux pinning at high fields, represented by Term-1 in Eq. 6.2, originates from the defect density associated with twinning in the samples fabricated by POIGP.
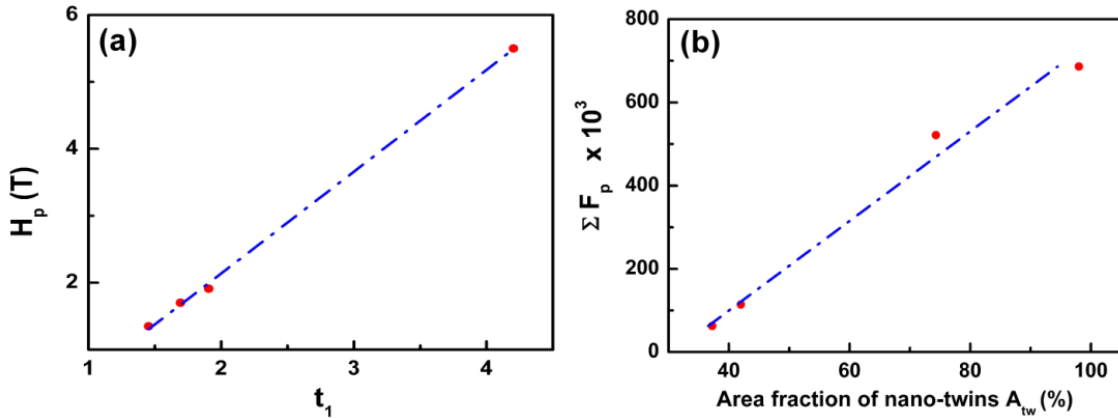
Fig. 6.16 (a) Variation of peak field H_p of the samples is shown as function of the fit parameter t_1 used in the exponential decay equation applied to the high field regions. (b) The total flux pinning force (computed as the area under the flux pinning force versus field curves, shown in Fig. 3.11(b)) for different samples, is shown against A_{tw}, the area fraction showing nano-twins estimated from Figs. 6.11 and 6.12 and expressed as a percentage. The observed correlations in (a) and (b) support the conclusion that the high current densities to very high fields in the POIGP sample has its origin in extensive twinning on a nano-scale in the optimized samples.

References

[1]   Bean C P 1962 *Phys. Rev. Lett.* **8** 250

[2]   Chen D X and Goldfarb R B 1989 *J. Appl. Phys.* **66** 2489

[3]   Murakami M, Morita M, Doi K and Miyamoto K 1989 *Jpn. J. Appl. Phys.* **28** 1189

[4]   Johansen T H, Koblischka M R, Bratsberg H and Hetland P O 1997 *Phys. Rev. B* **56** 11273

[5]   Wei C D, Liu Z X, Ren H T and Xiao L 1996 *Physica C* **260** 130

[6]   Mahesh Chandran 1998 *Physica C* **304** 202

[7]   Nakamura M, Hirayama T, Yamada Y, Ikuhara Y and Shiohara Y 1996 *Jpn. J. Appl. Phys.* **35** 3882

[8]   Jin S, Kammlott G W, Nakahara S, Tiefel T H and Graebner J E 1991 *Science* **253** 427

[9]   Rabier J, Sandiumenge F, Plain J, Proult A, Tall P D and Obradors X 2002 *Radiation Effects and Defects in Solids* **157** 871

[10]   Koblischka-Veneva A and Koblischka M R 2008 *Mater. Sci. Eng. B* **151** 60

[11]   Krabbes G, Fuchs G and Canders W-F 2005 *High Temperature Superconductor Bulk Materials: Fundamentals - Processing - Properties Control - Application Aspects* (Wiley, GmbH, KGaA, Weinheim)

[12]   Boyko V S, Chan S-W and Chopra M 2001 *Phys. Rev. B* **63** 224521

[13]   Mei L, Boyko V S and Chan S-W 2006 *Physica C* **439** 78

[14]   Boyko V S 2008 *Low Temperature Physics* **34** 503

[15]   Barsch G R, Horovitz B and Krumhansl J A 1987 *Phys. Rev. Lett.* **59** 1251

[16]   Cai Z-X and Welch D O 1994 *Physica C* **234** 373

[17]   Roy T and Mitchell T E 1991 *Philos. Mag. A* **63** 225

[18] Suematsu H, Okamura H, Nagaya S and Yamauchi H 1999 *Supercond. Sci. Technol.* **12** 274

[19] Feng Y, Zhou L, Wen J G, Koshizuka N, Sulpice A, Tholence J L, Vallier J C and Monceau P 1998 *Physica C* **297** 75

[20] Boyko V S and Chan S-W 2007 *Physica C* **466** 56

CHAPTER VII

SUMMARY AND CONCLUSIONS

Infiltration Growth process is a powerful process that enables the fabrication of bulk REBCO superconductors in near net shape with improved microstructural features in comparison with the melt growth process [1-9]. Because of the enhanced interest in recent times in using bulk REBCO for several applications, there is considerable interest in optimizing the microstructure and current carrying ability of the IG processed samples. The work presented in this thesis was primarily aimed at improving the performance of IG processed REBCO.

In the present work, modifications were made to the Infiltration growth process by paying special attention to the stability of preform during its fabrication. This modified process is named as "Preform Optimized Infiltration Growth Process (POIGP)". The Y_2BaCuO_5 (Y-211) preforms used were made under relatively higher compaction pressures. It was demonstrated that one needs to sinter the preforms at 950^oC, prior to liquid phase infiltration, for them to acquire mechanical rigidity. Thus POIGP has led to microstructures with a homogenous distribution of Y-211 inclusions in the superconducting Y-123 matrix. The variation in the Y-211 content was < 5% across the volume of the samples fabricated by POIGP.

The effect of compaction pressure under which the Y-211 preform is fabricated on the final microstructures and the resultant current densities in IG processed samples is investigated. It was observed that Y-211 preforms when compacted under an optimized pressure of 460 MPa led to improved microstructures that support considerable current densities in the final product. The optimized sample (referred to as S-460, see chapter III) showed J_c values better than 10^3 Acm^{-2} up to applied magnetic fields of 6.5 Tesla at 77 K. Due to the homogeneity in the distribution of Y-211 particles in the optimized sample, the field dependence of J_c was found to be uniform throughout the sample.

149

The effect of POIGP in refining the Y-211 particles in Y-123 matrix can be seen in Fig. 7.1.
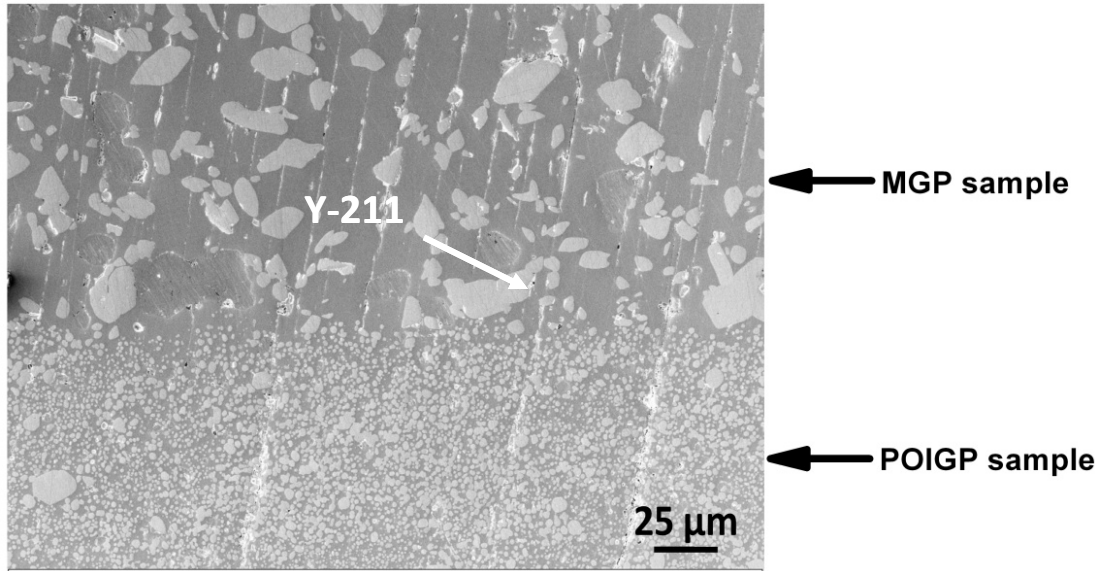
Fig. 7.1. An FE-SEM image obtained at the interface between a MG processed and POIG processed YBCO/Ag superconductor. The image is obtained under a magnification of 1000 x using an inlens detector.

The FE-SEM image obtained at the interface that separates MG processed YBCO and POIGP YBCO using an inlens detector is shown. Y-211 particles were found to be in the size range of 5 – 40 μm in MG processed sample while most of the particles in the POIGP sample were significantly less than 3 μm in size. Further it can be seen from the figure that MGP led to acicular Y-211 particles while their morphology in POIGP sample remained quite spherical. The refinement of Y-211 through POIGP and their uniform distribution are evident from the figure.

Bulk YBa$_2$Cu$_3$O$_{7-\delta}$ (YBCO)/Ag composites with a homogenous distribution of fine and spherical particles of metallic silver and Y-211 have been fabricated employing POIGP. Effect of two different methods of introducing silver, one directly into the Y-211 preform and the other through the liquid phase source placed above the Y-211 preform, on the microstructures and current densities is investigated. Our results show that the latter method is far superior to the former. The samples obtained by introducing silver through liquid phases are nearly free from defects

like voids, pores, macro-cracks and platelet gaps. It was also observed that addition of Ag helped in refining the size of Y-211 particles. Current densities in excess of 10^3 Acm^{-2} up to fields of 2.7 T have been recorded in the Ag-added samples at 77 K. The problems reported in literature with respect to inhomogeneity in the distribution of both Y-211 and Ag particles in the Y-123 matrix and the associated spatial non-uniformity in the current density are successfully resolved by introducing Ag along with the liquid phases.

In addition to the refinement of Y-211 particles, the POIGP was also found to refine the Ag particles. This can be seen from Fig. 7.2, which was recorded in the same region as described in Fig. 7.1 but with secondary electron detector using FE-SEM. Ag particles were found to be in the size range of 10 – 100 μm in MG processed sample [10-14] while most of the particles in the POIGP sample were significantly less than 5 μm in size.
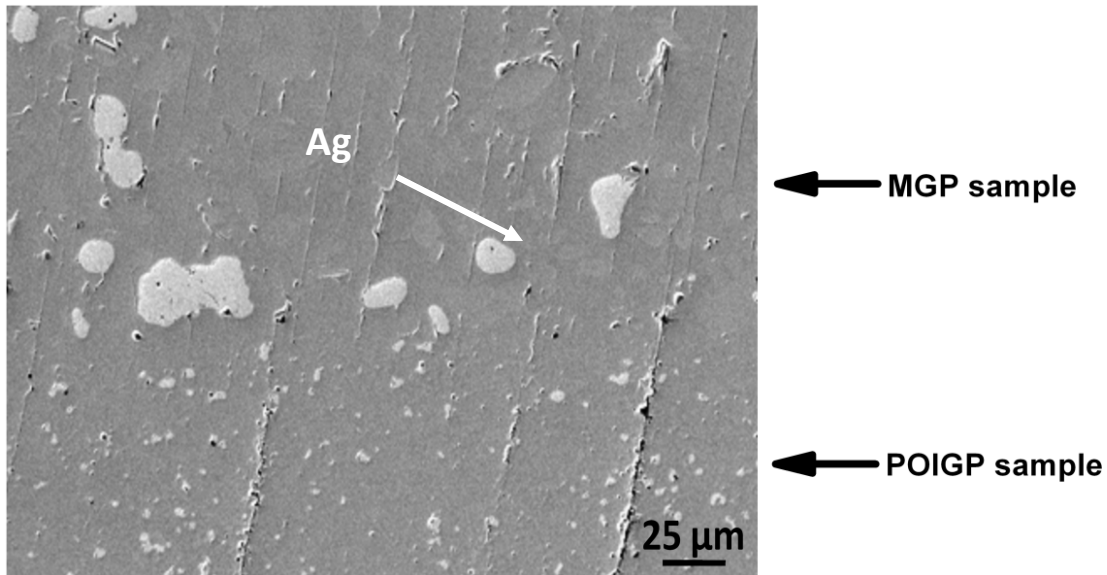
Fig. 7.2. An FE-SEM image obtained at the interface between a MG processed and POIG processed YBCO/Ag superconductor. The image is obtained under a magnification of 1000 x using a secondary electron detector.

Directional Solidification is successfully combined with Preform optimized IG process (DS-POIGP) in order to fabricate YBCO and YBCO/Ag products in short time

durations. Bulk YBCO samples with reasonable critical current densities are fabricated in short time scales of ~ 30 hours. The effect of Y-211 preform compaction pressure on the end microstructures and magnetic properties are studied. It was found that among the DS-POIGP samples, DS-460 with its preform consolidated under a pressure of 460 MPa showed better results from both the microstructural and magnetic property measurements. Ag was introduced along with the liquid phase and the macro-cracks were successfully fused. The YBCO and YBCO/Ag samples fabricated by DS-POIGP showed irreversibility fields better than 6 Tesla even at 77 K. However, the J_c values of DS-POIGP samples are one order lower than the POIGP samples. Further optimization of the processing conditions during directional solidification, to improve the J_c, is worthwhile since DS-POIGP has the potential to be extended to wire fabrication.

The origin of high current densities to very high magnetic fields (better than 10^3 Acm^{-2} to 6.5 Tesla fields at 77 K) in YBa$_2$Cu$_3$O$_{7-\delta}$ superconductor fabricated by the Preform Optimized Infiltration Growth Process is investigated. Techniques like Field Emission Scanning Electron Microscopy and Transmission Electron Microscopy (TEM) were used for studying the defect structure of the optimized sample S-460. An Electron Back Scattered Diffraction study of the sample was also carried out. The results show that extensive twinning on a nanometer scale with crossing twins occur near the optimally separated Y-211 precipitates, and can be the origin of the observed flat $J_c(H)$ response in the optimized sample fabricated by POIGP. TEM study reveals the presence of very fine defects starting from domain boundaries that can be associated with crossing twin regions.

The observed field dependences of normalized J_c of the samples fabricated by POIGP were found to be affected by different pinning mechanisms operative at low and high magnetic fields, each exhibiting an exponential dependence on applied field as indicated in Eq. 7.1.

$$\frac{J_c(H)}{J_c(0)} = A_1 \exp\left(-\frac{\mu_o H}{t_1}\right) + A_2 \exp\left(-\frac{\mu_o H}{t_2}\right) + y_0 \quad \text{...............(7.1)}$$

where A_1, t_1, A_2, t_2 and y_0 are the fit parameters. The details of the fits were discussed in Chapters III and VI.

The term – II, containing the parameters A_2 and t_2, has been found to be applicable at low fields. It was observed that the fit parameter A_2 varies linearly with the Y-211 content present in different POIGP samples. The $J_c(0)$ measured for the samples is also found to vary systematically with Y-211 content. These correlations support the view that the flux pinning at low fields depends on the Y-211 content and the associated defects at the Y-211/Y-123 interfaces.

The term – I, containing the parameters A_1 and t_1, has been found to be applicable at high fields. It was observed that the peak field H_p for different samples fabricated by POIGP varied systematically with the fit parameter t_1 in Term-1 of Eq. 7.1. The area fraction occupied by nano-twins (A_{tw}) was found to correlate with the total flux pinning force ΣF_p for different samples suggesting that the pinning at high fields originates from the defect density associated with twinning observed in the POIGP samples.

It is thus found that a variety of defects like twins, twin boundaries, nano-defects, high angle domain boundaries etc. were observed in the optimized S-460 sample. Various defects are of different sizes ranging from 15 to 100 nm. It is known from literature [15] that defects can influence the J_c giving rise to the observation of a peak in J_c at a particular field H_p; the peak field (H_p) is given by

$$H_p = \frac{2\phi_o}{\sqrt{3}(a_f)^2} \quad \text{.................(7.2)}$$

where ϕ_o is the flux quantum, a_f is the defect size / defect spacing.

Following Eq. 7.2, the peak fields are computed based on the defect sizes and are observed to occur in a range of 10 mT to 10 T in the optimized POIGP sample (S-

460). This appears to be the reason for the flat and uniformly high current densities achieved to large applied magnetic fields.

Preform Optimized Infiltration and Growth Process developed in the present work yields a homogenous and dense distribution of fine Y-211 particles in YBCO superconductor. Extensive nano-twinning with large number of crossing twins, and the associated high defect densities, are identified to be the source of flux pinning in the optimized S-460 sample. Such flux pinning is responsible for the enhanced flat J_c response to high fields. The fact that the optimization of the preform fabrication process generates Y-123 samples which support high current densities to very high magnetic fields without the addition of second phases or grain refiners, could be of practical importance. This is particularly so since there is scope to further improve the current densities supported by the samples by techniques which have already proven to be successful in the case of conventional melt growth process; like the addition of nano-sized inclusions and the use of mixed rare earth REBCO in preform optimized IG process.

References

[1]   Sudhakar Reddy E and Rajasekharan T 1998 *J. Mater. Res.* **13** 2472

[2]   Sudhakar Reddy E and Rajasekharan T 1998 *Supercond. Sci. Technol.* **11** 523

[3]   Viswanath N V N, Rajasekharan T, Harish Kumar N, Menon L and Malik S K 1998 *Supercond. Sci. Technol.* **11** 420

[4]   Cloots R, Koutzarova T, Mathieu J-P and Ausloos M 2005 *Supercond. Sci. Technol.* **18** R9

[5]   Meslin S, Iida K, Hari Babu N, Cardwell D A and Noudem J G 2006 *Supercond. Sci. Technol.* **19** 711

[6]   Iida K, Hari Babu N, Withnell T D, Shi Y, Haindl S, Weber H W and Cardwell D A 2006 *Physica C* **445–448** 277

[7]   Iida K, Hari Babu N, Shi Y and Cardwell D A 2005 *Supercond. Sci. Technol.* **18** 1421

[8]   Chen S-Y, Hsiao Y-S, Chen C-L, Yan D-C, Chen I-G and Wu M-K 2008 *Mater. Sci. Eng. B* **151** 31

[9]   Meslin S and Noudem J G 2004 *Supercond. Sci. Technol.* **17** 1324

[10] Mendoza E, Puig T, Varesi E, Carrillo A E, Plain J and Obradors X 2000 *Physica C* **334** 7

[11] Diko P, Krabbes G and Wende C 2001 *Supercond. Sci. Technol.* **14** 486

[12] Maeda J, Izumi T and Shiohara Y 1999 *Supercond. Sci. Technol.* **12** 232

[13] Iida K, Hari Babu N and Cardwell D A 2007 *Supercond. Sci. Technol.* **20** 1065

[14] Joo J, Kim J-G and Nah W 1998 *Supercond. Sci. Technol.* **11** 645

[15] Nakamura M, Hirayama T, Yamada Y, Ikuhara Y and Shiohara Y 1996 *Jpn. J. Appl. Phys.* **35** 3882

APPENDIX

BASIC CONCEPTS IN SUPERCONDUCTIVITY

A.1 Fundamental properties of Superconductor

Heike **Kamerlingh Onnes** discovered Superconductivity in 1911 in Hg [1]. Superconductivity is a quantum phenomenon. The two basic properties which characterize the superconducting property are:

1. Zero Resistance $(R \approx 0)$
2. Perfect Diamagnetism (Induced magnetic field $B = 0$)

A.1.1 Zero Resistance

At low temperatures, the normal electrons condense into paired state (Cooper pairs are formed) which possesses a reduced and hence more stable-system energy. Whenever the system energy exceeds the condensation energy, the charge carriers will revert back to the normal electronic behavior. The temperature at which the condensation occurs is termed as the critical temperature and is denoted as T_c. This is the temperature below which the measurable resistance of a superconducting material drops to zero. A schematic sketch of the temperature dependence of resistance of a superconductor in comparison to a perfect conductor (non-superconductive metal) is shown in Fig. A.1.

Apart from T_c, there are other parameters which control the superconducting state namely the critical magnetic field (H_c) and critical current density (J_c). A schematic representation of the superconducting state is shown in Fig. A.2.
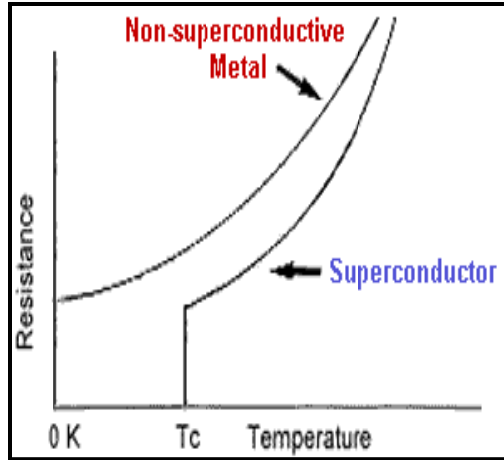
Fig. A.1. Schematic representation of the variation of electrical resistance of a superconductor in comparison to that of a non-superconducting metal.
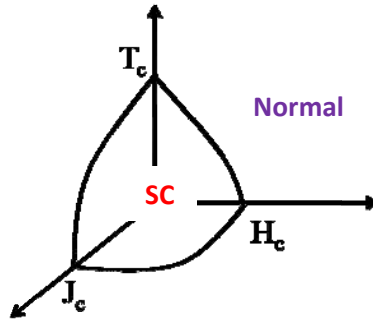
Fig. A.2. A closed contour indicating the superconducting regime.

Many metallic elements and binary alloys were seen to show superconductivity at very low temperatures (< 20 K). The highest T_c of all pure metals was discovered in Nb with T_c = 9.2 K [2]. Nb$_3$Ge was well known among conventional superconductors as its T_c was the record transition temperature of ∼ 23.2 K [3] for a long time, till the discovery of high temperature superconductors.

In 1986, a breakthrough occurred when two European scientists Georg Bednorz and Alex Müller discovered superconductivity in La-Ba-Cu-O compound showing T_c of ∼ 35 K [4]. This discovery triggered the research on oxide based materials and soon led to the important discovery of Y-Ba-Cu-O superconducting

material by Wu et al. which has a $T_c \sim 90$ K [5]. The transition / critical temperature T_c of some of the superconducting elements and alloys are listed in table A.1.

Table A.1. Critical temperature T_c (K) for various superconducting elements and alloys.

	Name	Formula	Critical temperature T_c (K)
Elements	Aluminium	Al	1.2
	Cadmium	Cd	0.52
	Gallium	Ga	1.1
	Indium	In	3.4
	Iridium	Ir	0.11
	Lanthanum	La	4.8
	Lead	Pb	7.2
	Mercury	Hg	4.2
	Niobium	Nb	9.3
	Tantalum	Ta	4.5
	Technetium	Tc	7.9
	Tin	Sn	3.7
	Vanadium	V	5.4
Alloys		Ta-Nb	6.3
		Pb-Bi	8.0
		Nb-Ti	9.2
		Nb_3Zr	11.0
		Nb_3Sn	18.0
		Nb_3Ge	23.2
		V_3In	13.9
		Nb_3Ga	14.5
		Nb_3Si	19
		Nb_3Al	18

The slow but steady search for new superconductors with higher transition temperatures continued for decades until superconductivity was discovered in La–Ba–Cu–O oxide (with $T_c \sim 30$ K) in 1986. Cuprates such as Y–Ba–Cu–O, Bi–Sr–Ca–Cu–O, Tl–Ba–Ca–Cu–O, Hg-Ba-Ca-Cu-O etc. were soon discovered [5-8] which showed superconductivity at temperatures above 77 K, the boiling point of liquid nitrogen.

A.1.2 Meissner Effect

In 1932, Walther Meissner and Robert Ochsenfeld observed that, when a superconductor is exposed to the magnetic field, the magnetic flux gets completely expelled from the interior of the superconductor [9]. This total expulsion of magnetic flux lines is a clear demonstration of the perfect diamagnetic nature possessed by the superconductors.

The induced field 'B' resulting due to an applied field 'H' is given as

$$B = \mu_0(H + M) = 0 \ldots\ldots (A.1)$$

Since in the superconducting state, M = –H, the susceptibility χ becomes:

$$\chi = \frac{M}{H} = -1 \ldots\ldots (A.2)$$

This striking diamagnetic property of the superconductors is interesting from applications point of view, as it opens up a subarea of study – "Magnetic levitation of superconductors" [10-13]. The schematic representation of complete magnetic flux expulsion exhibited by a superconductor establishing the nature of perfect diamagnetism is shown in Fig. A.3.
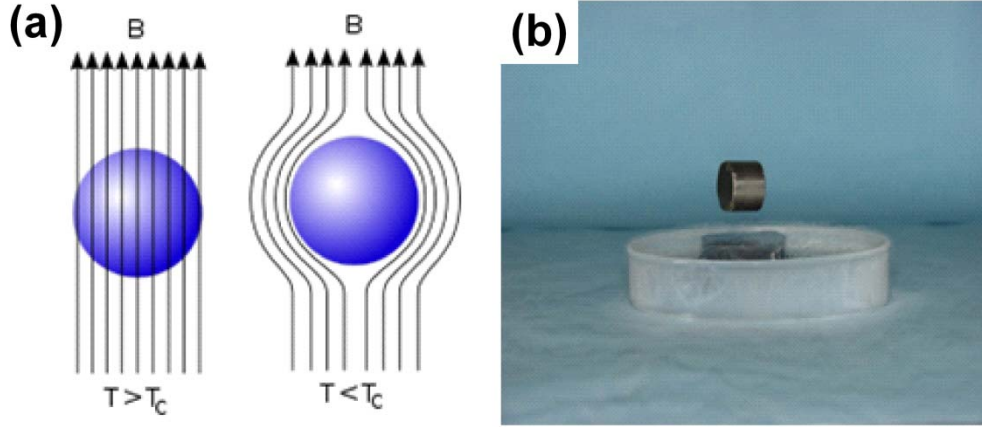
Fig. A.3. (a) Schematic sketch of complete magnetic flux expulsion from the interior of the superconductor when T<T_c can be seen. At T > T_c, the flux enters the superconductor since it is in the normal state. (b) The demonstration of magnetic levitation of a YBCO superconductor levitating a $SmCo_5$ magnet over it. The levitation gap between the superconductor and the magnet was found to be ∼ 7 – 8 mm at 77 K.

A.2 Classification of Superconductors

Superconductors, based on their magnetic properties, can be broadly classified into two kinds namely Type-I and Type-II superconductors [14, 15]. A typical sketch representing the variation of magnetization of a Type-I superconductor with applied field H_e is shown in Fig. A.4(a). When the external magnetic field H_e is lower than the critical field H_c, the magnetization is given by $M = -H_e$ and the superconductor shows a perfect diamagnetism (B = 0). This state is known as the Meissner state. The transition from the superconducting state to the normal state occurs at $H_e = H_c$ with a discontinuous variation in the magnetization to M = 0 (i.e. $B = \mu_0 H_e$ with μ_0 denoting the permeability of vacuum). The classification can also be understood in terms of the reduced parameter $\kappa = \frac{\lambda}{\xi}$, where λ and ξ are two fundamental characteristic lengths namely London penetration depth and coherence length respectively [16]. (The details of these characteristic lengths are discussed in Section A.3 of Appendix). If κ is $< \frac{1}{\sqrt{2}}$ then such materials are called Type I superconductors and if κ is $> \frac{1}{\sqrt{2}}$, then they are classified as Type II superconductors [16].

161

In the case of a Type-II superconductor, the perfect diamagnetism is maintained only up to the lower critical field, H_{c1}, and then the magnetization varies continuously with the penetration of magnetic flux as shown in Fig. A.4(b) until the diamagnetism disappears at the upper critical field, H_{c2}, where the normal state starts.
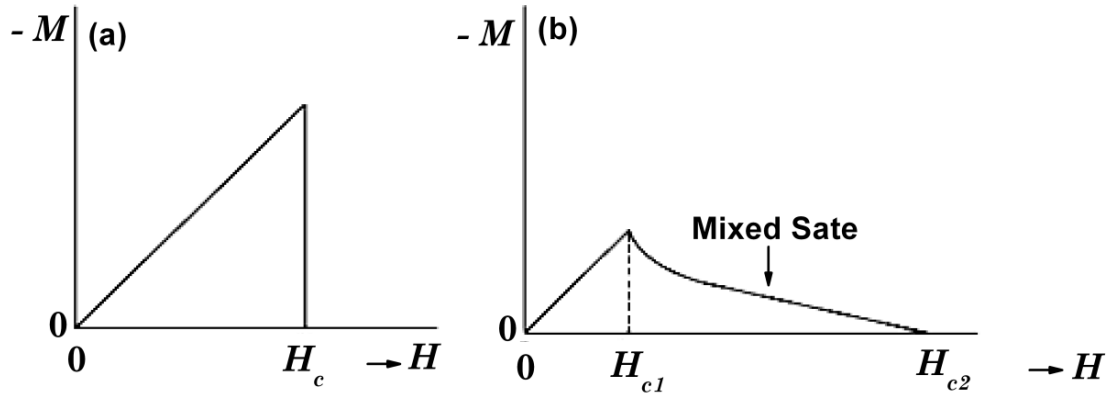
Fig. A.4. Field dependence of magnetization (M) for (**a**) Type-I superconductor and (**b**) Type-II superconductor

It is empirically known that the critical field of Type-I superconductors varies with temperature according to

$$H_c(T) = H_c(0) \left[1 - \left(\frac{T}{T_c} \right)^2 \right] \quad\text{......... (A.3)}$$

where $H_c(0)$ is the absolute critical field (value of H_c at zero temperature)

Both the lower and upper critical fields (H_{c1} and H_{c2}) of Type-II superconductors show similar temperature dependences. Schematic representations of the H-T phase diagrams of Type-I and Type-II superconductors, indicating the variation of H_c with temperature T, are shown in Figs. A.5(a) and (b) respectively.
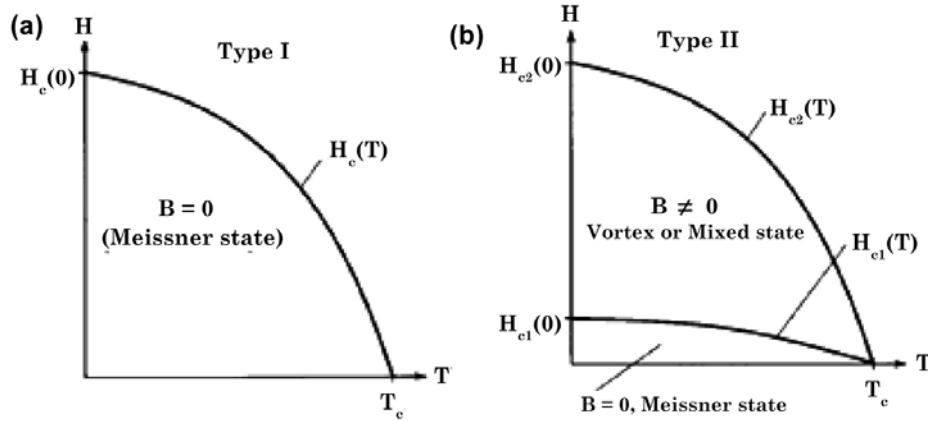
Fig. A.5. Schematic representation of H-T phase diagram of (a) Type-I and (b) Type- II superconductors.

A.3. BCS Theory of Superconductivity

John Bardeen Leon Cooper and Robert Schrieffer, in 1957, proposed the basis of a quantum theory of Superconductivity [17] which is now popularly known as "BSC Theory". Specific accomplishments of BSC theory are:

1. An attractive interaction between electrons can lead to a ground state separated from the excited states by an energy gap. The critical field, the thermal properties and most of the electromagnetic properties of consequences of the energy gap.

2. The electron-lattice-electron interaction leads to an energy gap of the observed magnitude. The indirect interaction proceeds when one electron interacts with the lattice and deforms it; a second electron sees the deformed lattice and adjusts itself to take advantage of the deformation to lower its energy. Thus the second electron interacts with the first electron with the first electron via the lattice deformation.

3. The penetration depth and the coherence length emerge as natural consequences of the BCS theory. The London equation is obtained for magnetic fields that vary slowly in space. Thus the central phenomenon in superconductivity, the Meissner effect, is obtained in a natural way.

163

4. The criterion for the transition temperature of an element of alloy involves the electron density of orbitals $D(\epsilon_F)$ of one spin at the Fermi level and the electron-lattice interaction U, which can be estimated from the electrical resistivity at room temperature is a measure of the electron-phonon interaction. For U $D(\epsilon_F)$ <<1, the BCS theory predicts T_c as:

$$T_c = 1.14\ \theta \exp\left[-\frac{1}{U\ D(\epsilon_F)}\right] \ldots\ldots\ldots (A.4)$$

where θ is the Debye temperature and U is an attractive interaction. This result for T_c is satisfied at least qualitatively by the experimental data.

5. Magnetic flux through a superconducting ring is quantized and the effective unit of charge is 2e rather than e. The BCS ground state involves pairs of electrons; thus flux quantization in terms of the pair charge 2e is a consequence of the theory.

A.4 Characteristic lengths in Superconductors

In Superconductivity, there are two characteristic lengths namely the penetration depth and the coherence length

A.4.1 Penetration depth

The penetration depth refers to the exponentially decaying magnetic field at the surface of a superconductor. The London equations, developed in 1935 by Fritz London and Heinz London [18] relate electrical current to the electromagnetic fields for a superconductor. These equations could explain the experimentally observed Meissner effect, wherein a material expels all internal magnetic fields on cooling below T_c, as it reaches the superconducting state.

The two London equations are

$$\frac{\partial J_S}{\partial t} = \frac{n_s e^2}{m} E \dots\dots (A.5)$$

$$\nabla X J_S = -\frac{n_s e^2}{m} B \dots\dots (A.6)$$

where J_s is the superconducting current density,

E is the electric field within the superconductor

B is the magnetic field inside the superconductor,

e is the charge of an electron

m is the mass of an electron

n_s is a phenomenological constant associated with a number density of superconducting carriers

The London's first equation (Eq. A.4) is also known as modified Ohms law and is valid for both superconductors and perfect conductors.

The second London's equation when treated with Ampere's law $\nabla X B = \mu_0 J_s$ gives

$$\nabla^2 B = \frac{1}{\lambda^2} B \dots\dots (A.7)$$

The solution of this differential equation results as

$$B_Z(x) = B_0 e^{-\frac{x}{\lambda}} \dots\dots (A.8)$$

Thus, the London equations imply a characteristic length scale, λ, over which external magnetic fields are exponentially suppressed This value λ is the London penetration depth. Thus, when a magnetic field of intensity B_0 is applied to a superconductor, it decreases as a function of distance x inside the superconductor and the variation is of the form shown in Eq. A.7.

It shows that, in order to have zero field within the bulk of the material, one must have a sheet of superconducting currents which flow within λ_L from the

surface and which create an opposite field inside the superconductor that cancels the externally applied magnetic field.

At a depth x = λ = λ_L, B = $\frac{B_0}{e}$. This implies that London penetration depth is the length into the superconductor by which the B becomes 1/e times of the applied field intensity B_0. Typical values of λ_L range from 50 to 500 nm.

The Penetration depth λ is related to the density of superconducting electrons (n_s) as:

$$\lambda \equiv \sqrt{\frac{mc^2}{4\pi n_s e^2}} \ldots\ldots (A.9)$$

A.4.2 Coherence length

One of the characteristic lengths for the description of superconductors is called the coherence length [19]. Superconducting coherence length denoted as ξ gives approximate spatial dimension (size) of the Cooper pair. This also sets the length scale on which the superconducting order parameter changes considerably. The coherence length is related to the Fermi velocity v_F and the energy gap E_g of the material as

$$\xi = -\frac{2\hbar v_F}{\pi E_g} \ldots\ldots (A.10)$$

where E_g is the superconducting energy gap

$\hbar = \frac{h}{2\pi}$, h is the Planck's constant

v_F is the Fermi velocity

A.5 Vortex matter

In Type-I superconductors, no magnetic flux can enter the material as long as it is in the superconducting state. Once the applied field is more than the critical field H_c, the magnetic flux enters the material since it becomes normal.

In Type-II superconductors, the coherence length is smaller than the London penetration depth [16, 19]. The partial diamagnetic state occurring between the lower critical field (H_{c1}) and (H_{c2}) in the M-H phase diagram as shown in Fig. A.4(b) is called the mixed state.

In the mixed state, the magnetic flux lines enter the material in narrow regions which become non superconducting and are comparable to the size of coherence length [16, 19]. The entry of flux lines occurs in the form of vortices / fluxoids. The entry of a fluxoid locally loses the condensation energy. The loss of energy due to the penetration of fluxoid is called the penalty energy and is $\frac{H_c^2}{2\mu_o}$ per unit volume.

The vortices are surrounded by rings of super-currents which shield the rest of the superconductor from getting exposed to the applied magnetic fields. The vortices arrange themselves in a regular structure known as the vortex lattice as described by Abrikosov [20]. This is a quantized effect with the flux quantum associated with each of the vortices being $\Phi_0 = h/2e$, where h is the Planck's constant and 2e is the total charge of the Cooper pair. A schematic representation of the fluxoids in the sample volume is shown in Fig. A.6.
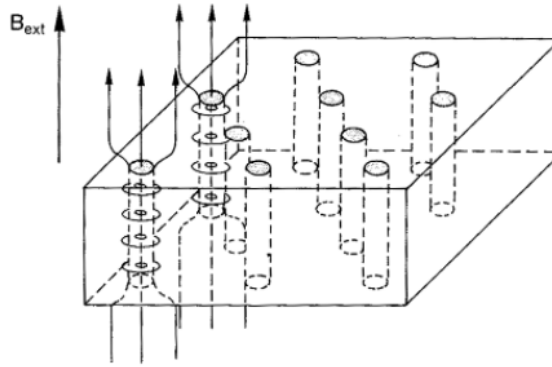
Fig. A.6. Schematic representation of the mixed state of a Type-II superconductor. The flux tubes (fluxoids) arranged in a two-dimensional lattice, allow the magnetic field to penetrate. Each fluxoid is surrounded by superconducting ring currents and enclose one magnetic flux quantum.

The magnetic field, when applied parallel to c-axis of the samples generates super-currents in the a-b planes of the sample. Since the applied magnetic field and the generated super currents are perpendicular to each other, Lorentz force gets generated which tends to move the vortices causing energy dissipation. This is schematically shown in Fig. A.7.
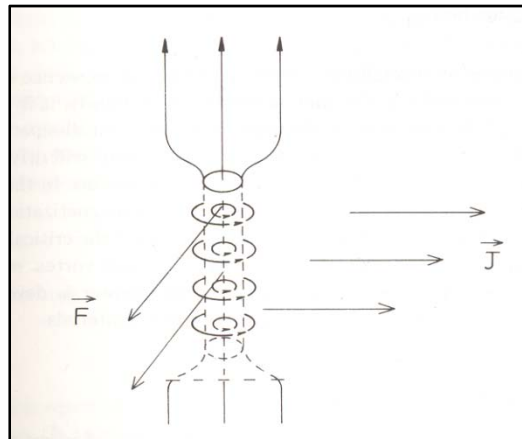
Fig. A.7. A schematic sketch showing the direction of the Lorentz force resulting on the vortices due to the application of magnetic field.

In order to minimize the motion of vortices, pinning centers need be introduced which pin the magnetic flux lines. This is achieved through vortex pinning or flux pinning, by creating normal sites out of which the vortex cannot

168

leave without large energy increase [21]. The vortex will be pinned to such inclusions as it does not have to spend energy to destroy superconductivity in that inclusion. An inclusion is most efficient when its diameter matches with the coherence length ξ of the material [22].

The bulk pinning force dented as F_p is the sum over all contributions from various pinning centers, and if the number of interactions per unit volume is N, then F_p becomes equal to Nf_p, where f_p is the elementary pinning force [23]. Critical current density is related to the flux pinning force F_p as

$$F_p = Nf_p = J_c \times B \dots\dots\dots (A.11)$$

A.6   Bulk high temperature superconductors

A.6.1   Critical temperature

The critical temperatures of some of the high temperature superconductors are shown in table A.2

Table A.2. Critical temperature T_c (in K) of some high temperature superconducting compounds

System	Symbol	Composition	Critical Temperature T_c(K)
Copper oxide based superconductors	La based	$La_{2-x}Sr_xCuO_4$	35
	YBCO	$YBa_2Cu_3O_{7-\delta}$	92
	BSCCO	$Bi_2Sr_2Ca_2Cu_3O_{10}$	110
	TBCCO	$Tl_{1.6}Pb_{0.6}Sr_2Ca_2Sb_{0.1}Cu_3O_x$	127
	Hg based	$Hg_{0.8}Tl_{0.2}Ba_2Ca_2Cu_3O_{8.33}$	138
Boride based Superconductors		MgB_2	39
		$ThPd_2B_2C$	14.5
Iron based superconductors		SmFeAs	55
		CeFeAs	41
		LaFeAs	26

A.6.2 Flux creep and Irreversibility fields

Though HTS have large upper critical fields (H_{c2}), the fields up to which these materials are practically usable are called Irreversibility fields [24]. Applications of REBCO superconductors are limited to magnetic fields below their respective irreversibility fields (H_{irr}). The irreversibility field is defined as the field by which the current density J_c is better than 100 Acm^{-2} [25]. In the field range $H_{irr} < H < H_{c2}$, the effect of thermal fluctuations on the vortex lattice becomes so strong that currents cannot flow without losses although the superconductor has not yet reached the normal state. A transition of the vortex lattice from vortex glass to a vortex liquid state occurs above H_{irr} [26]. The boundary between the reversible region and the irreversible region with non-zero critical current density J_c in low temperatures and / or magnetic fields in the H-T plane is called the irreversibility line (IL). This is schematically shown in Fig. A.8.

Though BSCCO has higher critical temperature of $\sim$ 110 K, the problems of flux creep confines the operation of this material to only 1/4th of its T_c [27, 28]. In this context, YBCO becomes more interesting as the flux creep problems are minimal in these materials [29].

A.6.3 Applications of bulk REBCO superconductors

Some of the devices erected for various applications comprising bulk REBCO superconductors are shown in Fig. A.8.

Fig. A.8 (a) A schematic picture of a noncontact superconducting mixer. The upper part is coupled by an attractive force between two Fe–Nd–B magnets and the lower part is coupled by the attractive force between an Fe–Nd–B magnet and bulk Gd–Ba–Cu–O superconductor [30] (b) Photograph of a magnetic separation device for water purification. Bulk Gd–Ba–Cu–O magnets are cooled by a cryocooler and inserted into the device after magnetization by a superconducting solenoid. [33] (c) Single-pole and (d) double-pole magnetic field generators using RE-Ba-Cu-O magnets [34] (e) Levitated vehicle carrying two people [36] (f) Synchronous motor with bulk RE–Ba–Cu–O magnets on operation. The motor is rotating a propeller for ship propulsion. [38] (g) Flywheel energy storage system that can store 10 kWh [47].

171

A.5.3.1 Superconducting mixers

The development of noncontact mixers is desired for mixing various solutions for medical and biotechnological applications [30]. The production of contaminant free vaccines has a huge impact on the medical treatment of people. The conventional mixers employ ceramic ball bearings for the rotation wing parts that mix solutions. But, these mechanical contacts often cause contamination of materials demanding that solutions must be cleaned with filters after mixing. Noncontact superconducting mixers have already been devised using the flux pinning of bulk superconductors [31]. In this device, two magnet components are coupled by a single bulk superconductor via flux pinning. A schematic sketch demonstrating the arrangement is shown in Fig. A.8(a). Here, bulk RE–Ba–Cu–O is immersed in a liquid nitrogen bath inserted between two magnets and rotate freely in liquid nitrogen. The rotation of the bottom permanent magnet driven by the outer rotating device is transferred to the top magnet attached to the mixer wing via a bulk superconductor by virtue of flux pinning.

A.5.3.2 Trapped field magnets and Magnetic separation device

Bulk superconducting magnets can be used as a magnetic source like permanent magnets [32]. The superconductors are field cooled during which the magnetic flux gets trapped in the material. Now, when the external field is removed, the material still acts like a permanent magnet due to the presence of trapped flux. The benefit of the superconducting trapped magnet is that the field strength is much greater than those of conventional permanent magnets like Fe–Nd–B, although refrigeration is necessary. An experimental magnetic separation system has been developed [33] and already commercialized which use trapped field magnets. A photograph of the device is shown in Fig. A.8(b).

Two types of experimental magnet systems are commercially available: a single-pole type and a double-pole type {Figs. A.8(c) and (d)}. Bulk RE–Ba–Cu–O disks are installed at the heads, which are connected to a cryo-cooler and cooled

down to the target temperature. In order to activate bulk RE–Ba–Cu–O magnets, one needs to apply high magnetic fields. To make the operation simple, a pulse-field magnetization technique has been used to activate the bulk magnets in this system. At present, a magnetic field of 3 Tesla can be obtained at the center of two trapped-field magnets in free space [32]. An interesting feature of this magnet system is that the field configuration with like poles facing each other (e.g., N to N) can be easily produced by simply changing the direction of magnetization, in addition to the common field configuration of N to S. Pulse magnetization techniques have recently advanced very rapidly. Repeated pulse activation methods with varying peak fields enabled achieving a trapped field value as high as 5 Tesla [34] showing that one can have a bulk RE–Ba–Cu–O magnet system that generates 5 Tesla without the need of superconducting solenoid coils.

A.4.3.3 Levitation

One of the most popular applications of bulk RE–Ba–Cu–O superconductors is based on the magnetic levitation property. It has been demonstrated several times that large masses like a person could be levitated with a network of an array of superconductors and magnets [35]. A prototype maglev train based on the levitation of bulk RE–Ba–Cu–O has been developed by Wang et al. [36]. They used Fe–Nd–B magnets as a guide-way and levitated a vehicle 3.5 m in length, 1.2 mm in width, and 0.8 m in height that carries eight liquid nitrogen vessels, each containing 43 pieces of Y–Ba–Cu–O melt-textured blocks 30 mm in diameter and about 15 mm in thickness and cooled by liquid nitrogen. The vehicle could support the weight of 9000 N at gaps of 15 mm and 11,000 N at gap of 10 mm. The translational motion of the vehicle was controlled with a linear motor on the ground. Fig. A.8(e) shows the demonstration of such a levitated vehicle carrying two persons.

This property plays an important role in use of cryogenic tanks and transmission lines. This property also finds applications in magnetically levitated

conveyor systems useful in clean rooms, where high-purity requirements are mandatory with no mechanical contact [37].

A.4.3.4 Motor

The ability of bulk RE–Ba–Cu–O superconductors to trap very high magnetic fields [38] suggests their use in superconducting analogs to brushless synchronous motors that currently use permanent magnets. For the application of cryogen pumping, this device is adequate. A group of Kitano Seiki and TUMST [39, 40] have designed and fabricated an axial gap-type synchronous motor, where a rotor is composed of eight Gd–Ba–Cu– O bulk magnets. The dimensions of the motor were 500 mm diameter and 30 mm length, and used for ship propulsion. The output of the motor is 10kW at a rotation speed of 850 rpm [40]. A photograph of the motor is shown in Fig. A.8(f).

A.4.3.5 Flywheel

The combination of diamagnetic behavior of the superconductor and the ability to lock magnetic flux lines through pinning centers within bulk RE–Ba–Cu–O allows stable levitation of a permanent magnet above or below an RE–Ba–Cu–O superconductor [41, 42]. If a permanent magnet is cylindrically symmetric, it freely rotates about its axis of symmetry and forms a low-loss magnetic bearing that is quite stable [43]. The availability of superconducting bearings that are nearly friction free has naturally led to the construction of a flywheel energy storage system [44-46]. Flywheels with superconducting bearings made of bulk Y–Ba–Cu–O showed a rotational loss as small as 0.001% per hour, while it is nearly 1% per hour with the use of conventional bearings [45]. With modern carbon fiber re-inforced plastic materials, the inertial section of a flywheel rotates with a rim velocity in excess of 1000 m/s and achieves energy densities greater than those of advanced batteries. Superconducting bearings, of the model shown in Fig. A.8(g), could store 5 kWh power in the flywheels designed [47].

References

[1]   Kammerlingh Onnes H 1911 *Leiden Commun.* **120b** 1226

[2]   Narlikar A V and Ekbote S N 1983 *Superconductivity and Superconducting Materials* (South Asian Publishers, New Delhi, India) p 12

Easterling K E *Tomorrow's materials* 1990 Ed. II (Inst. Of Metals, London) p 112

[3]   Tilley R 2004 *Understanding Solids: The Science of Materials* (John Wiley, West Sussex, England) p 415

[4]   Bednorz J G and Müller K A 1986 *Z. Phys. B* **64** 189.

[5]   Wu M K, Ashburn J R, Torang C J, Hor P H, Meng R L, Gao L, Huang Z J, Wang Y Q and Chu C W 1987 *Phys. Rev. Lett.* **58** 908

[6]   Maeda H, Tanaka Y, Fukutumi M and Asano T 1988 *Jpn. J. Appl. Phys.* **27** L209

[7]   Sheng Z Z and Hermann A M 1988 *Nature* **332** 6160

[8]   Chu C W, Gao L, Chen F, Huang Z J, Meng R L and Xue Y Y 1993 *Nature* **365** 6444

[9]   Meissner W and Ochsenfeld R 1933 *Naturwissenschaften* **21** 787

[10]   Francis C. Moon 1994 *Superconducting Levitation: Applications to Bearings and Magnetic Transportation* (Wiley-VCH, Germany)

[11]   Ito E, Suzuki T, Sakai T, Koga S, Murakami M, Nagashima K, Sakai N, Hirabayashi I and Sawa K 2006 *Physica C* **445–448** 412

[12]   Walter H, Arsac S, Bock J, Siems S O, Canders W-R, Leenders A, Freyhardt H C, Fieseler H and Kesten M 2003 *IEEE Trans. Appl. Supercond.* **13** 2150

[13]   Kamijo H, Higuchi T, Fujimoto H, Ichikawa H and Ishigohka T 1999 *IEEE Trans. Appl. Supercond.* **9** 976

[14]   Kittel C 2002 *Introduction to Solid State Physics* Seventh ed.   (John Wiley, Toronto, Singapore) p 335

[15]   Parinov I A 2007 *Microstructure and Properties of High-Temperature Superconductors* (Springer, Berlin, Heidelberg)

[16]   Krabbes G, Fuchs G and Canders W-F 2005 *High Temperature Superconductor Bulk Materials: Fundamentals - Processing - Properties Control - Application Aspects* (Wiley, GmbH, KGaA, Weinheim)

[17]   Bardeen J, Cooper L N and Schrieffer J R 1957 *Phys. Rev.* **106** 162

[18]   London F and London H 1935 *Proceedings of the Royal Society of London A* **149** 71

[19]   Pippard A B 1953 *Physica C* **19** 765

Abrikosov A A 2004 *Rev. Mod. Phys.* **76** 975

[20]   Abrikosov A A 1957 *Zh. Eksp. Teor. Fiz.* **32** 1442

[21]   Campbell A M and Evetts J E 1972 *Adv. Phys.* **21** 199

[22]   Murakami M 1992 *Melt Processed High temperature Superconductors* (World Scientific, Singapore)

[23]   Matsushita T 2007 *Flux Pinning in Superconductors* (Springer-Verlag Berlin Heidelberg)

[24]   Hari Babu N, Iida K, Shi Y and Cardwell D A 2005 *Appl. Phys. Lett.* **87** 202506

[25]   Kobayashi S, Kaneko T, Kato T, Fujikami J and Sato K 1996 *Physica C* **258** 336

[26]   Fisher D S, Fisher M P A and Huse D A 1991 *Phys. Rev. B.* **43** 130

[27]   Palstra T T M, Batlogg B, van Dover R B, Schneemeyer L F and Waszczak J V 1989 *Appl. Phys. Lett.* **54** 763

Shi D, Boley M S, Welp U, Chen J G and Liao Y 1989 *Phys. Rev. B* **40 5255**

[28] Chen I 2008 AAPPS Bulletin **18** 17

[29] Cohen L F, Totty J T, Perkins G K, Doyle R A and Kadowaki K 1997 *Supercond. Sci. Technol.* **10** 195

[30] S. Akiyama "Noncontact rotary apparatus," Patent Abstracts of Japan, Application Number 10298750, 2000.

[31] Koyama F, Akiyama S and Murakami M 2006 *Supercond. Sci. Technol.* **19** S572

[32] Fujishiro H, Tateiwa T, Fujiwara A, Oka T and Hayashi H 2006 *Physica C* **445–448** 334

[33] Saho N, Mizumori T, Nishijima N, Murakami M and Tomita M 2003 *Ceram. Trans.* **141** 325

[34] Oka T, Itoh Y, Yanagi Y, Yoshikawa M, Ikuta H and Mizutani U 2000 *Physica C* **335** 101

[35] Murakami M 1993 *Appl. Supercond.* **1** 1157

[36] Wang J S, Wang S Y, Ren Z Y, Jiang H, Zhu M, Wang X R, Shen X M and Song H H 2003 *Physica C* **386** 431

[37] Minami H and Yuyama J 1995 *Jpn. J. Appl. Phys.* **34** 346

[38] Tomita M and Murakami M 2003 *Nature* **421** 517

[39] Miki M, Tokura S, Hayakawa H, Inami H, Kitano M, Matsuzaki H, Kimura Y, Ohtani I, Morita E, Ogata H, Izumi M, Sugimoto H and Ida T 2006 *Supercond. Sci. Technol.* **19** S494

[40] Driscoll D, Dombrovski V and Zhang B 2000 *IEEE Power Eng. Rev.* **20** [5] 12

[41] Brandt E H 1990 *Am. J. Phys.* **58** 43

[42] Nariki S, Fujikura M, Sakai N, Hirabayashi I and Murakami M 2005 *Physica C* **426–431** 654

[43] Hull J 2000 *Supercond. Sci. Technol.* **13** R1

[44]   Nagaya S, Kashima N, Minami M, Kawashima H and Unisuga S 2001 *IEEE Trans. Appl. Supercond.* **11** 1649

[45]   Hull J R 1997 *IEEE Spectrum* **34** 20

[46]   Day A C, Hull J R, Strasik M, Johnson P E, McCrary K E, Edwards J, Mittleider J A, Schindler J R, Hawkins R A and Yoder M L A 2003 *IEEE Trans. Appl. Supercond.* **13** 2179

[47]   Matsunaga K, Tomita M, Yamachi N, Iida K, Yoshioka J, Isono M, Hirose M, Nasu H, Kameno H, Kubo A, Takahata R, Kitai N, Yamamoto H, Nakamura Y, Koshizuka N and Murakami M 2002 *Physica C* **378–381** 883

FIGURE CAPTIONS

Fig.1.1.   Evolution in the transition temperatures of superconducting materials, starting with mercury. Recent discoveries are also included.

Fig.1.2.   Perovskite structure of YBCO showing the presence of copper planes and chains.

Fig.1.3.   The oxygen deficient perovskite structures for Y-Ba-Cu-O system with oxygen content (a) δ=6, (b) $6 < \delta < 7$, (c) $\delta = 7$.

Fig.1.4.   A pseudo-binary phase diagram for the Y-Ba-Cu-O system [*21*]. The peritectic temperature of Y-123 is ~1008°C in air. Above this temperature, solid Y-123 disassociates into solid Y-211 and barium rich liquid phases (L_1). Above 1200°C, the Y-211 phase further disassociates to form Y_2O_3 and liquid phases L_2 comprising of BaO and CuO.

Fig.1.5.   Microstructure of a melt-grown YBCO sample obtained using a scanning electron microscope. Presence of platelets can be seen. Y-211 particles were found to be large in size and acicular in morphology.

Fig.1.6.   A schematic sketch comparing TSMG and IG processes.

Fig.2.1.   Powders of (a) Y-123 and (b) Y-211 as obtained after combustion process.

Fig.2.2.   (a) Photograph of the sintered powders of Y-123 and Y-211 is shown. (b)Scanning electron micrograph obtained from sintered Y-211 powder used in the present experiments is shown. The micrograph shows that the Y-211 particles are of size in the range 400 nm – 1000 nm.

Fig.2.3.   A schematic diagram of the furnace used.

Fig.2.4.   The heat profiles showing the temperature distribution obtained along the length of the muffle in tubular furnaces used for (a) sintering / IGP and (b) oxygenation.

Fig.2.5.   X-ray diffractograms obtained from sintered powders of (a) Y-123 and (b) Y-211.

Fig. 4.2. The experimental arrangement used in the present study for fabricating YBCO/Ag composites employing POIGP. Sample *A* was fabricated without any Ag addition, Sample *B* was prepared by adding Ag directly to the Y-211 preform, and samples *C* and *D* were fabricated by adding Ag to the liquid phase source (Y-123) at the top.

Fig. 4.3. (a) A schematic diagram showing the positions from where specimens to study microstructure were collected. P, Q, R and S are at increasing distances from the Nd-123 seed crystal. Row (b), which corresponds to Sample B in which Ag was added to the preform, shows optical micrographs at 50x from the four regions P, Q, R and S. We observe that in all the regions, the microstructure is highly porous. Row (c) for Sample C with 10wt.% Ag added along with the liquid phase, has less porosity in all regions and show some amount of macro-cracks. Row (d) for Sample D with 20wt.% Ag added along with the liquid phase, has minimal porosity in all regions and show fewer cracks. In (b), large Ag particles can be seen (white in the figure) and the size of silver particles in (c) and (d) are below the resolution limit in the micrographs.

Fig. 4.4. Images from the POIGP samples *A*, *B*, *C* and *D* obtained using the in-lens detection mode of the Zeiss-make FE-SEM. A uniform distribution of Y-211 particles is observed in the micrographs (a), (c) and (d) from samples *A*, *C* and *D;* Sample A had no Ag and in Samples C and D, Ag was added along with the liquid phase. (b) In Sample *B* which was fabricated with Ag added to the Y-211 preform, the Y-211 distribution is not uniform. When Ag is introduced through the liquid phase source, the Y-211 particle size is refined, with the refinement becoming a maximum with sample *D*.

Fig. 4.5 Histograms are constructed showing the number of Y-211 particles in different size ranges versus the average size of such particles in each range. The histograms were constructed using the micrographs in Fig. 4.4. Figs. (a), (b), (c) and (d) are for the Samples A, B, C and D respectively.

Fig.6.8.   The pole figure and the inverse pole figure obtained on the S-460 sample indicating the orientations observed are shown in (a) and (b) respectively. The extent of orientation can be seen from the color coding provided in (a). RD and TD stand for Reference Direction and Transverse Direction respectively.

Fig.6.9   (a) Crystal orientation map for the superconducting Y-123 phase in the S-460 sample is shown. The black regions in this map correspond to grains of Y-211 phase and the partition has been created to show only the Y-123 region in white. The green lines are high angle domain boundaries. The top and left region of the figure has a dense population of Y-211, and the bottom right bottom portion is relatively sparsely populated with Y-211, in the field of view. Misorientation profiles were generated within both the regions. The lines along which the profiles were recorded are shown red (color online). (b) shows the profile recorded from a region densely populated in Y-211 and (c) is from a region that is relatively sparsely populated. In (b), the presence of 90° misorientations between neighboring regions has been observed. In (c), only low angle domain boundaries (neighboring grains misoriented between $1°$ and $5°$) are observed in a region where Y-211 particles are fewer. The width of the 90° domains is measured from (b), and is observed to vary in the range 50 nm to 180 nm. The grain boundary character distribution (GBCD) for the scan area in (a) is shown in (d). As can be seen the most number of boundaries are centered around $90°$ misorientation.

Fig.6.10   Representative crystal orientation map for the Y-211 phase in the sample S-460 is shown. The corresponding orientations of the particles can be seen from the color coded picture provided in (a). It is evident from the figure that Y-211 particles show random orientation. This is also seen in the pole figure provided in (b) and inverse pole figure provided in (c).

Fig.6.11.   FE-SEM images obtained under a magnification of 25,000 x and 50,000 x from the samples S-300 and S-380 are shown. Nano-twinning is seen in both the samples. The twin widths were found to be in the range 40 nm – 100 nm.

Fig.6.12.   FE-SEM images obtained under a magnification of 25,000 x and 50,000 x from the samples S-460 and S-540 are shown. The images show extensive nano-twinning throughout the samples. The twin widths vary in the range 25 nm – 100 nm. Changes in twin directions giving rise to crossing twins can be observed in the areas where small Y-211 particles are in close vicinity. Abundance

of crossing twins resulting in increased twin density is observed in the sample S-460.

Fig.A.1. Schematic representation of the variation of electrical resistance of a superconductor in comparison to that of a non-superconducting metal.

Fig.A.2. A closed contour indicating the superconducting regime.

Fig.A.3. (a) Schematic sketch of complete magnetic flux expulsion from the interior of the superconductor when $T<T_c$ can be seen. At $T > T_c$, the flux enters the superconductor since it is in the normal state. (b) The demonstration of magnetic levitation of a YBCO superconductor levitating a $SmCo_5$ magnet over it. The levitation gap between the superconductor and the magnet was found to be $\sim 7 - 8$ mm at 77 K.

Fig.A.4. Field dependence of magnetization (M) for (a) Type-I superconductor and (b) Type-II superconductor.

Fig.A.5. Schematic representation of H-T phase diagram of (a) Type-I and (b) Type- II superconductors.

Fig.A.6. Schematic representation of the mixed state of a Type-II superconductor. The flux tubes (fluxoids) arranged in a two-dimensional lattice, allow the magnetic field to penetrate. Each fluxoid is surrounded by superconducting ring currents and enclose one magnetic flux quantum.

Fig.A.7. A schematic sketch showing the direction of the Lorentz force resulting on the vortices due to the application of magnetic field.

Fig.A.8. (a) A schematic picture of a noncontact superconducting mixer. The upper part is coupled by an attractive force between two Fe–Nd–B magnets and the lower part is coupled by the attractive force between an Fe–Nd–B magnet and bulk Gd–Ba–Cu–O superconductor [30] (b) Photograph of a magnetic separation device for water purification. Bulk Gd–Ba–Cu–O magnets are cooled by a cryocooler and inserted into the device after magnetization by a superconducting solenoid. [33] (c) Single-pole and (d) double-pole magnetic field generators using RE-Ba-Cu-O magnets [34] (e) Levitated vehicle carrying two people [36] (f) Synchronous motor with bulk RE–Ba–Cu–O magnets on operation. The motor is rotating a propeller for ship propulsion. [38] (g) Flywheel energy storage system that can store 10 kWh [47].

TABLE CAPTIONS

Table 1.1.   Properties of some superconductors

Table 1.2.   Peritectic temperature (T_p) of various REBCO compounds

Table 2.1.   Details of crystal structure and unit cell dimensions as analyzed from X-ray diffractograms obtained from sintered powders of Y-123 and Y-211

Table 3.1.   Comparison of transition temperatures and transition widths of the YBCO samples fabricated by POIGP

Table 3.2.   Comparison of various microstructural properties of YBCO superconductors fabricated by POIGP

Table 3.3.   Comparison of various parameters obtained from the field dependences of J_c obtained for samples studied

Table 3.4.   Zero field J_c and J_c(H) of samples fabricated by MG and IG processing techniques from the literature, in comparison with the results from the present work

Table 3.5.   Fit parameters for the POIGP samples S-300 to S-540

Table 4.1.   Details of the YBCO and YBCO/Ag samples studied in the present work

Table 5.1.   Comparison of various microstructural properties of YBCO superconductors fabricated by DS-POIGP

Table 6.1.   Range of peak fields (H_p) computed for the S-460 sample from various microstructural features observed by different techniques

Table A.1.   Critical temperature T_c (K) for various superconducting elements and alloys

Table A.2.   Critical temperature T_c (in K) of some high temperature superconducting compounds

PUBLICATION LIST

Publications in Journals

1. Unprecedented current density to high fields in $YBa_2Cu_3O_{7-\delta}$ superconductor through nano-defects generated by preform optimization in infiltration growth process
   N. Devendra Kumar, T. Rajasekharan, K. Muraleedharan, A. Banerjee and V. Seshubai
   Supercond. Sci. Technol. **23** 105020 (2010).

2. YBCO/Ag composites through preform optimized infiltration and growth process yielding high current densities
   N. Devendra Kumar, T. Rajasekharan and V. Seshubai
   Supercond. Sci. Technol. **24** 085005 (2011).

3. Extensive nano-twinning: origin of record high current density to high fields in $YBa_2Cu_3O_{7-\delta}$ superconductor
   N. Devendra Kumar, T. Rajasekharan, Ravi. C. Gundakaram and V. Seshubai
   (Submitted to *IEEE Trans. Appl. Supercond.* - Under Review)

4. Significance of preform compaction pressure in improving the microstructure and current densities in Infiltration Growth processed $YBa_2Cu_3O_{7-\delta}$ superconductors
   N. Devendra Kumar, T. Rajasekharan, A. Banerjee and V. Seshubai
   (Submitted to *J. Appl. Phys.* – Under Review)

5. Effect of nano-CeO_2 on the microstructural and magnetic properties of IG processed YBCO superconductors fabricated by Gelcasting technique
   P.M. Swaroop Raju, **N. Devendra Kumar**, T. Rajasekharan and V. Seshubai
   (Under preparation)

Publications in the International/National Symposia/Workshops

1. Effect of Nano-Precipitates in RE-123 Superconductors
   N. Devendra Kumar, V. Seshu Bai and T. Rajasekharan
   National level Symposium "Self Assembly routes for Nanotech Materials-2006
   (SARNaM – 2006), Mumbai April 2006.

2. Magnetic Levitation and Suspension effects in high J_c YBCO superconductors made by seeded Infiltration and Growth & Melt Growth processing techniques.
   N. Devendra Kumar, B. Satyanand, V. Seshu Bai and T. Rajasekharan
   Proceedings of International Conference on Advanced Materials IUMRS – ICAM 2007, Page S-17, October 8-13, 2007, Bangalore, India.

3. Optimization of Y-211 content in Y-123 matrix in IG Processed YBCO Superconductors
   N. Devendra Kumar, V. Seshu Bai and T. Rajasekharan
   Proceedings of International Conference on Condensed Matter Physics (ICCMP-2007), Page 27, November 25-28, 2007, Jaipur, India.

4. High Temperature Superconductors as Non-Linear Inductive cores for high Frequency applications
   N. Devendra Kumar, V. Seshu Bai and T. Rajasekharan
   Proceedings of East Asia Symposium on Superconductor Electronics (EASSE), Page OL 12, December 11-15, 2007, New Delhi, India.

5. High J_c bulk YBCO superconductors with enhanced flux pinning by IG Process
   V. Seshubai and **N. Devendra Kumar**
   UoH-TIFR Interaction Meeting, August 20-22, 2009 University of Hyderabad, Hyderabad.

6. Fish Tail effect in high J_c bulk YBCO superconductor fabricated by Seeded Infiltration Growth process
   N. Devendra Kumar, P. Missak Swarup Raju, Sabyasachi Saha, V. Seshu Bai, Alok Banerjee, K. Muraleedharan and T. Rajasekharan
   Proceedings of 54th DAE-Solid State Physics Symposium, Page 803, December 14-18, 2009, Vadodara, India.

7. Levitation force measurements on Ag doped SIG processed bulk YBCO superconductor
   R. Parthasarathy, M. Mahalakshmi, **N. Devendra Kumar** and V. Seshubai

Proceedings of 54th DAE-Solid State Physics Symposium, Page 813, December 14-18, 2009, Vadodara, India.

8. Optimization of Ag content in SIG processed bulk YBCO superconductors by levitation and suspension force measurements
    R. Parthasarathy, M. Mahalakshmi, **N. Devendra Kumar** and V. Seshubai
    Proceedings of 54th DAE-Solid State Physics Symposium, Page 817, December 14-18, 2009, Vadodara, India.

9. High J_c bulk YBCO superconductors fabricated by Preform Optimized Infiltration Growth Process (PO-IGP)
    V. Seshubai and **N. Devendra Kumar**
    India-Singapore Joint Physics Symposium 2010 (ISJPS-2010), proceedings page 38, February 19-21, 2010 University of Hyderabad, Hyderabad.

10. Effect of nano sized CeO_2 doping on magnetic and microstructural properties of IG processed YBCO
    P Missak Swarup Raju, **N. Devendra Kumar**, V. Seshubai and T. Rajasekharan
    Proceedings of India-Singapore Joint Physics Symposium 2010 (ISJPS-2010), Page 72, February 19-21, 2010 University of Hyderabad, Hyderabad.

11. Strong pinning and enhanced flux trapping due to nanometer sized defects caused by submicron non-superconducting precipitates in Ag doped YBCO superconductors
    R. Parthasarathy, M. M. Lakshmi, **N. Devendra Kumar**, V. Seshubai and T. Rajasekharan
    Proceedings of India-Singapore Joint Physics Symposium 2010 (ISJPS-2010), Page 73, February 19-21, 2010 University of Hyderabad, Hyderabad.

12. Extensive nano-twinning : cause of enhancement of flux pinning to high fields in YBCO superconductors fabricated by Preform optimized Infiltration Growth Process
    N. Devendra Kumar and V. Seshubai
    Workshop on "Physics at small scales" organized at University of Hyderabad, Hyderabad during March 18-19, 2011.

13. Nano-twinning: cause for high Jc to high fields in bulk YBCO superconductor fabricated by Preform Optimized Infiltration Growth Process
    N. Devendra Kumar, P. Missak Swarup Raju, Sabyasachi Saha, V. Seshu Bai, K. Muraleedharan and T. Rajasekharan
    International conference Electron Nanoscopy & XXXII Annual Meeting of EMSI (EM-50) organized jointly by Defence Metallurgical Research Laboratory and Electron Microscope Society of India during July 6-8, 2011.

N. DEVENDRA KUMAR

Phone : 91-9441521071
E-mail: ndevendra@gmail.com

Work Address: **Home Address:**

Research Scholar   *Plot No. 83*
School of Physics   *Sri Durganjanadri Nagar*
University of Hyderabad   *Manneguda, Hayathnagar Mandal*
Gachibowli, Hyderabad – 500046   *Hyderabad – 501510*
Andhra Pradesh, India   *Andhra Pradesh, India*
Phone: 91-40-23134365, 23010241,   *Phone: 9441521071*

Academic achievements

- ❖ Pursuing Doctor of Philosophy (**Ph.D**.) in University of Hyderabad, in Physics Stream
  - ➢ Specialization :   Superconductivity
  - ➢ Current status: Thesis submitted
  - ➢ Title of the thesis: **Enhanced Flux Pinning To High Fields In YBCO and YBCO/Ag Superconductors through Preform Optimization in Infiltration and Growth Process**

- ❖ Master of Science (**M.Sc**.) from University of Hyderabad in Physics Stream, 2003 with **73.5 %**
  - ➢ Specialization :   Solid State Physics
  - ➢ Undergone research training in the form of a project as a part of M.Sc. course
  - ➢ Title of the project: **Measurement of magnetic properties of superconducting YBCO toroid made by IG Process**

- ❖ Bachelor of Science (**B.Sc**.) from Sri Venkateswara University, Tirupati, 2001 with **80.1 %**
  - ➢ Specialization: Mathematics, Physics and Electronics
  - ➢ Undergone training in the form of a project as a part of B.Sc. program
  - ➢ Title of the project: **AC-DC Converter: Bridge Rectifier Circuit**

- ❖ **Intermediate** from Board of Intermediate Education, Andhra Pradesh, 1998 with **85.7 %**

- ❖ **Class X (SSC)** from Board of Secondary Education, Andhra Pradesh, 1996 with **83.5%**

Additional Qualifications

- ❖ Secured **93.7** percentile in GATE 2004 National Level Examination.
- ❖ Secured **85.5** percentile in JEST 2004 National Level Examination.
- ❖ Secured a "Praveena" degree from Dakshina Bharata Hindi Prachar Sabha, Chennai, India, 1997.

Interests

- ❖ Applied research
- ❖ Condensed Matter Physics, Cryogenics
- ❖ Coated Conductors, Electrical and Magnetic properties of Superconductors, Superconducting wires and tapes, Superconducting thin films.

Hands on experience with Instruments like

- ➢ Physical Property Measurement System PPMS (Quantum Design-make) with various attachments like Vibrating Sample Magnetometer (with Oven), ac susceptibility, Resistivity, thermal transport measurement etc.

- ➢ Microscopes like

  - ∗ Metallurgical Optical Microscope with Polarizer attachment (Zeiss make, Model Axiovert)
  - ∗ Scanning Electron Microscope (FEI-make, Model XL30 ESEM)
  - ∗ Field Emission Scanning Electron Microscope FE-SEM (Zeiss make, Model Ultra 55)
  - ∗ Atomic Force Microscope (SEIKO make, Model SPA 400)

- ➢ Low Speed Diamond Saw, ISOMET 1000 and an Auto-polisher of Buehler make. Developed expertise in preparing samples for observation under SEM and TEM.

- ➢ Automated data acquisition through LabVIEW using Programmable instruments like dc constant current source (Keithley make, model 224), ac/dc current source (Keithley-make, model 6221), nano-voltmeter (Keithley-make, model 181), cryogenic temperature controller (Lakeshore-make, model DRC-93C), lock-in amplifier (Stanford-make, model SR830), multimeter (Keithley-make, model 2000) etc.

- ➢ Furnaces operating to 1200^oC /1500^oC furnaces controlled by programmable temperature controller and thyristor (Eurotherm-make/WEST-make).

- ➢ Sample preparation techniques for fabricating high temperature bulk REBCO superconductors and preliminary work on wires by PIT technique.

Contributions in the form of facilities for the research lab during my Ph.D. program

➢ Facility for obtaining temperature dependence of electrical resistivity by four probe technique.

➢ Facility for obtaining temperature dependence of ac susceptibility by mutual Inductance principle.

➢ Facility to fabricate REBCO samples in short-time scales by employing directionally solidified Infiltration Growth process.

➢ Levitation and Suspension force (of superconductors) measurement facility.

➢ Established the methodology of developing YBCO superconducting wires of short lengths (∼ 60 mm) using Powder-in-tube technique.

Important Scientific contributions to the area of work during Ph.D. program

➢ Achieved uniformity in the distribution of Y-211 precipitates in the Y-123 matrix across the volume of the YBCO samples by paying attention to the Y-211 preforms during their fabrication.

➢ Optimized the Y-211 content in the Y-123 matrix of samples fabricated by POIGP for enhanced current densities to high fields.

➢ Achieved homogeneity in the distribution of both Ag and Y-211 particles in the Y-123 matrix by introducing metallic Ag along with the liquid phases in POIGP. A substantial refinement of Y-211 particles and a significant reduction in macro-crack density were achieved by introducing silver along with the liquid phases.

➢ Developed a method to fabricate high current density (J_c) superconductors in short time combining Directional solidification in IG process (DSIG).

➢ Developed a method of fabricating YBCO wires and tapes of short lengths with Ag-Pd clad employing IG process following powder-in-tube technique. The preliminary results on the fabricated YBCO wire showed sharp superconducting transition and a J_c of ∼ 100 Acm^{-2} at 77 K.

Computational skills

➢ Origin, MS office (Word, excel, power-point etc.) and Fortran.

➢ NI Lab-View for automation of data acquisition.

➢ Microstructural analysis using Axio-vision / Image analysis software.

➢ Having familiarity with scientific software like JCPDS data cards, binary phase diagrams, crystal structure analysis using X-pert software.

Work Experience in the projects

➢ Research Fellow in the project entitled "RE-123 Wires by IG process" funded by Department of Science and Technology (DST) Govt. of India during 2006-2009.

➢ Research Fellow in the project entitled "Enhancement of critical current densities in IG processed REBCO superconductors" under Center for Nanotechnology funded by DST, Govt. of India during 2009-2010.

Workshops / Training courses attended

❖ Course on "Metallography" conducted at ASM International Chapter, Pune during September 1-2, 2005.

❖ One day course on "LabVIEW 8 Hands-On Technology workshop" conducted by National Instruments, India at Hyderabad on February 15, 2006.

❖ "Awareness Workshop on the Experimental Facilities of UGC-DAE Consortium for Scientific Research" organized by UGC-DAE CSR and Department of Physics, Osmania University at Hyderabad during March 4-5, 2006.

❖ "Workshop on Superconductivity" organized at University of Hyderabad during January 27-28, 2007.

❖ "Workshop on Low Temperature Physics" Organized at School of Physics, University of Hyderabad during March 14-15, 2008.

❖ "University of Hyderabad – Tata Institute of Fundamental Research (UoH-TIFR) Interaction Meeting organized at University of Hyderabad, Hyderabad during August 20-22, 2009.

❖ India-Singapore Joint Physics Symposium 2010 (ISJPS-2010), organized at University of Hyderabad, Hyderabad during February 19-21, 2010.

❖ Workshop on "Physics at small scales" organized at University of Hyderabad, Hyderabad during March 18-19, 2011.

Achievements and Awards

❖ **Best poster award** in the Workshop on "Physics at small scales" organized at University of Hyderabad, Hyderabad during March 18-19, 2011.

❖ College topper during Intermediate and Graduation courses. Graduation passed with distinction.

❖ Secured All India rank **174** in Graduate Aptitude Test in Engineering (GATE) 2004.

❖ Secured several prizes during school and college days in various literary competitions like Essay-writing, Elocution, quiz, debate etc.

Personal

- ❖ Father's Name   :   Sri. N. Krishna Moorthy
- ❖ Mother's Name   :   Smt. N. Manohari
- ❖ Date of Birth   :   May 29, 1981
- ❖ Nationality   :   Indian
- ❖ Place of Birth   :   Sri Kalahasthi, Andhra Pradesh, India

Reference

- ❖ **Professor. V. Seshubai**, University of Hyderabad, Hyderabad, India.

  E-mail: seshubai@gmail.com

- ❖ **Dr. T. Rajasekharan**, Sc-G, Defense Metallurgical Research laboratory (DMRL), Hyderabad, India

  E-mail: trajasekharan@gmail.com

- ❖ **Dr. A. Banerjee**, Scientist, UGC-DAE Consortium for Scientific Research Indore, India.

  E-mail: alok@csr.ernet.in

- ❖ **Dr. G. Ravi Chandra,** Advanced Research Centre Imarat (ARCI), Hyderabad, India.

  E-mail: ravi.gundakaram@gmail.com

- ❖ **Professor. S.N. Kaul**, University of Hyderabad, Hyderabad, India.

  E-mail: kaulsp@uohyd.ernet.in

Declaration

I declare that the information provided is true to the best of my knowledge.

N. DEVENDRA KUMAR

Date: August 11, 2011

Place: Hyderabad